Advanced acoustic emission methods for damage mechanisms monitoring in aerospace materials

Politecnico di Bari

LIBERATORIA PER L'ARCHIVIAZIONE DELLA TESI DI DOTTORATO

Al Magnifico Rettore
del Politecnico di Bari

Il/la sottoscritto/a **Dany Katamba Mpoyi** nato/a **Kinshasa il 25/12/1994**

residente a Bari in via De Viti De Marco e-mail dany.katambampoyi@poliba.it

iscritto al 3° anno di Corso di Dottorato di Ricerca in Ingegneria e Scienze Aerospaziali ciclo XXXVII

ed essendo stato ammesso a sostenere l'esame finale con la prevista discussione della tesi dal titolo:

Advanced Acoustic Emission Methods for Damage Mechanisms Monitoring in Aerospace Materials

---

DICHIARA

1) di essere consapevole che, ai sensi del D.P.R. n. 445 del 28.12.2000, le dichiarazioni mendaci, la falsità negli atti e l'uso di atti falsi sono puniti ai sensi del codice penale e delle Leggi speciali in materia, e che nel caso ricorressero dette ipotesi, decade fin dall'inizio e senza necessità di nessuna formalità dai benefici conseguenti al provvedimento emanato sulla base di tali dichiarazioni;
2) di essere iscritto al Corso di Dottorato di ricerca in Ingegneria e Scienze Aerospaziali ciclo XXXVII, corso attivato ai sensi del "*Regolamento dei Corsi di Dottorato di ricerca del Politecnico di Bari"*, emanato con D.R. n.286 del 01.07.2013;
3) di essere pienamente a conoscenza delle disposizioni contenute nel predetto Regolamento in merito alla procedura di deposito, pubblicazione e autoarchiviazione della tesi di dottorato nell'Archivio Istituzionale ad accesso aperto alla letteratura scientifica;
4) di essere consapevole che attraverso l'autoarchiviazione delle tesi nell'Archivio Istituzionale ad accesso aperto alla letteratura scientifica del Politecnico di Bari (IRIS-POLIBA), l'Ateneo archivierà e renderà consultabile in rete (nel rispetto della Policy di Ateneo di cui al D.R. 642 del 13.11.2015) il testo completo della tesi di dottorato, fatta salva la possibilità di sottoscrizione di apposite licenze per le relative condizioni di utilizzo (di cui al sito http://www.creativecommons.it/Licenze), e fatte salve, altresì, le eventuali esigenze di "embargo", legate a strette considerazioni sulla tutelabilità e sfruttamento industriale/commerciale dei contenuti della tesi, da rappresentarsi mediante compilazione e sottoscrizione del modulo in calce (Richiesta di embargo);
5) che la tesi da depositare in IRIS-POLIBA, in formato digitale (PDF/A) sarà del tutto identica a quelle **consegnate**/inviate/da inviarsi ai componenti della commissione per l'esame finale e a qualsiasi altra copia depositata presso gli Uffici del Politecnico di Bari in forma cartacea o digitale, ovvero a quella da discutere in sede di esame finale, a quella da depositare, a cura dell'Ateneo, presso le Biblioteche Nazionali Centrali di Roma e Firenze e presso tutti gli Uffici competenti per legge al momento del deposito stesso, e che di conseguenza va esclusa qualsiasi responsabilità del Politecnico di Bari per quanto riguarda eventuali errori, imprecisioni o omissioni nei contenuti della tesi;
6) che il contenuto e l'organizzazione della tesi è opera originale realizzata dal sottoscritto e non compromette in alcun modo i diritti di terzi, ivi compresi quelli relativi alla sicurezza dei dati personali; che pertanto il Politecnico di Bari ed i suoi funzionari sono in ogni caso esenti da responsabilità di qualsivoglia natura: civile, amministrativa e penale e saranno dal sottoscritto tenuti indenni da qualsiasi richiesta o rivendicazione da parte di terzi;
7) che il contenuto della tesi non infrange in alcun modo il diritto d'Autore né gli obblighi connessi alla salvaguardia di diritti morali od economici di altri autori o di altri aventi diritto, sia per testi, immagini, foto, tabelle, o altre parti di cui la tesi è composta.

Luogo e data 29/01/2025 Firma _____

Il/La sottoscritto, con l'autoarchiviazione della propria tesi di dottorato nell'Archivio Istituzionale ad accesso aperto del Politecnico di Bari (POLIBA-IRIS), pur mantenendo su di essa tutti i diritti d'autore, morali ed economici, ai sensi della normativa vigente (Legge 633/1941 e ss.mm.ii.),

CONCEDE

- al Politecnico di Bari il permesso di trasferire l'opera su qualsiasi supporto e di convertirla in qualsiasi formato al fine di una corretta conservazione nel tempo. Il Politecnico di Bari garantisce che non verrà effettuata alcuna modifica al contenuto e alla struttura dell'opera.
- al Politecnico di Bari la possibilità di riprodurre l'opera in più di una copia per fini di sicurezza, back-up e conservazione.

Luogo e data 29/01/2025 Firma _____

INTER-UNIVERSITY PH.D. PROGRAM
POLITECNICO DI BARI - UNIVERSITÀ DEGLI STUDI DI BARI ALDO MORO

Ph.D. Thesis

PhD Course in Engineering and Aerospace Sciences- XXXVII Cycle
SSD: ING-IND–03/A: Mechanical Design and Machine Construction

---

Advanced Acoustic Emission Methods for Damage Mechanisms Monitoring in Aerospace Materials

---

Ph.D. Student

Dany Katamba Mpoyi

Tutors

Prof. Caterina Casavola

Prof. Giovanni Pappalettera

Coordinator of Ph.D. Program:
Prof. Marco Donato De Tullio

Course n°37, 01/11/2021-31/10/2024

INTER-UNIVERSITY PH.D. PROGRAM
POLITECNICO DI BARI - UNIVERSITÀ DEGLI STUDI DI BARI ALDO MORO

Ph.D. Thesis

PhD Course in Engineering and Aerospace Sciences- XXXVII Cycle
SSD: ING-IND–03/A: Mechanical Design and Machine Construction

---

Advanced Acoustic Emission Methods for Damage Mechanisms Monitoring in Aerospace Materials

---

Ph.D. Student
Dany Katamba Mpoyi

Tutors
Prof. Caterina Casavola

Prof. Giovanni Pappalettera

Coordinator of Ph.D. Program:
Prof. Marco Donato De Tullio

Referees
Prof. Aime Lay Ekuakille
Prof. Carmine Maletta

Course n°37, 01/11/2021-31/10/2024

To my loved ones, to my family

Acknowledgements

I would like to express my deep gratitude to my supervisors, Professors Caterina CASAVOLA and Giovanni PAPPALETTERA, who, despite their many responsibilities, have always been available to support me in my scientific and social development. Their support, wise counsel, and dedication have been essential to the success of this work.
I would like to make a special mention of my co-supervisor, Prof. Giovanni PAPPALETTERA, who has always shown great kindness and has been consistently available to answer all my questions, whether scientific or administrative. His invaluable advice and skilful coordination have been of immense help throughout these years of research.
My warmest thanks also go to Professor Claudia BARILE for her invaluable expertise and encouragement, and to Dr. Vimalathithan PARAMSAMY KANNAN for his assistance and decisive contributions to the progress of this research.
Finally, I would like to thank the Polytechnic University of Bari (Department of Mechanics, Mathematics and Management) for making this project possible by granting me a doctoral scholarship.

Abstract

This thesis develops advanced Acoustic Emission (AE) techniques for monitoring and characterizing damage in aerospace materials. It focuses on AlSi10Mg produced by Selective Laser Melting (SLM) and on Carbon Fiber Reinforced Plastic (CFRP) composites. These materials are crucial for aerospace due to their unique mechanical properties. AlSi10Mg offers high strength and fatigue resistance. It is used in critical aerospace parts. CFRP composites provide stiffness strength and corrosion resistance, making them suitable for demanding aerospace environments. Monitoring damage in these materials is essential to ensure safety and structural integrity over time.

This research aims to improve damage monitoring by combining traditional AE methods with deep learning frameworks. Structural Health Monitoring (SHM) is vital in aerospace. It allows early detection of material degradation and reduces the risk of in-service damages. Traditional SHM methods can be limited in accuracy for complex materials such as AlSi10Mg and CFRP composites. This thesis introduces a robust approach that uses advanced methods to address these challenges.

Tensile tests were conducted on AlSi10Mg specimens built in different orientations. AE signals were recorded to examine their mechanical behavior. Continuous Wavelet Transform (CWT) was used to analyze these signals. This allowed differentiation between elastic and plastic deformation. Convolutional Neural Networks (CNNs) were then used to classify AE signals. Several CNN architectures, including AlexNet and SqueezeNet, were tested to improve classification accuracy. A novel approach was also introduced. It combines a Fuzzy Artificial Bee Colony (FABC) algorithm with CNN and CWT-scalogram analysis. This method includes data augmentation to improve robustness and prevent overfitting.

For CFRP composites, a Deep Autoencoder (DAE) framework was developed to automate damage mode characterization during mechanical testing. The DAE reduced the complexity of AE signals and extracted essential features. These features were clustered to identify damage modes like matrix cracking, delamination, and fiber breakage. By automating damage classification, the DAE enhances SHM by providing accurate real-time damage assessments.

This thesis shows that combining traditional AE features with deep learning models improves damage source classification for aerospace materials. These methods make SHM systems more efficient and precise. They offer advanced solutions for monitoring and maintaining structural integrity in aerospace. The research contributes to safer and more reliable aerospace applications.

Key Words: Acoustic Emission, Non-Destructive Testing, Selective Laser Melting, AlSi10Mg, Carbon Fiber Reinforced Plastic, Deep Learning, Convolutional Neural Networks, Continuous Wavelet Transform, Fuzzy Artificial Bee Colony, Deep Autoencoder, Structural Health Monitoring, Damage Mechanisms, Signal Classification, Aerospace Materials.

Contents

Chapter 1. Introduction

1.1 Context and importance of damage monitoring in Aerospace materials

In aerospace, the structural integrity of materials is critical due to the extreme operational conditions and the high safety standards required for aircraft and spacecraft. Aerospace materials, such as carbon fiber reinforced polymers (CFRP), aluminium alloys, and titanium composites, are designed to be lightweight and high strength [1]. Despite their advanced properties, these materials are still prone to degradation mechanisms such us fatigue, cracking, delamination, and corrosion over time, which can compromise their performance and reliability[2], [3], [4]. Effective damage monitoring is essential for detecting early signs of degradation before they lead to critical failures [5], [6], [7]. Traditional inspection methods, such as visual and ultrasonic testing, often fall short in identifying internal or subsurface damage, especially in composite materials [8], [9]. This limitation has led to the increased adoption of non-destructive evaluation (NDE) techniques, with Acoustic Emission (AE) emerging as a key method for real-time monitoring [10]. AE tech detects stress waves emitted by materials when damage occurs, such as crack initiation or fiber breakage[11]. AE offers the advantage of real-time, continuous monitoring, making it an ideal solution for identifying damage early, facilitating predictive maintenance [12]. This proactive approach reduces the risk of in-service failures, extends the lifespan of aerospace components, and optimizes maintenance schedules, thus lowering operational costs. As the aerospace industry embraces more advanced materials like composites and adopts cutting-edge manufacturing processes such as additive manufacturing (AM), the need for sophisticated damage monitoring becomes more pressing[13], [14]. Advanced AE methods, as developed in this thesis, are vital for accurately tracking and characterizing damage mechanisms in these materials. These methods play a crucial role in ensuring safety, performance, and longevity in modern aerospace structures.

1.2 Objectives and contributions of the thesis

This thesis focuses on advancing Acoustic Emission signal analysis methods to enhance damage detection and classification in aerospace materials. The ultimate goal is to contribute to the development of fully autonomous Structural Health Monitoring (SHM) systems. The primary objective is to improve existing monitoring techniques by developing tools that can facilitate the future integration of AE into SHM systems. The thesis emphasizes two key aerospace materials: AlSi10Mg, produced via Selective Laser Melting (SLM), and CFRP composites adhesively bonded in joggled lap shear configurations. These materials are critical in the aerospace industry due to their high strength and lightweight properties, making them ideal for structural applications.

The key objectives of this thesis are:

1. Develop advanced AE signal analysis methods that integrate traditional methods (time-domain, frequency-domain, and time-frequency analysis such us Continuous Wavelet

Transform (CWT)) with deep learning approaches, enabling better feature extraction and a deeper understanding of material degradation.
2. Introduce deep learning-based models, including customized Convolutional Neural Networks (CNNs) and a novel Fuzzy Artificial Bee Colony Convolutional Neural Network (FABC-CNN), to automate AE signal classification and improve damage mode identification, thereby reducing reliance on manual interpretation.
3. Implement a data augmentation strategy using Gaussian noise to expand the AE dataset, enhance model robustness, minimize overfitting, and improve the accuracy of AE signal classification, even with limited experimental data.
4. Apply these developed methods to AE signal analysis for aerospace materials such as AlSi10Mg and CFRP composites, with a focus on characterizing damage mechanism modes such as matrix cracking, delamination, and fiber breakage.
5. Contribute to predictive maintenance in aerospace by developing reliable AE signal analysis methods for real-time monitoring and accurate damage prediction, ultimately reducing downtime and operational costs.

The contributions of this thesis are:

1. The development of advanced AE methods that integrate traditional signal processing techniques with machine learning and deep learning for more effective damage mechanisms monitoring.
2. The introduction of novel deep learning frameworks, such as the FABC-CNN and deep autoencoders frameworks, which significantly improve the accuracy and efficiency of AE signal classification.
3. The application of these methods to real-world aerospace materials, providing valuable insights into damage mechanisms and material behavior under mechanical stress, thereby contributing to more reliable SHM systems in the aerospace industry.

1.3 Document Organization

In Chapter 2, the fundamental concepts related to Aerospace Materials and their degradation mechanisms are discussed. The chapter also introduces the Acoustic Emission technique and its relevance for monitoring damage mechanisms. Various material types and factors influencing material degradation, such as mechanical stress and environmental conditions, are presented.

Chapter 3 focuses on the various AE signal analysis methods. Both traditional non-learning techniques (time-domain, frequency-domain, and time-frequency analysis such as Continuous Wavelet Transform (CWT)) and modern machine learning approaches are detailed. The chapter introduces key techniques for signal processing and explains their role in extracting useful information about material degradation.

In Chapter 4, the mechanical behavior of AlSi10Mg specimens produced via Selective Laser Melting (SLM) is explored. The impact of build orientation on mechanical properties is assessed through tensile testing, while AE signals recorded during the tests are analyzed to monitor damage evolution. This chapter provides a comprehensive understanding of the material's response to stress.

Chapter 5 discusses the classification of AE signals using deep learning techniques. The focus is on the use of Convolutional Neural Networks (CNNs) to classify AE signals based on damage stages (elastic and plastic deformation) and specimen configurations. The performance

of different CNN models, such as AlexNet, SqueezeNet, and a simplified model, is compared in terms of classification accuracy and efficiency.

Chapter 6 introduces the use of the Fuzzy Artificial Bee Colony (FABC)-CNN algorithm to improve AE signal classification. This chapter presents an enhanced methodology that combines FABC with deep learning to address issues such as suboptimal local maxima during model training and overfitting. The approach's robustness and effectiveness in classifying AE signals are demonstrated.

In Chapter 7, a Deep Autoencoder (DAE) framework is used to characterize damage mechanisms in Carbon Fiber Reinforced Polymer (CFRP) composites. The DAE reduces the dimensionality of AE data, and techniques such as K-means clustering, and Hilbert Spectral Analysis (HSA) are applied to identify and classify different damage modes. The complexity of identifying damage in CFRP composites is also discussed.

Finally, the conclusions highlight the effectiveness of the developed methods for AE signal analysis in aerospace applications. Future research directions are proposed, focusing on expanding these methods to other materials and improving damage mechanisms monitoring capabilities for Structural Health Monitoring (SHM) systems.

Chapter 2. Theoretical Background

This chapter provides an overview of aerospace materials, their types, and the degradation mechanisms they are subject to. It also introduces additive manufacturing in aerospace and introduces the acoustic emission technique.

2.1 Aerospace materials and degradation mechanisms

2.1.1 Overview of Aerospace Materials

In the aerospace industry, materials selection is essential for optimum performance, safety and durability under demanding conditions [15], [16]. Over the years, materials have evolved significantly, responding to the industry's growing need for stronger, lighter and more durable components. As aerospace technologies advance, the importance of materials continues to grow, playing a central role in the design of aircraft and spacecraft [15], [17]. Aerospace materials are generally classified into four categories: metallic materials, non-metallic inorganic materials, polymeric materials and composite materials [18]. Each category has distinct properties that make them suitable for specific applications. Metals such as aluminium, titanium and nickel alloys are widely used for their mechanical strength and corrosion resistance, although they present their own difficulties, such as aluminium's susceptibility to corrosion fatigue [19]. Polymer matrix composites (e.g. carbon fiber reinforced polymers, CFRP) offer excellent strength-to-weight ratios, but can be vulnerable to environmental stresses and impact damage [20]. As new materials are developed and refined, their applications in aerospace have extended beyond structural components [21]. They now form an integral part of a range of systems, including engines, propulsion systems, instruments and electronic equipment [22]. The need for enhanced performance, particularly under conditions of extreme temperature and high stress, has led to the development of advanced high-performance composites, superalloys, metal matrix composites (MMC) and ceramic matrix composites (CMC) [23]. These innovations offer superior thermal stability and wear resistance, enhancing the durability and fuel efficiency of modern aircraft [23]. The evolution of aerospace materials has also contributed to increasing aircraft size and performance. Early wood and fabric constructions gave way to metal models, enabling larger, more powerful aircraft to be built, such as those pioneered by Junkers [24]. The trend towards lightweight, durable materials continued. Companies including Boeing and Airbus have incorporated increasing quantities of advanced composites into their latest models (see Figure 2.1) [25]. This has significantly improved fuel efficiency and reduced operating costs. However, there is no "perfect material" for all aerospace needs [26]. Material selection must carefully balance weight, mechanical strength, corrosion resistance and environmental sustainability [27]. This complexity reflects the aerospace industry's general trend towards constant innovation. As materials science advances, new developments will further enhance aircraft performance, paving the way for innovations in civil and military aviation, as well as spacecraft.

2.1.2 Metallic Aerospace Materials

Metallic materials are fundamental to aerospace engineering due to their high strength, durability, and resistance to extreme conditions [28]. From the early use of an aluminium engine by the Wright Brothers to the first all-metal airplane developed by Hugo Junkers using duralumin. Metals such as aluminium, titanium, and steel have played a critical role in aircraft development. These metals are now widely used in modern aircraft structures [29]. The aluminium alloys are highly valued in aerospace for their strength-to-weight ratio and corrosion resistance, making them ideal for components such as fuselages, wings, and support frames [29]. The most commonly used aluminium alloy in aerospace is 7075 aluminium, which is composed of zinc, magnesium, and copper [30]. Table 2.1 shows the composition of 7075 aluminium [30]. Aluminium alloys, heat-treated for improved performance, use temper designations such us T3 and T6 in aerospace [31]

Table 2.1. Composition of 7075 Aluminium Alloy [30]

Element	Percentage
Zinc	5.6% - 6.1%
Magnesium	2.1% - 2.5%
Copper	1.2% - 1.6%

The titanium alloys are recognized for their high strength-to-weight ratio and excellent corrosion resistance [31]. Despite being denser than aluminium, titanium can withstand temperatures up to 600°C, making it suitable for high-stress areas such as engine components, landing gear, and fuselage skins [32]. Titanium's major drawback is its high cost and difficulty in machining [32]. Steel remains important in aerospace, especially for high-stress components like landing gear and engine parts, because of its high tensile strength [33]. There are different types of steel depending on the carbon content, and Table 2.2 provides a summary of low, medium, and high carbon steels, and their applications [33]. Nickel-based superalloys are essential in jet engines and turbines because they maintain strength at temperatures above 1000°C [34]. They also offer excellent corrosion and oxidation resistance [34]. Although expensive, these materials are crucial for ensuring reliability in propulsion systems. Table 2.3 provides a comparison of key properties between aluminium, titanium, and nickel-based superalloys, showing their different strengths and applications [34].

Table 2.2. Types of Steel Used in Aerospace [35]

Type of Steel	Carbon Content	Applications
Low Carbon Steel	0.05% - 0.2%	Secondary structures, ductile components
Medium Carbon Steel	0.2% - 0.8%	Machinable parts, surface-hardened components
High Carbon Steel	0.8% - 1.5%	Springs, wear-resistant part

Table 2.3. Comparison of Key Metallic Aerospace Materials [35]

Material	Strength-to-Weight Ratio	Temperature Resistance	Corrosion Resistance	Typical Application
Aluminium Alloys	High	Moderate (up to 250°C)	Good	Fuselage, wings
Titanium Alloys	Very High	High (up to 600°C)	Excellent	Engine parts, landing gear
Nickel-Based Superalloys	Very High	Very High (1000°C +)	Excellent	Jet engines, turbines

2.1.3 Composite Aerospace Materials

Composite materials have dramatically reshaped the aerospace industry, offering a superior strength-to-weight ratio that has greatly improved aircraft performance [36]. They have gradually replaced traditional materials such as aluminium and steel in critical components, including fuselages and wings [36]. This shift has led to the production of lighter, more fuel-efficient aircraft, signifying a major milestone in the evolution of aerospace manufacturing [37]. Figure 2.1 illustrates the increasing use of composite materials in commercial aircraft by Airbus and Boeing. This shift has led to improved performance and cost efficiency for both companies.

Composite materials are made by combining two or more distinct materials. This process typically results in a new material that is stronger and more efficient than its individual components. These composites consist of:

- Reinforcing phase: The element that provides strength and stiffness, which can be fibers, particles, or flakes.
- Matrix phase: This is the material that binds and surrounds the reinforcing phase, providing shape and stability. The matrix phase is continuous, and when integrated with the reinforcing phase, the composite gains unique properties tailored to specific needs.

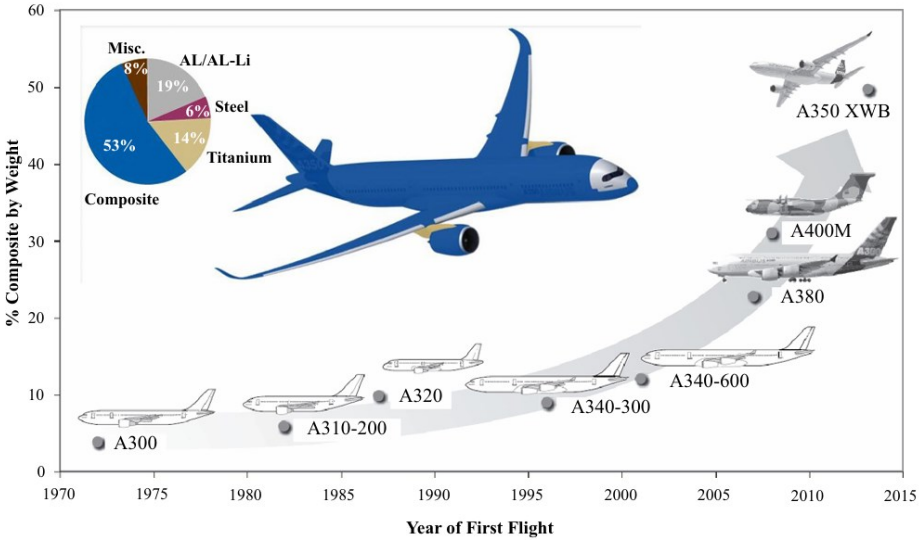

Figure 2.1: Evolution of Composite Materials for Commercial Aircraft: Airbus and Boeing [25]

2.1.3.1 Types of Composites Used in Aerospace

Composites used in aerospace applications are categorized by the type of matrix material they contain. These include:

- Polymer Matrix Composites (PMC): These are the most widely used, known for their low weight and high strength [38]. Carbon fiber-reinforced plastics (CFRP), which combine carbon fibers with a polymer resin matrix, are a good example [39]. The result is exceptionally light and strong materials. CFRPs are often used in key structural components such us fuselages, wings, and tail sections. Glass Fiber-Reinforced Plastics (GFRP) are another type, used in less critical structures where lower strength is sufficient [40].
- Metal Matrix Composites (MMC): These materials offer excellent mechanical properties by combining metals such as aluminium or titanium. They are reinforced with materials including ceramic or carbon fibers. MMCs are often used in high-stress components such as engine parts and landing gear [41].
- Ceramic Matrix Composites (CMC): CMCs are engineered for high-temperature environments. They are commonly used in turbine blades and exhaust systems for their superior thermal stability and wear resistance [42].

The variety of composite materials used in aerospace, along with their matrix and reinforcing phases, can be seen in Table 2.4.

Table 2.4. Classification of Composite Aerospace Materials [43]

Materials	Matrix Material	Reinforcing Material	Applications
Polymer Matrix (PMC)	Polymers/Resins	Carbon fiber (CFRP), glass fiber	Fuselage, wings, tail sections
Metal Matrix (MMC)	Metals (Al, Ti)	Ceramic fibers, carbon fibers	Engine components, landing gear
Ceramic Matrix (CMC)	Ceramics	Ceramic fibers	Turbine blades, exhaust systems

With the increasing reliance on these advanced materials, aerospace design continues to evolve, pushing the boundaries of efficiency, durability, and structural complexity [43].

2.1.4 Additive Manufacturing Materials in Aerospace

Additive manufacturing (AM) or 3D printing has transformed the aerospace industry by enabling lightweight, complex structures unattainable with traditional methods [44]. The layer-by-layer construction process allows for efficient material use, reducing waste and lowering production costs, while offering greater design flexibility [44]. This technology has been adopted in aerospace for various components due to its ability to produce parts quickly and with minimal material waste [45].

AM has been widely adopted in aerospace for producing various parts, including rocket engine components, fuel tanks, and UAV component [44]. The materials used for aerospace parts are typically divided into metallic and polymer components, depending on the criticality of the part [46]. Boeing and Airbus rely on AM for manufacturing and repairing components, with Boeing producing over 20,000 parts using this technology [47]. Notably, AM-fabricated titanium alloy parts have helped Boeing save around $2–3 million per airplane [48]. Airbus, similarly, has incorporated AM technologies into the fabrication of metallic brackets and bleed pipes [47]. Moreover, space agencies such as NASA and SpaceX are investigating the feasibility of using AM to produce igniters, injectors, and combustion chambers for rocket engine [47].

2.1.4.1 Benefits of Additive Manufacturing in Aerospace

The aerospace sector benefits from additive manufacturing for several key reasons (see Figure 2.2):

- Material Efficiency: Additive manufacturing uses only the material required to build each part, minimizing waste compared to traditional subtractive methods [49].
- Weight Reduction: By allowing for optimized internal structures, such as lattice designs, it reduces the weight of components without compromising strength [50]. This is particularly important in aerospace, where lightweight materials are essential for fuel efficiency and emission reduction [50]. As highlighted in Figure 2.2. advantages of AM in aerospace, this weight reduction contributes directly to improved fuel efficiency and overall aircraft performance.
- Design Freedom**:** AM allows for the production of freeform, highly complex shapes that would be difficult to achieve using traditional methods [44]. This makes it possible to optimize parts for both strength and weight, improving performance while reducing material use [47].

- Rapid Prototyping and Production**:** This technology enables fast production of prototypes and parts, speeding up development cycles and reducing time to market [47]

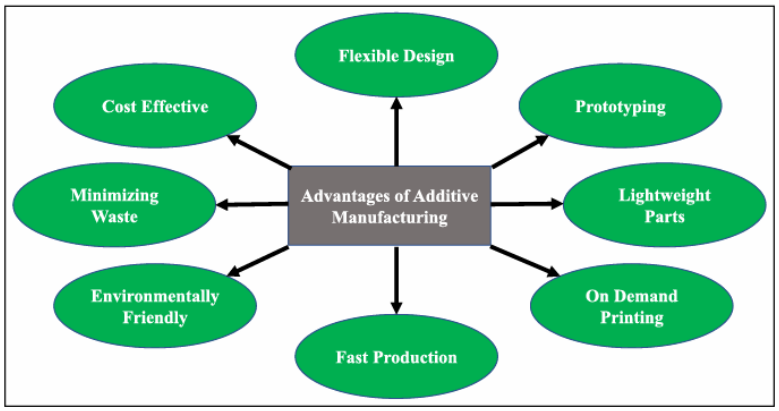

Figure 2.2: Advantages of Additive Manufacturing in the Aerospace [51]

2.1.4.2 Materials Used in Additive Manufacturing for Aerospace

A variety of materials are used in additive manufacturing for aerospace applications, depending on the specific requirements for strength, durability, and environmental [47]

- Metals: Commonly used metals include titanium alloys, aluminium alloys, and nickel-based superalloys for high-performance and high-temperature components [52]. Notably, AM-fabricated titanium parts have become crucial in reducing costs and improving performance in aerospace applications [53].
- Polymers: Lightweight polymers such as PEEK and nylon are utilized for non-critical, non-load-bearing components [54].
- Composites: Emerging in additive manufacturing, composites combine a polymer matrix with reinforcing fibers such as carbon, offering excellent strength-to-weight ratios [55].

2.1.4.3 Additive Manufacturing Techniques

Different additive manufacturing techniques are used to create aerospace components, each optimized for specific materials [47]:

- Selective Laser Melting (SLM): Utilized for metals, SLM uses a high-powered laser to fuse metal powders layer by layer, creating strong, dense parts [56].
- Electron Beam Melting (EBM): Similar to SLM but using an electron beam, primarily for high-performance alloys [57].
- Fused Deposition Modelling (FDM): Used for polymers, FDM extrudes thermoplastics layer by layer to build parts [58].

In this work, the material chosen for the Selective Laser Melting (SLM) process is the AlSi10Mg aluminium alloy. This material is particularly suitable for aerospace due to its:

- High strength-to-weight ratio: AlSi10Mg offers excellent mechanical properties while remaining lightweight, essential for reducing aircraft weight [59].
- Corrosion resistance: The addition of magnesium enhances the alloy's resistance to corrosion, an important factor in aerospace environment [60].

- Good thermal properties: The alloy's ability to handle high temperatures makes it a strong candidate for components exposed to heat during operation [60].

AlSi10Mg is widely used in SLM because it combines the benefits of aluminium alloys with the precision and complexity that additive manufacturing provides. This allows for the production of intricate, strong, and lightweight components, crucial for aerospace applications [59]. Additionally, AM technologies have allowed manufacturers to fabricate parts that meet both weight and strength optimization criteria, significantly improving the efficiency of aerospace components [61].

2.1.5 Degradation Mechanisms in Aerospace Materials

Aerospace structures are exposed to a wide range of stresses during operation, including mechanical, thermal, and aerodynamic forces, as shown in Figure 2.4: Distribution of loads applied to the fuselage of an airliner [62]. These stresses, over time, contribute to the degradation of materials [62]. They can lead to various failure modes depending on the type of material, the structure, and the nature of the applied loads [62]. Identifying these degradation mechanisms and understanding how they develop are crucial for long-term performance and safety [63]. Assessing their impact on the integrity of aerospace structures is equally important. The following sections provide an overview of the most common degradation mechanisms observed in aerospace materials [64].

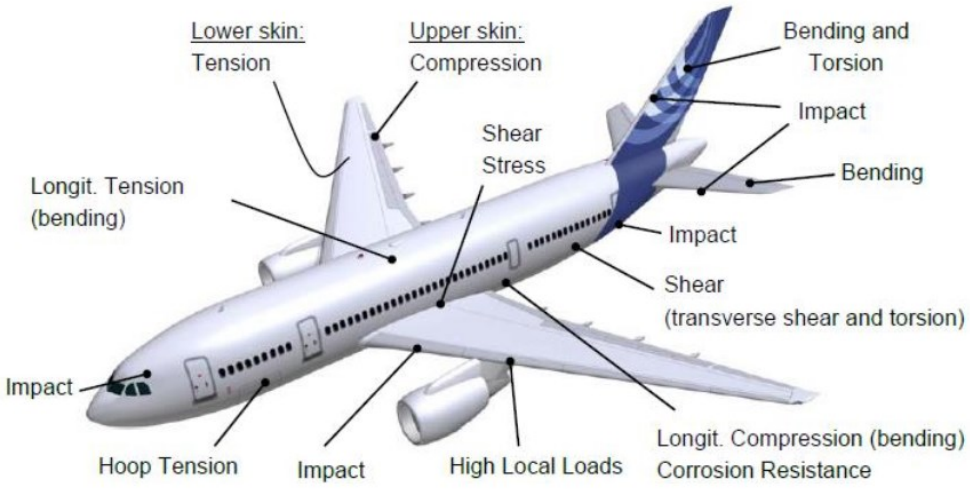

Figure 2.3: Distribution of loads applied to the fuselage of an airliner [62]

2.1.5.1 Degradation Mechanisms in Metals

Metals used in the aerospace industry are subjected to various environmental and operational stressors, leading to degradation over time [65]. Several key degradation mechanisms, such as corrosion, fatigue, creep, and wear, affect metal components in aerospace [66]. Understanding these mechanisms is crucial for maintaining aircraft safety, performance, and longevity.

2.1.5.1.1 Corrosion

Corrosion remains a significant issue for metals used in aerospace due to exposure to moisture, salts, and other environmental factors [67]. Metals as aluminium and titanium, common in aerospace structures, can form protective oxide layers. However, under certain conditions, these layers may break down, leading to various types of corrosion.:

- Uniform Corrosion: A generalized form of corrosion that thins the metal uniformly over time.
- Galvanic Corrosion: Occurs when two dissimilar metals are in contact, causing one to corrode preferentially in the presence of an electrolyte.
- Pitting Corrosion: Localized corrosion forming pits or holes that can weaken structural integrity.
- Stress Corrosion Cracking: A dangerous form of corrosion where tensile stresses cause cracking in a corrosive environment [68].

Appropriate material selection can reduce the likelihood of corrosion, though it remains a critical concern in aerospace applications.

2.1.5.1.2 Fatigue

Fatigue is considered one of the dominant causes of metal failure in aerospace [69]. Fatigue cracking occurs due to cyclic loading, where repeated application of stress leads to the formation and propagation of cracks [70]. Even if the applied load is below the material's yield strength, the repeated stress cycles can lead to failure over time.

Findlay and Harrison emphasize that aerospace components are generally designed with safety factors to prevent failure from yielding or brittle fracture [71]. However, fatigue cracking remains the main mode of failure, particularly in areas such as joints. Load transfer zones and stress concentrators, such as holes, cross-section changes and cut or forged areas. Fatigue failure accounts for over 60% of metal failures in aerospace structures, particularly in assemblies and load transfer areas [72] .

The fatigue cracking process can be divided into three stages:

a) Crack Initiation: Small cracks begin to form at micro-level imperfections or stress concentrators. These cracks often initiate in regions with slip bands, where repeated stress causes dislocation movements, leading to the formation of microscopic intrusions and extrusions at the material surface [73]. Surface flaws or manufacturing defects, such as micro notches, can also promote crack initiation [74].
b) Crack Propagation: Once initiated, cracks grow progressively under cyclic loading. The propagation consists of three phases:
    - Stage I (Microcrack Growth): Slow growth, heavily dependent on grain orientation.
    - Stage II (Long Crack Growth): The crack propagates perpendicularly to the tensile stress direction.
    - Stage III (Brittle Fracture): Final, unstable crack growth leading to complete material failure [75].
a) Final Failure: The remaining material can no longer support the load, leading to sudden failure [71].

Fatigue cracking is often subtle and difficult to detect until it reaches an advanced stage. Regular inspections and non-destructive testing (NDT) are crucial to identifying cracks early and preventing catastrophic failure [76]. The Paris Law, developed in 1961, provides a method for predicting crack growth under cyclic loading conditions based on stress intensity and crack growth rate [77].

2.1.5.1.3 Creep

Creep is the gradual, permanent deformation of metals under long-term stress, particularly at high temperatures [78]. In aerospace, creep primarily affects high-temperature components such as turbine blades [79], [80]. This slow deformation is dangerous because it can accumulate over time, leading to significant changes in component shape and mechanical properties [81]. High-performance alloys, such as nickel-based superalloys, are often used to mitigate creep effects in aerospace applications [82].

2.1.5.1.4 Wear

Wear refers to the progressive loss of material from the surface due to mechanical interactions such as friction or contact with other surfaces [83]. Components subjected to frequent movement, such as gears, bearings, and hydraulic parts, are prone to wear. In aerospace, wear can manifest as:

- Abrasive Wear: Caused by harder materials scratching or gouging the surface of softer metals.
- Adhesive Wear: Occurs when materials transfer between surfaces under sliding conditions.
- Fretting Wear: A combination of wear and corrosion in areas of small oscillatory movements, typically seen in mechanical joints and fittings [84].

Wear can significantly impact the lifespan of aerospace components, and regular maintenance and monitoring are essential to mitigate its effects [85].

2.1.5.2 Statistical Analysis of Failure Modes

Studies reveal that fatigue is the most common cause of metal failure in aerospace applications, accounting for over 55% of observed failures, followed by overload, corrosion, and wear [71]. Table 2.5 provides a breakdown of damage modes observed in aerospace components:
Fatigue failures are often concentrated around stress concentrators such as joints and load transfer areas, where cracks initiate due to cyclic stress [71].

Table 2.5. Statistical analysis of failure modes [71]

Modes of Failure	Failure Percentage (%)
Corrosion	16
Fatigue	55
Overload	14
High-Temperature Corrosion	2
Cracking/Fatigue Corrosion	7
Creep	1
Abrasion/Erosion	6

2.1.5.3 Degradation Mechanisms in Composite

The degradation of composite materials differs significantly from that of metals, as it occurs in a more dispersed manner across various scales [86]. Composite materials experience degradation through complex interactions at both microscopic and macroscopic levels [83]. Common degradation modes in composites include matrix cracking, fiber-matrix debonding,

fiber fracture, and delamination, with failure often resulting from the accumulation of these damage modes.

2.1.5.3.1 Delamination

Delamination is a critical and frequent failure mode in composite materials, especially in aerospace structures. It involves the separation of layers within a composite due to stress, impact, or manufacturing defects. Stress concentrations, such as those at free edges, drilled holes, sharp angles, or abrupt section changes, are common initiation points for delamination [87]. As delamination spreads, it significantly reduces the structural integrity of the composite. This degradation leads to issues such as stiffness loss and potential buckling under compressive loads [88]. The process begins with micro-damage, such as matrix cracking and fiber-matrix debonding, which coalesce into larger transverse cracks [89]. These cracks propagate between plies of different orientations, leading to interlaminar fracture. Environmental factors like temperature variations and humidity can worsen delamination [87]. They induce shear stresses between layers with different thermal expansion properties.

2.1.5.3.2 Matrix Cracking

Matrix cracking typically initiates the degradation process in composites. Cracks form within the matrix material, often due to cyclic loading or environmental stress [90]. Although matrix cracking alone may not cause immediate failure. It compromises the material by enabling other damage modes, as delamination, to occur [91]. Matrix cracking requires relatively low energy, particularly in brittle composites like carbon/epoxy laminates [92].

2.1.5.3.3 Fiber Breakage

Fiber fracture is a more severe form of damage that often leads to catastrophic failure in composite materials. Stress concentrations, such as those caused by matrix cracks, can trigger fiber breakage. Once fibers begin to fracture, the composite's load-bearing capacity is greatly diminished, which can result in sudden failure [93]. Fiber fracture can be initiated by various loading conditions, including impacts and fatigue cycling.

2.1.5.3.4 Fiber Debonding and Pull-Out

Fiber debonding occurs when the bond between the fibers and matrix weakens, leading to separation [94]. This damage mode can result from fatigue loading, environmental exposure, or impact. When severe, fibers may be completely pulled out of the matrix, further reducing the composite's strength [95]. Fiber debonding reduces the ability of the composite to transfer load effectively between fibers and matrix, thereby weakening the overall structure.

2.1.5.3.5 Environmental Degradation

Environmental factors, such as moisture and temperature fluctuations, can accelerate composite degradation [96]. Moisture absorption causes swelling, reduces stiffness, and may lead to microcracking [97]. High temperatures, on the other hand, can degrade the polymer matrix, reducing the composite's mechanical properties [96]. These environmental effects not only degrade the material directly but also amplify other damage modes, such as delamination and matrix cracking [96].

2.2 Fundamentals of Acoustic Emission Technique

2.2.1 Introduction

Acoustic Emission refers to the generation of transient elastic waves caused by the sudden release of energy within a material under stress [98]. According to EN 1330-9:2017, AE is defined as "transient elastic waves generated by the release of energy in a material or process. When a structure is subjected to external stimuli, such as changes in pressure, load or temperature, localized microcracks release energy that propagates as stress waves detected by surface-mounted sensors. As an NDT technique, AE is unique in that the material generates the signal, unlike methods as ultrasound or X-ray tomography, which require external energy input [99]. AE enables real-time monitoring of large structures with minimal sensors, detecting active defects as they evolve [100]. However, AE is limited to identifying progressive defects and cannot map the size or precise location of pre-existing damage. Historically, Joseph Kaiser's work in the 1950s identified the Kaiser Effect, where a material does not emit AE signals if reloaded below its previous maximum stress [100]. AE has since become a cornerstone in Structural Health Monitoring (SHM) and damage characterization. Studies on materials, including aluminium and copper, have shown that AE strongly correlates with internal structural changes under mechanical stress. This correlation provides insights into phenomena including dislocations and phase transformations [101].

2.2.2 Sources of Acoustic Emission in Materials

The AE signals come from different sources in stressed materials, associated with internal structural changes. These sources can be divided into two main categories: mechanical sources and artificial sources, each producing distinct types of AE signals that are vital for understanding material behavior [102].

2.2.2.1 Mechanical Sources of Acoustic Emission

Mechanical sources of AE are directly related to the material's response to external mechanical loads, such as tension, compression, or thermal stress [103]. These sources are primarily responsible for AE signal generation in aerospace materials and provide essential information about the material's degradation and damage mechanisms [103]. Mechanical sources in metals and composites can be categorized as follows:

a) Micro-cracking: The initiation and propagation of micro-cracks release energy in the form of transient elastic waves, detectable as AE signals [104]. This phenomenon is a primary indicator of damage in materials such as aluminium alloys and CFRP composites, making it critical for early detection in aerospace structures.
b) Dislocation Movement: In crystalline materials, particularly in aluminium alloys, cooperative dislocation movement under stress produces AE signals [105]. While a single dislocation movement is not detectable, the collective motion of dislocations generates detectable signals, providing insights into plastic deformation processes.
c) Phase Transformations: Some materials are subject to phase transformations as a result of stress or temperature changes [106]. For example, martensitic transformation in

certain alloys releases energy that can be captured as AE signals. These transformations often indicate significant microstructural changes that may precede failure.

d) In composite materials such as CFRP, AE signals are generated during matrix cracking, delamination, and fiber breakage, under mechanical loads (see Figure 2.4) [107]. These signals are crucial for monitoring the integrity of the material, as they indicate the initiation and progression of damage within the composite structure.

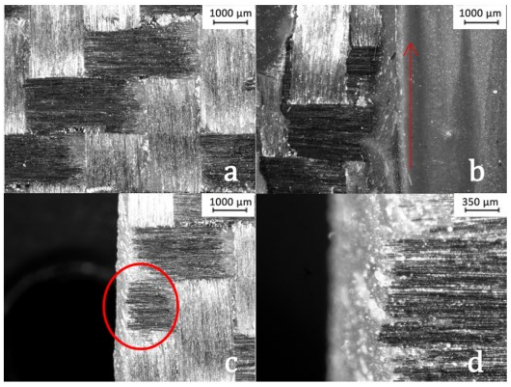

Figure 2.4: Illustrates typical AE signal sources in composite materials, (a) Fiber/Matrix debonding; (b) Delamination; (c) Fiber breakage; (d) Close in view fiber breakage [108]

2.2.2.2 Artificial Sources AE Signals

Artificial sources of acoustic emissions are employed to replicate a material's response to stress and validate the precision of acoustic emission systems [103]. They are extensively used for sensor calibration and the validation of experimental configurations. Prevalent artificial sources comprise:

a) Pencil Lead Break (PLB): The predominant method, entailing the fracture of a standardized 2H pencil lead against the material's surface. This produces dynamic AE signals, beneficial for sensor calibration and source localization [109].

b) Artificial Crack Propagation: Deliberate cracking or deformation to examine material behavior in a regulated setting, offering insights into how damage mechanisms generate acoustic emission signals [110].

c) Impact and Friction: Regulated impacts or friction between surfaces replicate authentic operational situations, producing AE signals for aircraft applications [111].

These sources essentially fulfil two functions: calibrating acoustic emission systems and analysing signal properties [112]. The PLB approach generates burst-type signals similar to those produced by micro-cracks, thus providing precise system calibration.

2.2.3 Types of AE Signals

The AE signals can be classified into two main types: burst-type and continuous-type signals, each corresponding to specific material behaviors and damage mechanisms [113]. These classifications help in understanding the nature of damage progression within materials, especially in high-performance aerospace materials [35]. The Burst-type signals are short, high-energy emissions associated with discrete events such as crack initiation, crack propagation, or fiber breakage [114]. Each signal represents a distinct damage event and is characterized by its transient nature and high amplitude, indicating significant energy release.

For instance, in composite materials, matrix cracking or fiber rupture produces burst-type signals, while in metals, such signals are often linked to crack initiation and growth [115]. These burst signals are critical for identifying localized damage and assessing the structural integrity of materials.

The Continuous AE signals are sustained, lower-energy waveforms associated with prolonged activities such as plastic deformation or friction between surfaces[116]. These signals arise when the material undergoes gradual deformation, leading to a continuous release of energy. Figure 3. illustrates the burst-type AE signal and Continuous [116].

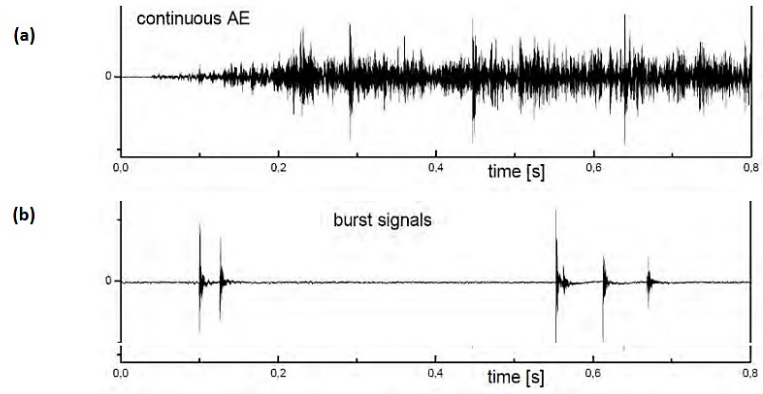

Figure 2.5: (a) continuous-type AE signals and burst-type AE signals (b) [115]

In this thesis, burst-type AE signals are of particular interest because they provide detailed information about significant damage mechanisms, including matrix cracking and fiber rupture. These signals are critical for assessing the health and integrity of aerospace. Where early detection of localized damage is essential for preventing structural failure [117].

2.2.4 Propagation of AE Signals as Stress Waves

The propagation of Acoustic Emission signals follows fundamental principles of wave mechanics. Elastic waves that propagate through a solid material are produced by disturbances within the material [118]. These waves are produced by stress redistributions, such as crack formation or phase transformations. They can be described by wave equations, which are often simplified into the Helmholtz equation for practical analysis [119]. The solution to this equation helps explain various wave behaviors, including progressive and stationary waveforms, as well as interactions with obstacles in the material.

2.2.4.1 Types of Elastic Waves in Solids

a) Primary (Longitudinal) Waves

Longitudinal waves, also called P-waves, involve particle motion that is parallel to the direction of wave propagation [120] The particles undergo compression and dilation as the wave moves forward. The driving component of longitudinal waves acts normal to the wavefront, which is the plane of the wave (see Figure 2.6). These waves are the fastest among elastic waves, hence they are referred to as primary waves. Their high velocity in solids makes them crucial for detecting internal structural damage, as they propagate quickly and carry significant energy. The velocity of longitudinal waves, C_L is expressed as shown in the provided equation (2.1):

$$C_L = \sqrt{\frac{(1-\upsilon)E}{(1+\upsilon)(1-2\upsilon)\rho}} \qquad (2.1)$$

Where, E represents Young's modulus. υ is the Poisson's ratio, indicating lateral deformation. ρ is the density, representing mass per unit volume of the material.

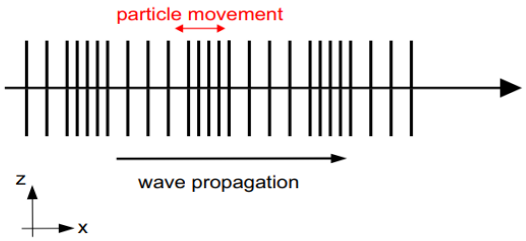

Figure 2.6: Illustration of Longitudinal wave propagation [121]

b) Secondary (Transverse) Waves

In transverse waves (S-waves), particles move perpendicularly to the wave's direction of propagation (see Figure 2.7). These waves, also known as shear waves, can travel through solids but not through liquids or gases, as shear forces cannot develop in fluids. The velocity of transverse waves, C_T , is given by the equation (2.2):

$$C_T = \sqrt{\frac{E}{2(1+\upsilon)\rho}} \qquad (2.2)$$

Where E is Young's modulus, υ is Poisson's ratio, and ρ is density.

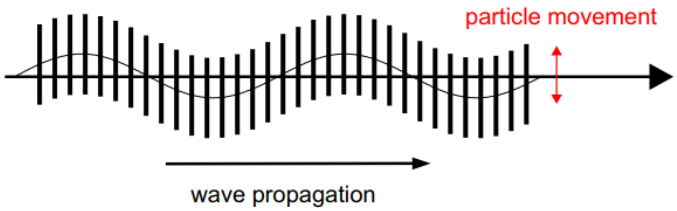

Figure 2.7: Illustration of transverse elastic waves [121]

c) **Surface Waves**: Rayleigh and Lamb Waves

The surface waves are slower than body waves but exhibit higher amplitudes, making them valuable for surface-level damage detection:

Rayleigh waves involve a combination of longitudinal and transverse motions, propagating along the surface of solids. The particles move in elliptical trajectories, and these waves decay exponentially with depth. The velocity of Rayleigh waves C_R can be approximated by the equation (2.3):

$$C_R = \frac{(0.87-1.12\upsilon)}{(1-\upsilon)} C_T \qquad (2.3)$$

Lamb waves, also called "plate waves," propagate through thin materials, guided by the plate's boundaries. They operate in two primary modes: extensional (symmetric), which resembles shear horizontal waves, and flexural (antisymmetric), similar to shear vertical waves (see Figure 2.8). Lamb waves can travel long distances with minimal energy loss, making them

highly efficient for inspecting large surface areas [122]. Their ability to detect both surface and internal defects. The velocity of Lamb waves in the extensional mode, denoted as C_E , is given by the equation (2.4):

$$C_E = \sqrt{\frac{E}{\rho(1-\upsilon^2)}} \quad (2.4)$$

Where E is Young's modulus, which measures the stiffness of the material. ρ represents the density of the material. υ Poisson's ratio, which relates the material's lateral strain to its axial strain. It represents how these factors influence the speed of wave propagation when the material experiences symmetric deformation. On the other hand, the flexural mode velocity is represented by the equation (2.5):

$$C_F = \sqrt[4]{\frac{D\omega}{\rho h}} \quad (2.5)$$

This equation focuses on the flexural Lamb waves, which are more sensitive to lower frequencies. The velocity is influenced by the bending stiffness of the plate D, the angular frequency ω, the material density ρ, and the thickness of the plate h. As flexural waves are dispersive, their velocity varies significantly with frequency, unlike extensional waves which have a relatively constant velocity over different frequencies.

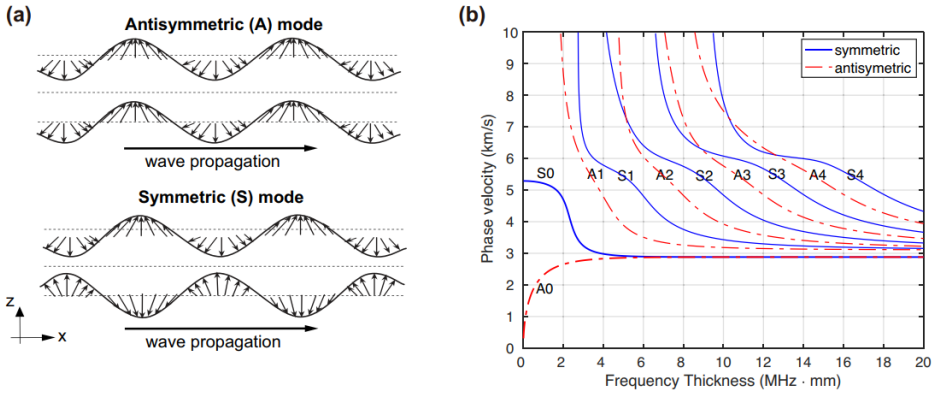

Figure 2.8: Illustration of antisymmetric (a) and symmetric (S) Lamb modes propagating in a plate. (b) Dispersion curves of Lamb modes for an aluminium plate [121]

2.2.5 Mechanisms of Wave Attenuation and Dispersion

Attenuation and dispersion are key factors that impact AE wave propagation through materials. They directly affect the signal quality and its interpretation in SHM systems.

2.2.5.1 Attenuation Mechanisms

Attenuation refers to the reduction of a wave's amplitude as it travels through a medium. Several key factors contribute to this phenomenon:

a) Geometric Spreading**:** As AE waves propagate, their energy disperses over an increasing area, leading to a reduction in amplitude. Energy conservation dictates that

the amplitude diminishes by approximately 30% each time the distance from the source is doubled [123]. This reduction is most prominent during the initial stages of wave propagation.

b) Absorption**:** The wave's kinetic and elastic energy is partially converted into heat as it travels through the material. This process is more pronounced at higher frequencies, resulting in greater attenuation of high-frequency AE signals compared to lower-frequency signals [124].
c) Energy Dissipation into Adjacent Media**:** When AE waves encounter material boundaries or discontinuities, part of the energy is reflected back into the material. The remaining energy is transferred to the surrounding media, which leads to further attenuation of the signal [125].

2.2.5.2 Wave Dispersion

Wave dispersion occurs when the different frequency components of a wave travel at different speeds, causing the wavefront to stretch out as it propagates [126]. This effect is particularly notable in guided waves, such as Lamb waves, where the wave's speed varies based on both frequency and the material's properties. Dispersion reduces the peak amplitude of the wave and complicates signal interpretation, though it also provides information about material characteristics [103].

2.2.6 Sensors and acquisition system

Sensors and Acquisition Systems play a critical role in capturing and analyzing AE signals. These systems detect the acoustic waves, produced by internal changes within a material under stress. These acoustic waves are converted into electrical signals by AE sensors and processed through acquisition systems. The choice of sensors and the configuration of the acquisition system are fundamental to obtaining high-quality AE data.

2.2.6.1 Types of AE Sensors

AE sensors are mainly piezoelectric, due to their high sensitivity and ease of installation. These sensors operate on the piezoelectric effect, where mechanical strain or displacement generates an electrical charge. When subjected to mechanical stress, piezoelectric materials like Lead Zirconate Titanate (PZT) generate an electrical charge due to the disruption of their internal structure. A cylindrical PZT sensor, bonded to a metal housing, is shown in Figure 2.9.

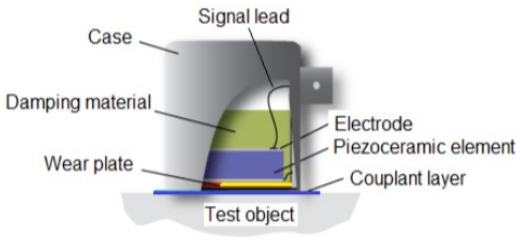

Figure 2.9: Schematic diagram of a typical ac acoustic emission PZT sensor [127]

There are two types of piezoelectric sensors used in AE such as:

a) Resonant Sensors**:** These sensors detect specific frequencies with high sensitivity but operate within a narrow frequency range. They are particularly useful when focusing on detecting certain high-frequency events, though the limited bandwidth can constrain the detection of broader signal spectra.
b) Broadband Sensors**:** These sensors respond uniformly over a broad frequency range. While less sensitive than resonant sensors, their ability to capture a wide range of frequencies makes them ideal for analyzing a variety of AE signals from different sources. This type is widely used in situations where the full spectrum of AE activity is essential for accurate diagnostics.

The Figure 2.10 illustrates two types of Acoustic Emission sensors along with their corresponding frequency responses.

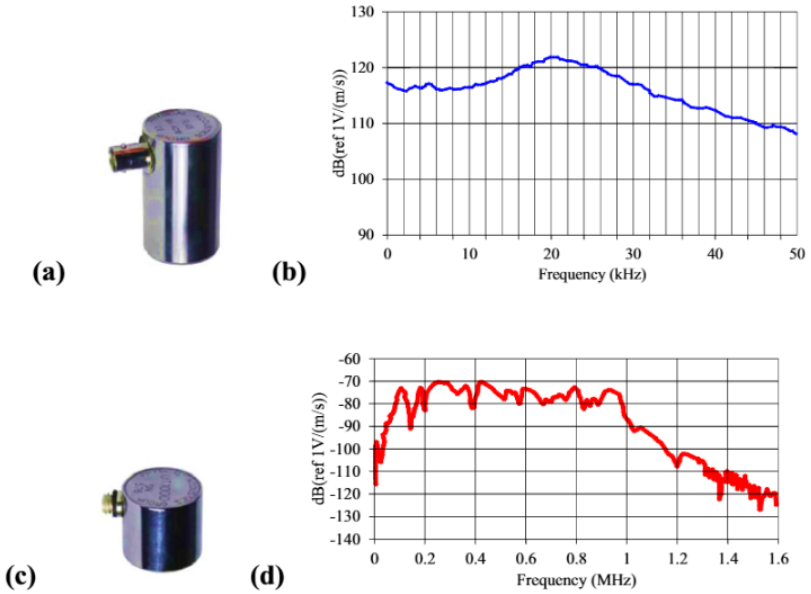

Figure 2.10: Illustration of two different AE sensor types along with their respective frequency responses. (a), (b)A resonance-type sensor and (c), (d) A broadband-type sensor

2.2.6.2 Signal Amplification and Acquisition Systems

AE signals are typically weak and require amplification to be effectively analyzed. Amplification is performed in two stages:

a) A preamplifier, positioned near the sensor, amplifies the raw signal.

b) The main acquisition system amplifies the signal further, typically by 40-60 dB.

The acquisition system also includes filters to eliminate background noise and isolate the true AE signals. Systems such as the Physical Acoustic MISTRAS PCI-2, manufactured by Physical Acoustics Corporation (USA), include multiple channels for signal recording and provide advanced filtering options. More information about this system can be found on the

manufacturer's website (www.physicalacoustics.com) and in the corresponding technical datasheet. Important acquisition parameters include:

- Threshold: The minimum amplitude required to register an AE event.
- Peak Definition Time (PDT): Determines the peak of the AE signal.
- Hit Definition Time (HDT): Defines when an AE event ends.
- Hit Lockout Time (HLT): Prevents overlapping hits from being confused with separate events.

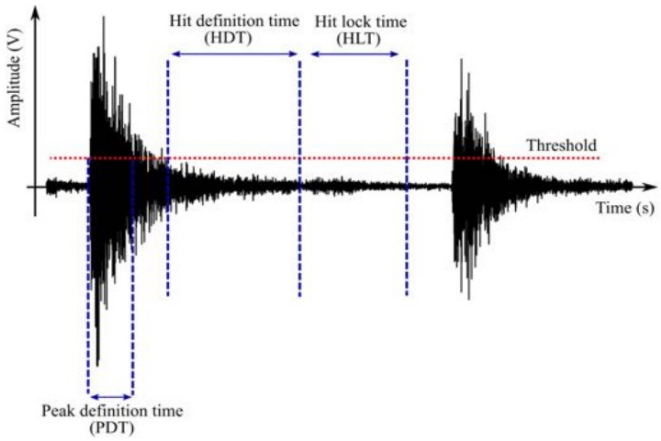

Figure 1-11: Representation of acquisition parameters [128]

2.2.7 Conclusion

In this chapter, we first explored aerospace materials, and the degradation mechanisms associated with them. The various factors that contribute to material degradation in aerospace applications. Particularly mechanical stresses, thermal fluctuations and environmental conditions, were examined in detail. In addition, additive manufacturing was presented as an important innovation in aerospace, offering flexibility in design and manufacture.

The chapter also introduced acoustic emission technique as an important tool for monitoring damage mechanisms in aerospace materials. The theory of AE wave propagation, and the acquisition system were briefly discussed. In this thesis, the phenomenological approach to AE will be used to establish links between AE signals and damage mechanisms in complex aerospace materials during mechanical testing. This approach requires a solid understanding of signal processing, pattern recognition and deep learning algorithms, which will be developed in Chapter 3. This fundamental knowledge of materials and AE paves the way for the advanced analyses and methodologies that will be developed in the following chapters.

Chapter 3. Methods for Acoustic Emission Signal Analysis

This chapter presents the methods for analyzing AE signals to assess degradation mechanisms in materials under tensile testing. The focus is on recording AE waveforms for more detailed and accurate damage interpretation. Traditional methods, including temporal, frequency, and time-frequency analysis, are used to extract key features. Additionally, convolutional neural network (CNN) models were developed to enhance AE signal classification. A data augmentation technique was implemented to increase the available data. By combining traditional methods with deep learning, this work aims to improve the analysis of AE signals and understanding of aerospace material damage.

3.1 Non-Learning Methods for Acoustic Emission Signal Analysis

In general terms, ‘’non-learning ‘’ methods refer to the classical approaches to statistical analysis that are used to analyse and interpret AE signals. These methods are based on traditional approaches in the time, frequency and time-frequency domains, which aim to extract descriptors relevant to the evaluation of AE signals. In the time domain, the descriptors are derived directly from the raw signal and include features such as maximum amplitude, duration, energy, threshold count and others. These characteristics make it possible to evaluate the intensity and duration of acoustic events, providing an initial qualitative analysis of the signal. Frequency approaches rely on the use of Fast Fourier Transform (FFT) to analyse the frequency components of the AE signal. This facilitates the detection of the predominant frequencies in the signal, thereby revealing crucial data about the nature of underlying phenomena such as cracks and fractures. In addition, time-frequency methods integrate both the temporal and frequency aspects to enable a more in-depth analysis of the AE signal. These methods include the Continuous Wavelet Transform (CWT) and the Hilbert-Huang Transform (HHT). These techniques are particularly effective for analysing transient and non-stationary signals, which are characteristic of AEs, giving a more in-depth and detailed view of the temporal and frequency dynamics of the AE signal. The non-learning methods used in this thesis will be presented in the following sections. They include feature extraction in the time, frequency and time-frequency domains. Each approach will be described and applied to the analysis of AE signals.

3.1.1 Time-domain AE descriptors

Time-domain acoustic descriptors play a fundamental role in analyzing AE signals. These time-domain descriptors such as amplitude, duration, rise time, and energy provide essential information about AE events (see Figure 3.1, Table 3.1) [129]. Helping in understanding the behavior of materials under stress, identifying damage mechanisms, and monitoring structural integrity. However, material heterogeneity can affect signal propagation, potentially masking results in practical applications. Advanced signal processing techniques, including non-parametric methods, are used to extract relevant information from AE signals, aiding in source localization and severity assessment [130]. These approaches contribute to the development of

effective structural health monitoring systems. In this research, acoustic emission waveforms are captured using the Physical Acoustic (MISTRAS) PCI-2 system, and the features are subsequently extracted and analyzed through an external MATLAB-based software.

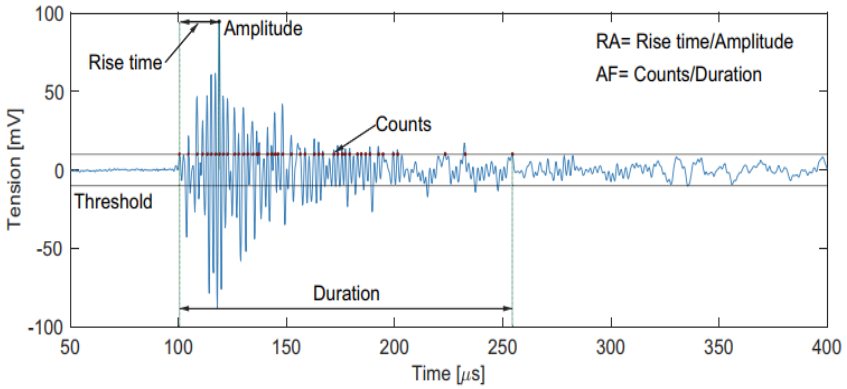

Figure 3.1: Time Feature Extraction from Acoustic Emission Signal x(t)[121]

Table 3.1. AE time domain Features calculated from AE waveform

ID	Descriptor	Units	Description
1	Duration	μs	The time between the first and last threshold crossing of the AE signal.
2	Amplitude	dB, V	The highest voltage or decibel level reached during the AE event.
3	Energy	J	The total energy released, often calculated as the area under the squared signal.
4	Rise Time	μs	The time from the beginning of the signal to its maximum amplitude.
7	Counts	–	The total number of times the signal crosses a defined threshold.
8	Counts to Peak	–	The number of threshold crossings from the start of the signal to its peak.
9	Rise Angle (RA)	–	Calculated as tan^ (-1)(Amplitude / Rise Time), providing a measure of the signal slope.
10	Rise Time/Duration	–	The ratio of rise time to the total signal duration.
12	Duration/Amplitude	μs	The ratio between the total duration of the signal and its peak amplitude.

14	Counts/Duration	–	A ratio describing the signal activity, measured by dividing counts by duration

3.1.2 Frequency domain AE features

Frequency-domain features are essential for analyzing the spectral content of AE signals. These features transform the signal from the time domain to the frequency domain. Techniques such as the Fast Fourier Transform (FFT) enable this transformation. Frequency-domain features reveal frequency distribution, energy concentration, and signal patterns. These insights are often hidden in the time domain. Frequency-domain analysis plays a key role in identifying different modes of damage mechanisms or material degradation that are responsible for the AE events[131]. The Fourier Transform (FT) mathematically converts a time-domain signal $x(t)$ into its frequency-domain counterpart $\hat{x}(f)$. The FT and its inverse are expressed as:

$$\hat{x}(f) = \int_{-\infty}^{\infty} e^{-2\pi i f t} x(t)\, dt \qquad (3.1)$$

And

$$x(t) = \int_{-\infty}^{\infty} e^{2\pi i f t} \hat{x}(f)\, df \qquad (3.2)$$

Here, $\hat{x}(f)$ is a complex-valued function that provides both the magnitude and phase of each frequency component in the signal. The magnitude $|\hat{x}(f)|$ reveals the amplitude of the signal's frequency components, while the phase relates to their timing [132]. In this study, we used the FFT, an efficient algorithm based on the Discrete Fourier Transform (DFT), to compute the spectral content of AE signals. By applying the FFT, we transformed the AE signal from the time domain into the frequency domain, revealing its spectral characteristics. his spectral information is essential for extracting features such are critical for understanding the nature of the AE events [133].

3.1.3 Time-frequency AE features

3.1.3.1 Continuous Wavelet Transform for AE Signal Processing

The Continuous wavelet transform (CWT) is a signal processing technique which extracts the time domain content of acoustic emission signals [134]. The CWT has been successfully used to characterize damage modes in materials and structures. Grabowska et al. performed structural health monitoring (SHM) using AE and wavelet analysis [133]. Li et al. monitored damage in metal panel damage using AE and the adaptive enhancement variational mode decomposition wavelet packet transform [135]. Burud et al. detected damage in concrete subjected to bending using AE and wavelet entropy [135]. Baccar et al. detected wear using acoustic emission wavelet analysis of AE [136]. The CWT is described by equation (3.3).

$$CWT_f(a,b) = \int_{-\infty}^{\infty} f(x)\overline{\zeta_{a,b}(x)}dx, \qquad a \succ 0, \qquad (3.3)$$

$$\zeta_{a,b}(x) = \frac{1}{\sqrt{a}}\zeta\left(\frac{t-b}{a}\right), \qquad a,b \in R, a \neq 0 \qquad (3.4)$$

where, $\zeta_{a,b}(x)$ is the mother wavelet described by equation (3.4), a parameter that determines the size of the wavelet, b sets shift along the time axis (t), $f(x)$ is decomposed into wavelet coefficients, and $1/\sqrt{a}$ maintains the wavelet energy constant at varying scales.

Several types of mother wavelets exist, such as the Morlet, Mexican, and Gaussian wavelets. The Morlet wavelet is more suitable for broadband signals due to its time-based frequency and scale properties [137]. In this study, the Morlet wavelet is used as the basis function for generating CWT scalograms of AE signals. Gao et al. provided more detailed of CWT [134]. In this thesis, the Implementation CWT algorithm is performed on the MATLAB® (2023a) environment.

3.1.3.2 Hilbert-Huang Transform for AE Signal Processing

Hilbert Spectrum Analysis (HSA) uses the Hilbert transform (HT) to determine instantaneous frequency and energy for signal analysis [138]. HT has been widely used to characterize material damage modes using AE signals [139], [140], [141]. In this study, the HSA is applied to the AE signals. The HT, $h[x(t)]$, is defined by the equation (3.5):

$$h[x_i(t)] = \frac{1}{\pi} p \int_{-\infty}^{+\infty} \frac{x_i(\tau)}{t-\tau} d\tau \quad (3.5)$$

Where P represents the principal Cauchy value, $\hat{x}(t)$ represents the reconstruct AE signal τ is a variable of integration, representing the time delay over which the convolution is performed and t is the specific time at which the Hilbert transform is evaluated. The analytical signal $A(t)$ corresponding to $x(t)$ is defined as follows:

$$A_i(t) = x_i(t) + jh[x_i(t)] = a_i(t)e^{j\varphi_i(t)} \quad (3.6)$$

With, $a_i(t)$ the instantaneous amplitude of $x(t)$, while φ_i is the instantaneous phase of $\hat{x}(t)$.

$$a_i(t) = \sqrt{x^2(t) + h^2[x_i(t)]} \quad (3.7)$$

$$\varphi_i(t) = arctan(\frac{h[x_i(t)]}{x_i(t)}) \quad (3.8)$$

By calculating the derivative of the instantaneous phase $\varphi_i(t)$, the instantaneous frequency $\omega_i(t)$ is determined as:

$$\omega_i(t) = \frac{d\varphi_i(t)}{dt} \quad (3.9)$$

After integrating the transient frequencies and transient amplitudes, the Hilbert time-frequency spectrum is calculated as follows:

$$H(\omega,t) = \sum_{i=1}^{n} a_i(t)e^{j\int \omega_i(t)dt} \quad (3.10)$$

From a statistical standpoint, the marginal spectrum reflects the cumulative distribution of amplitude at each frequency in the data. The presence of specific energy frequencies in the signal suggests the existence of corresponding waveforms. In other words, the marginal

spectrum allows for a more precise analysis of the actual frequency components present. Compared to conventional methods, this approach, which directly utilizes signals reconstructed by the decoder, is promise as it effectively reduces signal noise, thereby enabling an efficient application of the Hilbert spectrum. In the context of this thesis, this algorithm is implemented using MATLAB® 2023a software.

3.2 Learning Methods for Acoustic Emission Signal Analysis

Learning methods for acoustic emission (AE) analysis differ from traditional approaches. They use machine learning and deep learning techniques. These methods automatically identify patterns in AE signals. They classify events and improve the accuracy of signal interpretation. Unlike traditional methods, they do not rely on manual feature extraction. Instead, they leverage data-driven techniques to uncover complex relationships in the data, whether through clustering or advanced image-based and raw waveform analysis.

Significant advancements have occurred in the domain of artificial intelligence (AI) in recent years. This led to new possibilities for the analysis of complex data, including acoustic emission (AE) signals. These advancements have led to the development of advanced methods to enhance the classification and interpretation of AE data. One recent approach combines the Continuous Wavelet Transform (CWT) with Convolutional Neural Networks (CNNs). The CWT, a time-frequency method, generates scalograms when applied to AE signals. These scalograms, are used as images to serve as inputs to train deep learning models. CNNs, renowned for their effectiveness in image recognition, are particularly well-suited for this task. They have shown great potential in improving the accuracy of AE signal classification.

3.2.1 Clustering Techniques for Acoustic Emission Signal Analysis

3.2.1.1 K-Means Clustering for Acoustic Emission Data

The k-means algorithm, which was initially introduced in the 1950s, is still one of the most commonly used techniques for unsupervised clustering in data analysis. This is due to its practical success, simplicity, efficiency, and ease of implementation [142]. The primary objective of k-means is to reduce the sum of squared distances between the centroid of a cluster and the data elements within it [143]. This necessitates the predetermination of the number of clusters, denoted as k.

K-means clustering is based on assigning each datapoint in the dataset X to each cluster k by calculating the minimum distance between the datapoint and the cluster centroid. The objective of the k-means clustering in Equation (3.11). $r_k \in R^p$ serves as the representative of the cluster $k(1 \leq k \leq K)$, and $\{r_1, \ldots, r_k\}$ forms the set of representatives. The functions f and g define distance metrics within R^p.

$$\min_{R} \sum_{y \in Y} f(z^{(i)}, cf(z^{(i)}; R)), \quad (3.11)$$

In Equation (3.11), $f(z^{(i)}, cf(z^{(i)}; R)) = \arg\min_{r\in} f(z^{(i)}, r)$. f quantifies the distance between an object y and its latent feature representation $z^{(i)}$ is the function f assigns the closest feature to the cluster.

3.2.1.2 Novel AE Data Augmentation Strategy Based on CWT

CNNs trained on a very small number of data sets are likely to be overfit [144]. When networks are overfit, their task of classifying other unseen data sets may not be fulfilled and it can generally harm their robustness [145]. To address this problem, data augmentation techniques are used to artificially add replicas of the trained data while preserving the dataset labels [146]. In this work, the strategy used to artificially augment the data is based on adding additive white Gaussian noise (AWGN) as presented in equation (3.12). This AWGN is added systematically. First, the CWT is applied using the Morlet mother wavelet on the AE signals, and wavelet coefficients are extracted. Then, AWGN is randomly added to the extracted coefficients. Since CWT is a linear and reversible transformation, to reconstruct the AE signals from the noisy coefficient, The inverse of the CWT explained in equation (3.13) is used. Figure 3.2 shows the flowchart of the noise addition process and figure 3.3 shows the proposed noise addition process.

$$y(t) = x(t) + n(t), n(t) \sim N(0, \sigma) \quad (3.12)$$

$$ICWT = \frac{1}{C_\zeta} \int_{-\infty}^{\infty} \int_{-\infty}^{\infty} CWT_\zeta(a,b) \frac{1}{\sqrt{a}} \zeta^* \left(\frac{t-b}{a}\right) da\, db \quad (3.13)$$

where $y(t)$ is the noisy signal, $x(t)$ is the signal of interest, $n(t)$ represents the white Gaussian function. The probability density of $n(t)$ is a normal distribution of mean zero and variance σ^2, where σ is the amplitude of the noise.

where $ICWT$ is the inverse of $CWT_\zeta(a,b)$ is the CWT scalogram, ζ^* is the conjugate wavelet function, and C_ζ is a normalization constant.

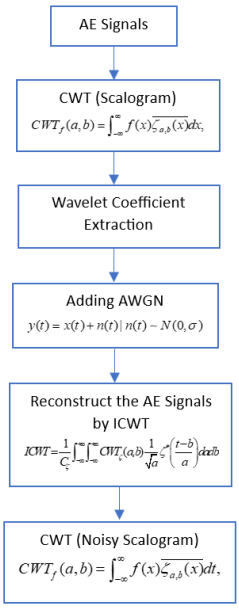

Figure 3.2: Data augmentation strategy based on AE Signals

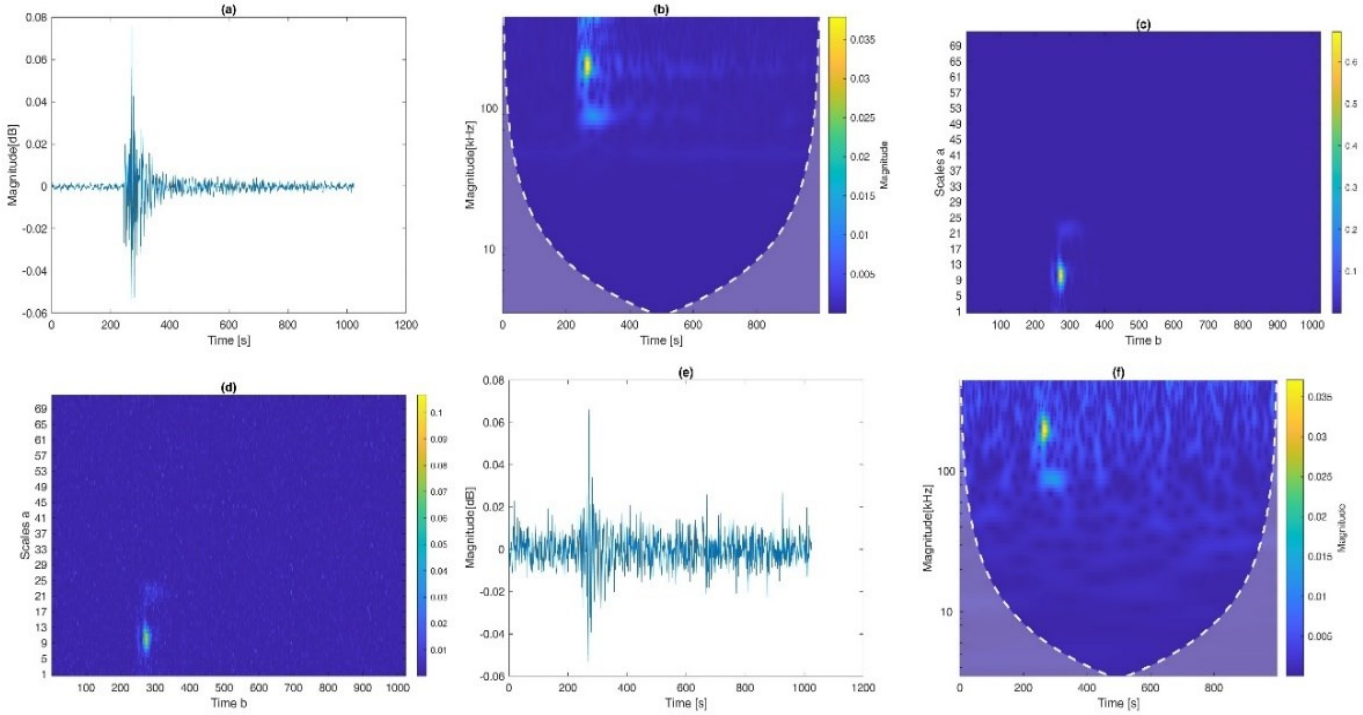

Figure 3.3: (a) Original AE signal, (b) CWT-Scalogram of AE signal, (c) Wavelet coefficient extracted, (d) adding AWGN to the Wavelet coefficient extracted, (e) Reconstruction of original signal from noisy wavelet extracted by Inverse CWT, (f) form the Inverse CWT to CWT-Scalogram

3.2.1.3 Deep Convolutional Neural Networks (CNNs) for Image-Based AE Classification

The CNN is inspired by biological processes, which can automatically learn complex features during training and are much more computationally efficient than traditional neural networks due to the convolution process [37]. They can achieve similar accuracy as human beings in image classification processes due to their self-learning capabilities to solve the multiple classification problem [38]. The main element that constitutes a CNN is a chain of convolutional layers (Conv) with rectified linear unit activation functions (ReLu), (Sigmoid) or other, maximum, or average pooling layers (Max Pool, Avg Pool) and a fully connected layer. Stochastic gradient descent (SGD) and a batch normalization operation are typically used to train the models. Some authors built their models from scratch to solve various classification problems with the CNN [39],[40],[41]. Others based their models on the existing CNN and made some modifications to optimize their results of classification [42], [43]

In this chapiter, an exploration of the possibility to improve the efficiency of AlexNet and SqueezeNet. For a good modification, it is important to understand the main parameters that affect the efficiency of a CNN. Based on this understanding of the parameters and based on the challenges of two previous CNN models, a new model is proposed. AlexNet is one of the most widely used neural network models to date (Figure 3.4). It was first developed as part of the ImageNet Large Scale Visual Recognition Challenge (ILSVRC 2012) [44]. Its structure consists of five convolutional layers (Conv1, Conv2, Conv3, Conv4, Conv5) followed by three maximum pooling layers (Pool1, Pool2, Pool3) and two normalization layers (Norm1, Norm2).

Two fully connected layers are present before the final fully connected layer leading to the output.

SqueezeNet was proposed in 2016 by researchers at DeepScale, the University of California at Berkeley and Stanford University [45]. The ultimate goal was to have a small number of network parameters while maintaining a high level of accuracy. Landola et al. claimed that SqueezeNet has 50x fewer parameters than AlexNet but can achieve about the same accuracy [46,47]. Its structure is based on the fire module, which allows the model to be compressed, as shown in Figure 3.5. The fire module consists of a squeeze convolutional layer with 1×1 filters feeding an expansion layer comprising a mixture of 1x1 and 3x3 convolutional filters. The integral structure is shown in Figure 3.6.

In the same order as Landola et al., a new model is proposed (Figure 3.7 and Table 3.2) that aims to reduce the number of parameters of the network without compromising its efficiency. The main advantage is the reduction of the parameters and the reduction of the development time of a CNN. In order to build this new model, to make a comparison with the previous models, alexNet and squeezeNet and to understand which are the relevant parameters for a good model, several training modes are implemented following the approach proposed in Figure 3.8.

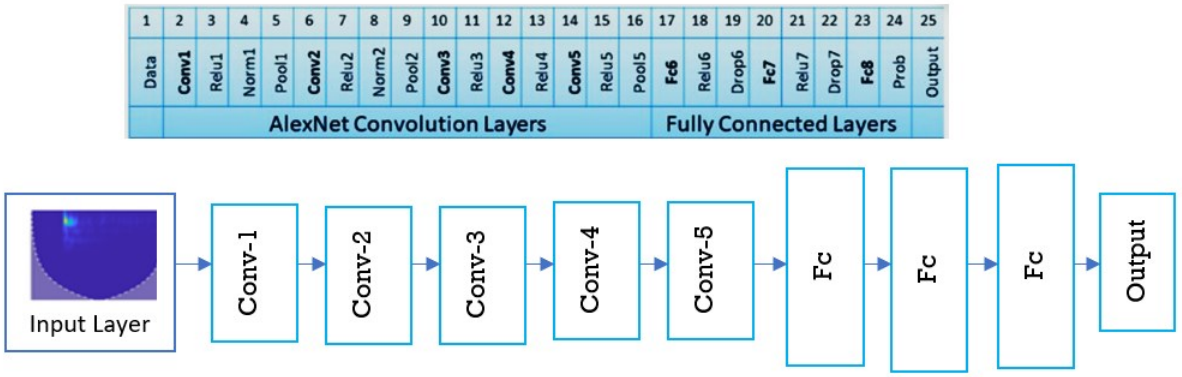

Figure 3.4: AlexNet architecture

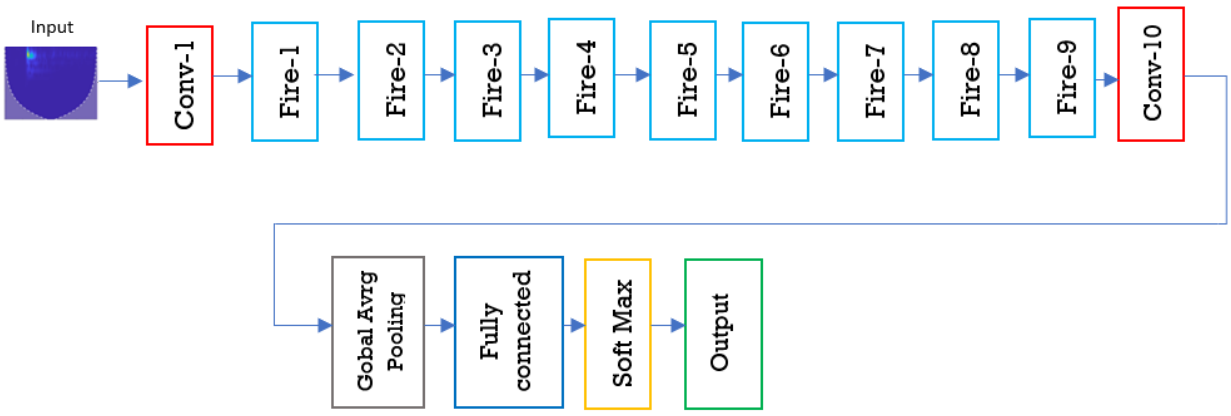

Figure 3.5: SqueezeNet architecture

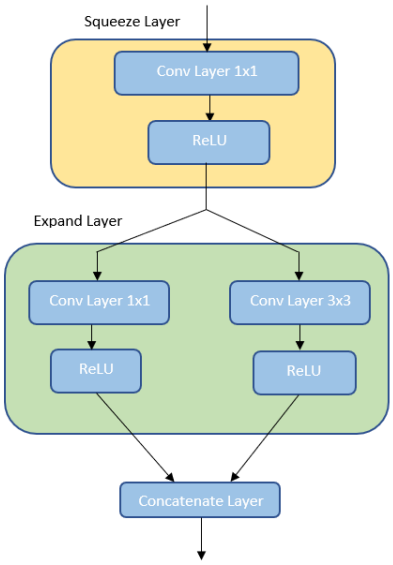

Figure 3.6: Internal structure of the fire module in squeezeNet

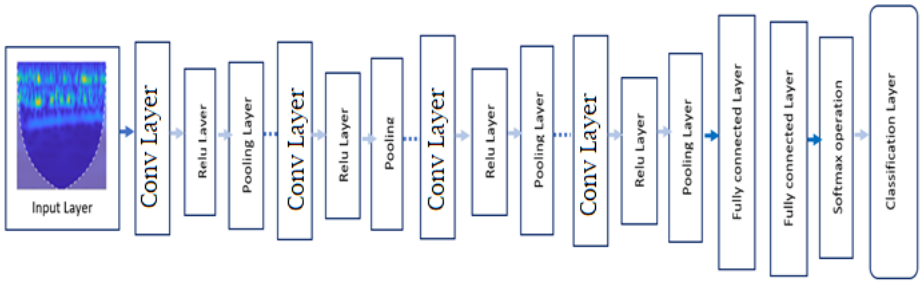

Figure 3.7: New model build

Table 3.2. Configuration of new model

Layer	Description
Input Layer	32 × 32 × 3 Scalogram
Convolution1, Pooling 1	Convolution layer (Filter 3 × 3, 32 Filters) ReLu layer Max-pooling Layer (Filter 2 × 2, strides 2)
Convolution 2, Pooling 2	Convolution layer (Filter 3 × 3, 64 Filter) ReLu layer Max-pooling Layer (Filter 2 × 2, strides 2)
Convolution 3, Pooling 3	Convolution layer (Filter 3 × 3, 128 Filter) ReLu layer Max-pooling Layer (Filter 2 × 2, strides 2)
Convolution 4, Pooling 4	Convolution layer (Filter 3 × 3, 256 Filter) ReLu layer

	Max-pooling Layer (Filter 2 × 2, strides 2)
Fully Connected Layer1	Input Size: 4096 Output Size: 64 ReLu Activation
Fully Connected Layer2	Input Size: 64 Output Size: 4
SoftMax Layer	/
Classification Layer	/

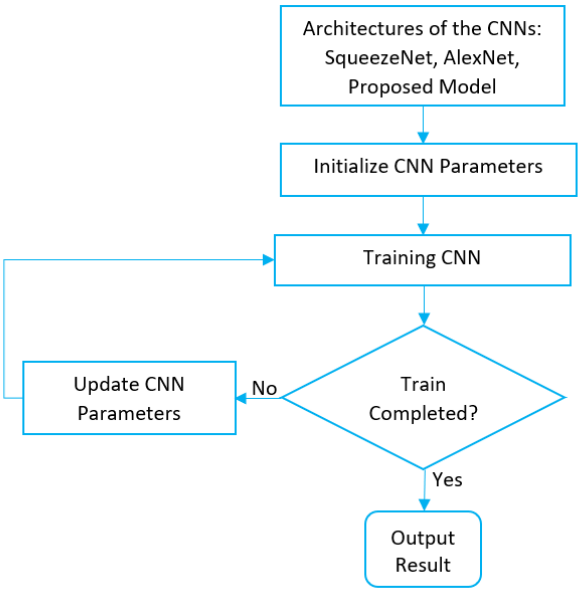

Figure 3.8: Flowchart of training mode

3.2.2 Fuzzy artificial bee colony Convolutional Neural Network (FABC-CNN)

This section provides a detailed description of the proposed CNN model firstly. Secondly, it covers a discussion on fuzzy averaging theory and an artificial bee colony. Finally, it presents an overview of the overall FABC-CNN model.

3.2.2.1 Convolutional Neural Network

CNNs are a category of deep learning algorithms that are modelled following the visual cortex of animals[147]. The interconnectedness of neurons between the eye (input) and the brain (output) allows for decision-making based on visual data. CNNs operate of neurons that extract relevant information from input data accurately. To do this, convolutional layers autonomously extract features from input data using dot product operations and a pre-defined kernel to extract weights and bias [147]. In this work, a CNN model is built from scratch for scalogram classifications of AE signals.

The input to the CNN model is an RGB image of a scalogram that has been resized to 32x32. Several studies have shown that resizing to this dimension yields great results and reduces

training time. The convolution operation is used to extract characteristic features by sliding a convolution kernel over the image. In the case of a scalogram (s) image, the first convolution layer is 3X3X3 the first two numbers represent the size of the filter in the spatial dimensions (height and width), while the third number represents the number of filters, and it uses a rectified linear unit (ReLu) activation function. The choice of a small filter size is intended to capture finer patterns in the image. The output of the convolution layer is formulated as follows:

$$Con^{layer} = r\left(\sum_{l=1}^{z}\sum_{m=1}^{z}\sum_{n=1}^{k} w_{l,m,n,k}\, s_{i+l-1,j+m-1,n} + b_k\right) \quad (3.14)$$

Where, Con^{layer} is the first convolution layer, z size of the filter , k represent the numbers of filter, The indices l, m, n correspond to the dimensions of the convolution kernel, (i, j) represent the spatial coordinates of the output, $r(.)$ is the rectified linear unit activation function that is applied to the weighted sum of the inputs for each neuron in the layer, $w_{l,m,n,k}$ is the weights of the convolution layer for the filter k at position (l, m, n), $s_{i+l-1,j+m-1,n}$ is the value of the input at position $(i + l - 1, j + m - 1, n)$ of the input feature map and represents the bias for the filter k. The output from the first convolutional layer is fed into the second convolutional layer, which employs 32 filters of size 6x6. Using larger filters enables capturing larger and more global features of the image. Employing small filters initially and larger ones later helps to prevent loss of important image information. The pooling layer is implemented to reduce the dimensionality of the output feature maps since their dimensionality and the number of parameters decrease after the pooling layer. This makes the model more prone to overfitting and less tolerant to errors. In this work, the preferred pooling layer is 2x2 maximum pooling. This is because it selects the maximum value of each region of the feature map, which helps to preserve the most important features of the feature map. The maximum pooling process formulated as follows:

$$Pmax^{layer} = \max_{i,j}\left(conv_{i,j}^{layer}\right) \quad (3.15)$$

Where, $Pmax^{layer}$ is the output of the max pooling layer with (i,j) represent the spatial coordinates of the output.

The third convolutional layer with 32 filters of size 3x3 is used which is applied after the first max pooling layer. Afterwards, a fourth convolutional layer by using 64 filters of size 3×3 with the 2x2 maximum pooling layer. The architecture continues by adding a fifth convolutional layer with 128 filters of size 3×3 is used at the output of the second maximum pooling layer. By incorporating this layer, the architecture becomes adept at capturing and effectively representing intricate patterns and complex structures that exist within the input images. This enhancement further strengthens the model's ability to discern and analyze key features. To facilitate dimensionality reduction and abstract feature extraction, the third maximum pooling layer with a window size of 2x2 is introduced. This layer reduces the spatial dimensions of the feature maps while preserving the most important information.

After the last layer of max pooling, there is a flattening layer that transforms the output of the previous layer into a unidirectional vector, enabling the transition from spatial information to characteristic information. Two fully connected layers are employed. The first layer has 512 units with an activation function. A dropout of 0.5 is used to prevent overfitting and improve

model generalization. Finally, the second layer consists of fully connected layers with a number of units corresponding to the number of classes and is correlated with the SoftMax to predict the probability of image appearance in each class. Equation (3,16) presents the simplified form of a fully connected layer (FC), where y represents the FC output (including FC1), and X represents the output of $Pmax_3$. The damage stages are identified in the FC2 layer, which utilizes the SoftMax method for solving multi-classification problems. The calculation is given by expression 8, where Yi represents the result of damage stages, and X_i represents the outputs of the FC2 layer. This expression evaluates the probabilities of all predictive candidates and presents the candidate with the highest probability as the final result.

$$Y = r(\sum X \times w + b) \quad (3.16)$$

$$Y_i = \frac{\exp(X_i)}{\sum_{i=1}^{n} \exp(X_i)} \quad (3.17)$$

The configuration and the step model of the constructed CNN are presented in Table 3.3 and Figure 3.9. As mentioned in the introduction section, optimizing the hyperparameters can significantly improve the accuracy of a CNN. In this context, the weight parameter is chosen for optimization since it plays a crucial role in determining the accuracy of the model. Proper optimization of weights helps to avoid overfitting, which occurs when the model fits the training data too closely and fails to generalize well on new data. With this in mind, the next section will introduce a fuzzy artificial bee colony algorithm.

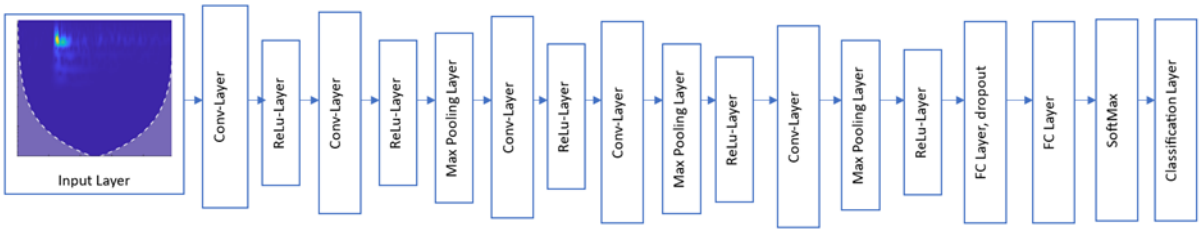

Figure 3.9: Constructed CNN model

Table 3.3. Configuration of the Constructed CNN model

Layer	**Description**
Input Layer	32 x 32 x 3 Scalogram
Conv-Layer	Convolutional Layer (Filter 3x3, 3 Filters) ReLu Layer
Conv-Layer	Convolutional Layer (Filter 6x6, 32 Filters) ReLu Layer Max Pooling Layer (Size 2x2, Strides 2)
Conv-Layer	Convolutional Layer (Filter 3x3, 32 Filters) ReLu Layer
Conv-Layer	Convolutional Layer (Filter 3x3, 64 Filters) ReLu Layer Max Pooling Layer (Size 2x2, Strides 2)
Conv-Layer	Convolutional Layer (Filter 3x3, 3 Filters)

	ReLu Layer Max Pooling Layer (Size 2x2, Strides 2)
FC Layer	Fully Connected Layer, 512 Units
Dropout	Dropout Layer, Probability 0.5
FC Layer	Fully Connected Layer, 4
SoftMax	SoftMax Layer
Classification Layer	-

3.2.2.2 Fuzzy C-means (FCM)

Fuzzy C-means (FCM) is a widely used clustering method that is based on fuzzy set theory and enables data to belong to multiple groups simultaneously [148]. The following steps outline the implementation of this algorithm:

The FCM algorithm can be used to cluster the weights of a CNN. In this context, the data sample w represents the weights of the CNN, which have been divided into C $(2 \leq C \leq n)$ clusters named $(C1, C2, \ldots, Cn)$. The fuzzy membership matrix U is used to represent the degree of membership of each weight in each cluster, where v_i represents the cluster center of each cluster and uik represents the degree of membership of the weight w_i in cluster C_i. The objective function J_b is used to measure the degree of overlap between the clusters and is defined as a sum of the squared distances between each weight and its assigned cluster center, weighted by the degree of membership of the weight in the cluster.

$$J_b(U, v) = \sum_{i=1}^{C} \sum_{k}^{n} u_{ik}^{b} ||w_k - v_i||^2 \quad (3.18)$$

Suppose we have a set of measured data represented by $w_{k,}$ and cluster centres represented by v_i. The distance between w_k and v_i is calculated using the standard Euclidean distance represented by $||.||$. The degree of fuzzification is denoted by b where $b = 2$ is considered optimal for most applications. We optimize the objective function J_b by updating the membership degree u_{ik} and cluster centre v_i. The expression for the membership degree u_{ik} is determined accordingly.

$$u_{ik} = \left[\sum_{j=1}^{C} \left(\frac{||w_k - v_i||^2}{||w_k - v_j||} \right)^{1/b-1} \right]^{-1} \quad (3.19)$$

With u_{ik} has the constraint that $\sum_{i=1}^{C} u_{ik} = 1, \forall k$. The clustering centre $\{v_i\}$ is expressed as,

$$v_i = \frac{\sum_{k=1}^{n} u_{ik}^{b} w_k}{\sum_{k=1}^{n} u_{ik}^{b}} \quad (3.20)$$

The clustering process involves iterative application of equations (3.19) and (3.20) to classify the data until the algorithm terminates. Upon completion of the fuzzy clustering partition, all clustering centers may be established.

3.2.2.3 Artificial Bee Colony (ABC)

The artificial bee colony ABC algorithm was introduced by Karaboga in 2005 as one of the population-based metaheuristic algorithms [149], [150]. The ABC algorithm is based on the natural foraging behavior of bees. The main objective of the algorithm is to ensure that each food source corresponds to a unique solution to the problem, with the largest food source giving the best result. The components of the ABC, which are inspired by the foraging behavior of bees, are as follows:

- Food source: This component represents a potential optimization solution.
- Fitness value: This value represents a food source excellence. It is depicted as a singular quantity associated with the objective function of a feasible solution for the sake of simplification.
- Bee agents: A group of computational agents constitute this component The honey bees in the ABC are classified into three categories: employed bees, onlooker bees and scout bees Figure 3.10.

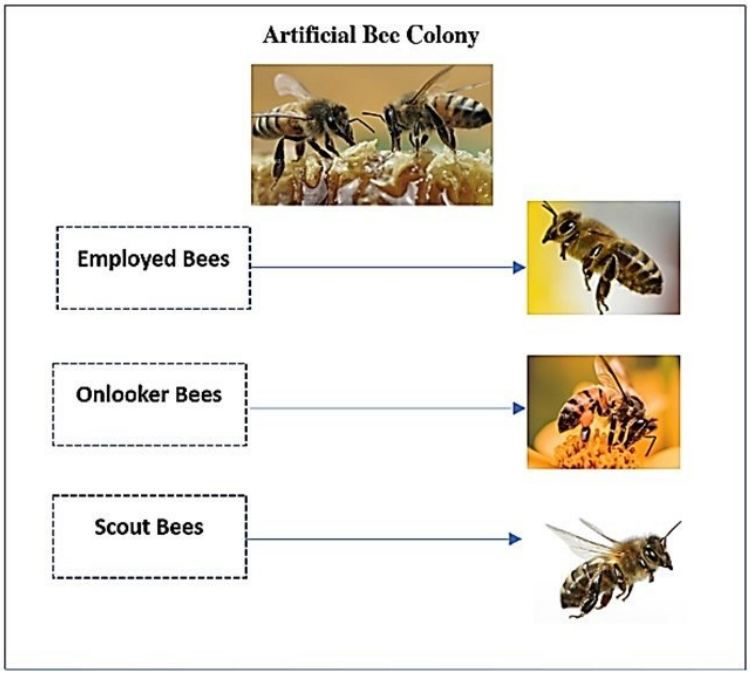

Figure 3.10: Three categories of artificial bees in ABC

Figure 3.11 shows the algorithmic phases of the ABC optimization procedure. This algorithm can be mathematically described as follows:

First, the algorithm initializes a set of potential solutions represented by the number of clusters (c_n) generated by the Fuzzy C-means algorithm. Each cluster represents a potential solution for the CNN weights that the algorithm will explore to find the best weight configuration. To generate these solutions, the algorithm randomly selects a position in the search space for each cluster. The search space is defined by the minimum (w_{min}) and maximum (w_{max}) values for each dimension of the problem. The dimensionality of the search space for the weights is determined by D, as shown in equations (3.21) and (3.22). D represents the total number of weights in the neural network that need to be optimized.

$$i \in \{1, 2, \dots, c_n\}, j \in \{1, \dots., D\} \quad (3.21)$$

$$w_j^i = w_{\min j} + rand[0.1]\left(w_{\max j} - w_{\min j}\right) \quad (3.22)$$

After generating the set of potential solutions represented by the number of clusters (c_n), the Artificial Bee Colony algorithm evaluates the fitness value of each solution by computing the objective function (f) that corresponds to the CNN weight configuration represented by that cluster. This value is calculated according to equations (3.23) and (3.24).

$$fit\left(w^i\right) = \begin{cases} \frac{1}{f(w^i)+1}, \\ 1 + \left|f(w^i)\right| \end{cases} \quad (3.23)$$

$$f\left(w^i\right) \geq 0, f(w^i) \prec 0 \quad (3.24)$$

In the employed bee step of the Artificial Bee Colony algorithm for optimizing the weights of the CNN, each employed bee produces a new weight configuration in the vicinity of an existing food source, according to equation (3.25). The position of the new food source, N^i, is generated by modifying the position of the existing food source, w^i, in a randomly chosen dimension, $j \in \{1, 2, \dots, D\}$. The modification is performed by adding a random perturbation, φ_{ij} (which is a real number uniformly distributed in the interval [-1, 1]), to the difference between the position of the existing food source and the position of a randomly selected food source, w^k (where $k \neq i$). The employed bees explore the search space for weight configurations by generating new solutions, and they use the fitness values of the solutions to determine which ones should be explored further in the search process.

$$N_j^i = w_j^i + \Phi_{ij}\left(w_j^i - w_j^k\right) \quad (3.25)$$

The algorithm iteratively optimizes the weight configuration of the CNN. During the onlooker bee step, if an onlooker bee visits a promising food source with a high amount of nectar (i.e., optimal fitness value), this information is shared among the workers using the fitness value equation (3.24). The shared information is used to calculate a potential attractiveness in the form of a selection probability pi, which is used to determine the next food source to explore. The selection probability is calculated using equation (3.26), where $fit(w^i)$ represents the fitness of the i^{th} solution and fit_{max} represents the maximum fitness value for the whole population.

$$pi = \frac{fit(w^i)}{\sum_{k=1}^{C_n} fit(w^k)} \quad (3.26)$$

During an onlooker bee or employed bee iteration, a new solution Ni is generated from an existing solution w^i, using equation (3.25). If the new solution Ni does not improve the fitness of the existing solution w^i, a visit counter is incremented for w^i. When this counter reaches a limit value, the solution w^i is abandoned and replaced by a new solution generated using equation (3.23). These two phases continue until a satisfactory fitness value is achieved, or the maximum number of iterations is reached.

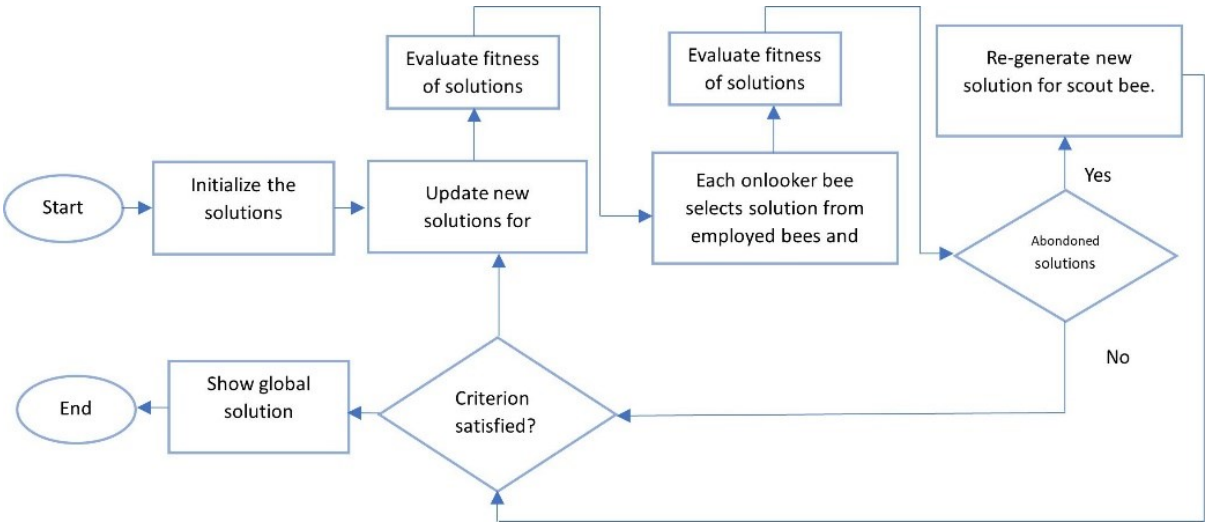

Figure 3.11: Flowchart of artificial bee colony (ABC)

3.2.2.4 Overview of FABC-CNN

The preceding subsections have established a theory regarding the design of the CNN, FCM, and ABC models. In this subsection, the overall model is outlined. The performance of a CNN classification may depend on the weights and gradient descent algorithm, both of which are susceptible to local optimum solutions. This paper proposes a framework based primarily on the ABC optimization algorithm to address this issue. The ultimate objective of ABC is to determine the optimal weights from the various weight sets. The CNN model is initially used to train scalograms. The fully connected layer generates a vector representation of each scalograms characteristics. The extraction of the weights associated with each neuron in the fully connected layer was made. The FCM is applied to the weights extracted. The FCM is especially useful when data is difficult to separate and features may belong to multiple clusters, as in the case of weights. In order to identify the optimal number of clusters for clustering similar weights, an initial fuzzy model can be created to represent the weight of each class. Subsequently, a clustering algorithm can be applied to the model to group similar weights into their corresponding clusters.

The clusters the weights obtained by FCM are considered as potential solutions for the employed bees. The employed bees inform the onlookers of any new solutions they have discovered. The scout bees then choose the optimal solutions, update them, and recalculate the fitness of their solutions. Repeat the procedure until the number of iterations equals the threshold value. The scout bees will generate new solutions to replace those that are unable to improve fitness within a specified time frame. The back projection based CNNs are trained using gradient descent to update the optimal weight that satisfies the ABC algorithm. This reduces the overall classification error. Figure 3.12 is a flowchart of the proposed methodology.

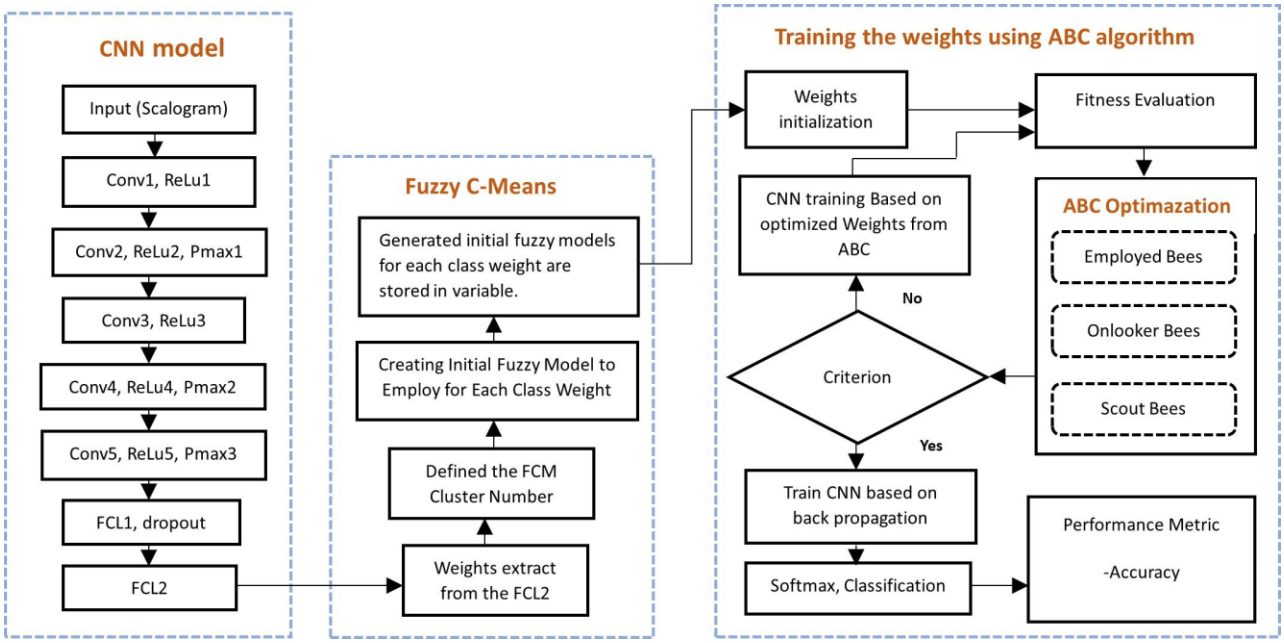

Figure 3.12: The Proposed Novel Fuzzy Artificial Bee Colony CNN-Inspired

3.2.3 Novel Deep Autoencoder Framework based AE Analysis

3.2.3.1 Overall framework

The novel method proposed in this work for damage mode classification is illustrated in Figure 3.13 Firstly, the AE signals collected from the tensile tests of the JLS specimens are used to train a deep autoencoder (DAE) model. The training process is structured into two main stages: encoding and decoding. During the encoding process, the AE signals are processed to condense to reduce their dimensions and to extract the essential features that reflect the state or changes in the signal data. This step transforms the raw data into a more compact format called latent features. Decoding, meanwhile, involves interpreting and reconstructing a representation of the original data from the condensed features obtained during encoding. In this work, the latent features obtained during encoding are extracted using Singular Value Decomposition. These latent features are then analyzed using the k-means algorithm and each cluster is assigned to different damage modes in the tested composite specimens. The procedure is further expanded for data validation using time-frequency analysis. The AE data reconstructed by the decoder is analysed using Hilbert Spectrum Analysis. The architecture and hyperparameters of the DAE model are optimized for reconstruction errors and k-means loss. The details of the proposed algorithms are presented in the following sections.

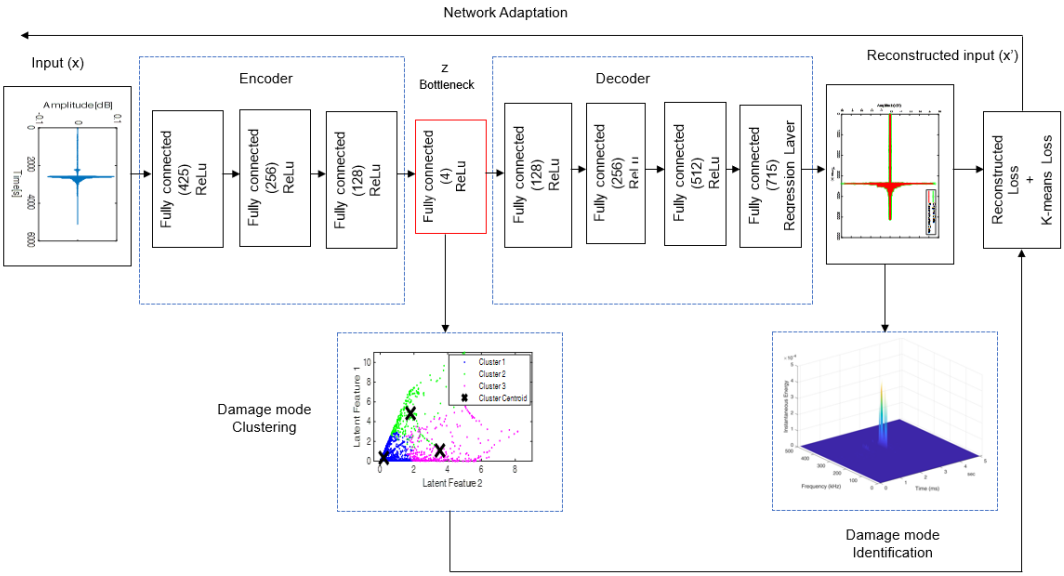

Figure 3.13: An Overview of the Damage Mode Characterization Framework Based on Deep Autoencoder, k-means Clustering and Hilbert Spectrum Analysis

3.2.3.2 Deep Autoencoder (DAE)

The architecture is composed of an encoder and a decoder block. The autoencoder is a specialized form of artificial neural network used to learn efficient features of an unlabelled data, enabling it to estimate input variables (reconstruction) [27]. This is achieved by capturing the inherent relationships and statistical patterns between the input variables in the data [28]. A schematic representation of the DAE is presented in Figure 3.13. The graphs in the lower part of Figure 3.14 highly illustrate the transformation process of complex input data by a deep autoencoder. Initially, the encoder reduces the dimensionality of this data, effectively transforms it from a high-dimensional space to a more compact, lower-dimensional representation in the latent space [30]. This is achieved by extracting the most significant attributes inherent to the data. Subsequently, the data are reconstructed into a simplified output by the decoder through the learned low dimensional information in the feature space [31]. For the autoencoder, different types of neural network architectures can be used, depending on the specific data type. For instance, the Convolutional Neural Networks (CNNs) are suitable at extracting features from spatial data, such as images. The Long Short-Term Memory networks (LSTMs) are used for sequential data such as time-series forecasting or speech recognition because of their ability to store long-term dependencies The Dense networks, known for their simplicity, are versatile in general pattern recognition, as they are able to encode data in a compact form and reconstruct it. The architecture chosen for this study is based on fully connected (dense) neural networks, which demonstrate an exceptional ability to encode data in a reduced-dimensional space and reconstruct it with high fidelity.

The overview of the training parameters of the deep autoencoder model deployed in this study is presented in Table 3.4. In the proposed deep autoencoder model, the architecture is structured into eight layers, segmented into four pivotal stages: input, encoding, bottleneck, and decoding, culminating in the regression output. The design begins with an input layer accommodating data of dimensions 5120x715, setting the foundation for subsequent processing. The

architecture then goes through a compression sequence, where the number of neurons is reduced from 425 to 256, then to 128, each layer being followed by a ReLu activation to inject non-linearity, which improves the network's ability to extract important features. At the core, the bottleneck layer, consisting of only 4 neurons and a ReLu activation, captures the essence of the data. This is succeeded by an expansion phase, where neuron counts increase from 128 to 425 across three layers, each augmented with a ReLu activation, aiming to reconstruct the data around the bottleneck's condensed features. The final layer, with 715 neurons, transitions to a regression output, readying the network to generate refined predictions. This output matches the input's dimensions, demonstrating the network's capability to process, compress, and expand data for Complex regression tasks.

The encoding process effectively transforms the input, denoted as $z^{(l-1)}$, into a compact hidden representation $z^{(l)}$, and this process can be expressed as follows:

$$z^{(l)} = \alpha_1(b + Wz^{(l-1)}), \quad (3.27)$$

In Equation (3.27), α_1 is the activation function of the rectified linear unit (ReLu) that represents the nonlinear mapping between the input $z^{(l-1)}$ and the output $z^{(l)}$, from the input layer to the fourth layer, with w as the weight matrix and b as the bias vector, respectively. The dimensionality of inputs decreases in proportion to the number of neurons in the bottleneck hidden layer, where the dominant features that represent information content in the input data are automatically extracted [32]. Subsequently, the decoder utilizes the bottleneck hidden layer to reconstruct the initial input through mapping by the activation function Relu α_2.

$$\hat{x}^{(l)} = \alpha_2(\hat{b} + \hat{W}\hat{z}^{(l-1)}), \quad (3.28)$$

where $\hat{x}^{(l)}$, and $\hat{z}^{(l-1)}$ are the output and input from the fourth layer to the eighth layer in the decoder network, and its parameters include the weight matrix $\hat{w}$ and offset vector $\hat{b}$. Consider a scenario in which we have raw data $X \in \mathbb{R}^{N \times n}$, where each row x_i represents an individual sample within a collection of samples. In the training process, the root mean squared error (RMSE) metric is used for a given collection x_i containing n data points. The primary objective of the loss function is to minimize the discrepancy between the reconstructed output $\hat{x}_i$ and the original input x_i .

$$L_{RMSE} = \sqrt{\frac{1}{N}\sum_{i=1}^{N} \| x_i - \hat{x}_i \|_2^2}, \quad (3.29)$$

With $\hat{x}_i$ is the i-th reconstructed sample.

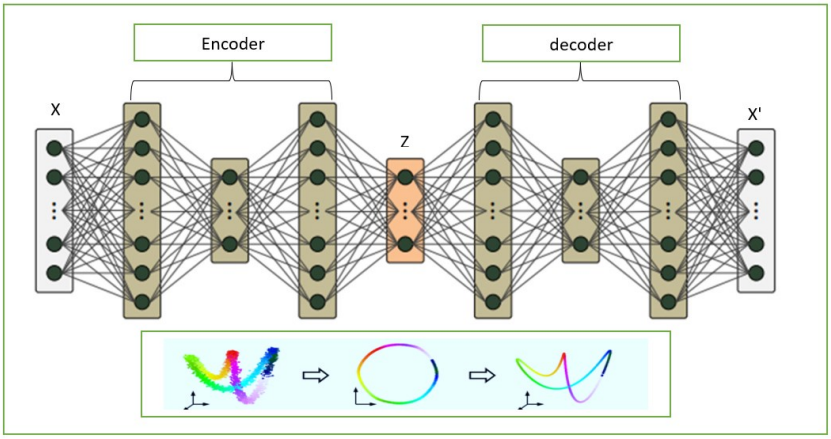

Figure 3.14: Schematic of Deep autoencoder model architecture.

Table 3.4. Deep autoencoder model configuration

Layers	**Descriptions**
Input Layer	5120 x 715
Fully Connected Layer 1	425 units ReLu layer
Fully Connected Layer 2	256 units ReLu layer
Fully Connected Layer 3	128 units ReLu layer
Fully Connected Layer 4	4 units ReLu layer (Latent Features)
Fully Connected Layer 5	128 units ReLu layer (Reshape)
Fully Connected Layer 6	256 units ReLu layer
Fully Connected Layer 7	425 units ReLu layer
Fully Connected Layer 8	715 units Regression Layer
Output	5120 x 715

The latent feature from the bottleneck layer is used for classifying the damage modes. This process is explained in detail in the subsequent sections.

3.2.3.3 Latent feature clustering using k-means

In this research, k-means clustering is used to group latent features of the AE signals generated by the composites tested. As mentioned earlier, these latent features are taken from the bottleneck layer of the DAE. The main objective is to assign the latent features to the different damage modes in the tested JLS specimens. K-means clustering is based on assigning each

datapoint in the dataset X to each cluster k by calculating the minimum distance between the datapoint and the cluster centroid. The objective of the k-means clustering in Equation (3.30). $r_k \in R^p$ serves as the representative of the cluster $k(1 \le k \le K)$, and $\{r_1,\ldots,r_k\}$ forms the set of representatives. The functions f and g define distance metrics within R^p.

$$\min_R \sum_{y \in Y} f(z^{(i)}, cf(z^{(i)}; R)) \quad , \quad (3.30)$$

In Equation (3.30), $f(z^{(i)}, cf(z^{(i)}; R)) = \arg\min_{r \in} f(z^{(i)}, r)$. f quantifies the distance between an object y and its latent feature representation $z^{(i)}$ is the function f assigns the closest feature to the cluster. To update the autoencoder for k-means compatibility, meaning to ensure that data points are evenly distributed around cluster centers, Yan et al. [143] proposed the following cost function:

$$L(z, \mu) = \sum_{i=1}^{M} \sum_{k=1}^{K} s_{ik} \, || \, z^{(i)} - \mu_k \, ||^2 \quad , (3.31)$$

Where $L(z, \mu)$ is the total clustering loss for the latent features, M is the number of data points, $z^{(i)}$ represents a set of latent features, μ_k is a cluster center and s_{ik} is a Boolean variable that assigns $z^{(i)}$ with μ_k. . Minimizing this loss with respect to the network parameters ensures that the distance between each data point and its assigned cluster center is small, improving the clustering quality when applying k-means.

3.3 Conclusion

This chapter introduces various methods for analyzing Acoustic Emission (AE) signals, including non-learning and learning approaches. Time-domain, frequency-domain, and time-frequency techniques, such as the Continuous Wavelet Transform (CWT), are covered for traditional analysis. On the machine learning side, clustering methods such as K-Means and a novel data augmentation strategy using CWT with Gaussian noise are explored. Advanced models like the Fuzzy Artificial Bee Colony Convolutional Neural Network (FABC-CNN) and a Deep Autoencoder framework are employed for AE signal classification and raw waveform analysis. These methods will be applied to case studies on AlSi10Mg specimens obtained by AM-SLM and CFRP composites in Chapters 4, 5, and 6.

Chapter 4. AM-SLM AlSi10Mg Specimens for Aerospace Applications: Materials, Testing Methods, and Mechanical Characterization

This chapter presents the common elements related to the materials, testing methods, and characterization of the mechanical behavior of AlSi10Mg specimens produced via Selective Laser Melting (SLM). The specimens were built in different orientations (X, Y, Z, and 45 degrees), and tensile tests were performed while recording AE signals. The specific methods of AE signal analysis will be detailed in Chapters 4 and 5.

4.1 Introduction and scope

Additive manufacturing (AM) is a rapidly growing process with advantages over traditional processes [151]. It provides significantly reduced design constraints, structural optimization, flexibility, and material saving characteristics with a wide range of applications in aerospace, automotive, and biomedical industries [152]. The growing use and diversity of parts produced during (AM) enhance the need for in-depth study of their mechanical properties [52]. The most widely used methods for AM of metallic materials are powder-fed systems such as electron beam melting (EBM), selective laser sintering (SLS), and selective laser melting (SLM). Among the popular methods mentioned above, SLM is the most popular method for AM of metal powders for flexibility in the production of all castable materials, high quality of parts produced in a short time, and high resolution for complex shaped parts. The aerospace, automotive, and marine industries focus on powder bed SLM technology for Ti-alloy, Ni-superalloy [153], Ni-based alloys [154], stainless steel [155], and Al-based alloys [156] components. AlSi10Mg was used in additive manufacturing for its good mechanical properties such as an excellent compromise between lightness, strength, limited restriction and high resolution for complex shapes and structures and a short printing time. Given the almost eutectic composition of Al and Si, a great weldability can be achieved. Mg plays an important role in age hardening in the form of β' and Mg_2Si (β phase) [157]. Recently, many works have been published on the microstructure using a study of processing parameters of AlSi10Mg fabricated by SLM [158]. During the fabrication of mechanical parts in the SLM process, the orientation of the construction has direct effects on the anisotropy and microstructural heterogeneity of SLM components, especially in AlSi10Mg. In most cases, the crack path in AlSi10Mg is strongly influenced by microstructural heterogeneity [159]. Obtaining an equiaxed grain remains a challenge since the cooling rate is high in the range of 106°C - 108°C. Several investigations demonstrated that orientation of construction remains a major challenge, mostly for AlSi10Mg built in SLM, whose cracking trajectories in most cases are related to microstructural heterogeneity. Therefore, it is important to understand the intrinsic behaviour of this component built on different orientations [160].

Many authors propose methods for monitoring the mechanical characteristics of specimens based on the acoustic emission (AE) technique [161]. This is a passive non-destructive evaluation (NDE) technique, used to detect and study specimen damage at the microscopic scale. The acoustic waves generated contain information about the initiation and progression

of damage. These acoustic waves can be recorded using a piezoelectric sensor. The recorded waveform can be analyzed in terms of its time-frequency properties to obtain information on the onset of damage and its evolution. The study of these AE waveforms can help to understand the characteristics of the damage [10]. Currently, there are few research papers regarding the damage characterization of AlSi10 Mg specimen obtained by the SLM process using the AE technique [162]. However, the AE technique has been successfully used for damage characterization of other specimen obtained by other additive manufacturing processes.
For example, Ould et al. studied the characterization of fatigue damage in 304L steel by AE technique for different total strain amplitudes. Through the parameter-based approach, a correlation between the acoustic signals and the damage evolution during the fatigue tests were obtained [163]. Barile et al. monitored the delamination process of 3D parts obtained during the Fused deposition modelling (FDM) process. They also have used parameter-based analysis of the acoustic emissions provided relevant predictive information about the material under test [164]. Barile et al. studied the crack propagation process in grade 5 titanium samples subjected to uniaxial fatigue loading using AE and IR thermography [165]. The AE techniques were found to be more accurate, as they were able to monitor crack activity and distinguish crack initiation in the beginning stages of the test [165]. Nonetheless, signal-based approaches are more efficient in comparison to parameter-based approaches, especially when the target to assign the acoustic emission signals to their damage sources.

This chapter describes the materials used, the manufacturing process, and the testing methods employed, which include tensile testing and the acquisition of Acoustic Emission signals during the tests. Additionally, it presents some mechanical results obtained from the specimens produced via Selective Laser Melting in different orientations (Tx, Ty, Tz, and T45). The analysis focuses on the behavior of the materials under load.

4.1 Materials and Testing Method

4.1.1.1 Materials

The AlSi10Mg specimens used in this work were produced using the AM-SLM process. The specimens are divided into four types based on the building direction along X, Y, Z, and at 45° inclination with respect to the bed. The AlSi10Mg powder melts at temperatures ranging from 570 to 590 °C and has a density of 2.68 g/cm^3. Its chemical composition is shown in Table 1.

Table 4.1. Chemical composition of AlSi10Mg specimens

Element	AI	Si	Mg	Fe	N	O	Ti	Zn	Mn	Ni	Cu	Ph	Sn
Mass (%)	Bal[a]	11	0.45	<0.25	<0.2	<0.2	<0.15	<0.1	<0.1	<0.05	<0.05	<0.02	<0.02

[a]Balance percentage

Figure 1 shows the dimensions of all specimens constructed in accordance with ASTM E8M. The AlSi10Mg powder underwent melting through the RenAM 500 series additive manufacturing machine, which utilized an Nd: YAG laser source with 400 Watts of output power and a 1.064 μm wavelength configuration. This wavelength was crucial to achieving

efficient powder melting and shaping. The powder was scanned by the laser beam at a rate of 100 mm/s, with a melting point diameter of 200 µm , resulting in an energy density of 20 J/mm2 in a single pass. Each layer during the SLM process was uniformly 20 µm thick, with the coated powder layer being moved along the y-axis while the laser scanned the component along the x-axis, ensuring precise and consistent fabrication. The SLM components were manufactured in four distinct orientations relative to the build platform, as shown in Figure. 2, without affecting the laser scan axis stability throughout the process. After scanning, the components were air-cooled and subjected to approximately two hours of relaxation at 300°C ± 10°C.

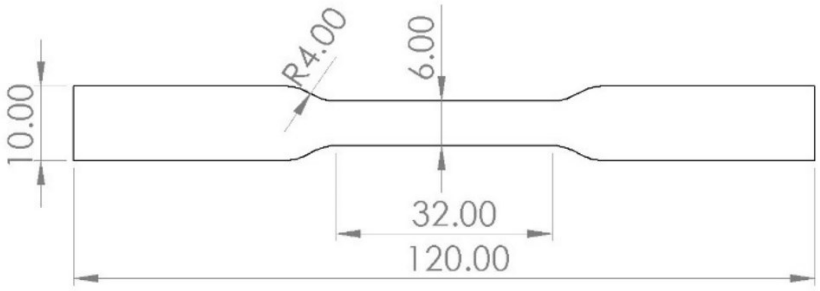

Figure 4.1: Specimen dimensions according to ASTM E8M (Dimensions are in mm)

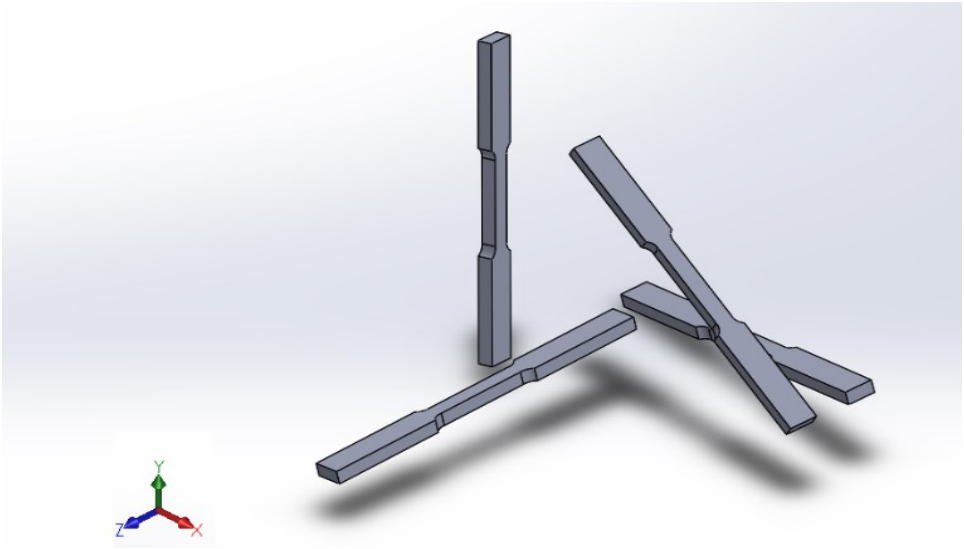

Figure 4.2: Orientation of specimen built along X, Y, Z, and a 45°

4.2 Testing Methods

Uniaxial strain gauges are used to measure strain evolution during the tensile tests. Before the strain gauge was properly connected, the surface of the specimen was cleaned with an acid solution followed by neutralization with a base. The tensile test was carried out in an INSTRON 1342 servo-hydraulic loading machine with a load capacity of a 10 kN and a crosshead travel speed was set at 1 mm/min. For the detection of the acoustic signal the Pico sensor (Physical Acoustic) broadband probe was used. Distinctive characteristics of the sensor are presented in Table 4.2. The Pico sensor was properly connected to the specimen surface

using two couplers. starting with the application of a silicone gel that established a flawless connection between the sensor and the specimen surface in order to ensure accurate signal capture and eliminate any interference from the reverberation frequency of the sensor's oscillating crystal and a 0.03-mm-thick Kapton tape was applied over the silicone gel layer. This method prevents the interference of strain gauge and load cell during AE signal acquisition. The signals were pre-amplified to 40 dB before being acquired at 2 MSPS sampling rate and passing through a 1 kHz low-pass and 3 MHz high-pass filter.

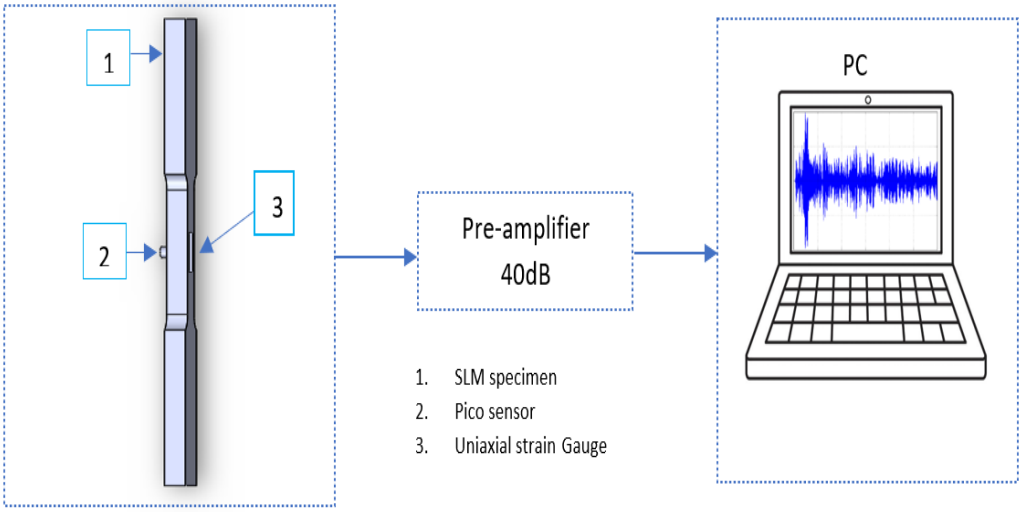

Figure 4-3: Schematic of acoustic emission setup

Table 4.2. Pico Sensor operating specifications

Pico Sensor Specifications	
Peak Sensitivity	54 dB
Operating Frequency Range	250 – 750 kHz
Resonant Frequency	250 kHz
Dimensions	3.94 mm x Ø 4.78 mm
Temperature Range	-65 to 177ºC
Directionality	+/- 1.5 dB

4.3 Mechanical Characterization of AM-SLM AlSi10Mg Specimens

The mechanical properties, ultimate tensile strength, yield strength, Young's modulus, and elongation at break of the specimens is presented in Table 4.3. The average, and standard deviation (Std_dev) are used to compare the mechanical properties.

Table 4.3. Tensile test results of all the specimens.

Orientation	Metrics	Yield strength MPa	Ultimate tensile strength MPa	Young's modulus E GPa	Elongation at break %
Tx	Mean	135.1	212.8	66.3	12.2
	Std_dev	2.4	3.9	3.5	1.1
Ty	Mean	138.8	215.4	68.4	12.7
	Std_dev	2.7	2.2	3	4.6
Tz	Mean	123.4	208.7	63.5	7.6
	Std_dev	2.3	3.4	2.7	0.5
T45°	Mean	125.2	212.8	64.3	9.6
	Std_dev	2.4	2.5	1.3	1.4

The results presented in Table 4.3 for the four groups of specimens. Certain observations were made especially for the group of specimens Tx and Ty. First, they exhibited similar mechanical properties. In addition, they exhibited high yield strength compared to Tz and T45. Finally, the group of specimens Tz shows weak mechanical properties compared to Tx, Ty, and T45. Several authors have shown that the orientation of SLM components affects their anisotropy, microstructural heterogeneity, and mechanical properties [166]. Figure 4.4 shows the representative load-displacement curves for four different groups of specimens (Tx, Ty, Tz, and T 45°). Figure 4.5 shows two deformation stages considered in accordance with ASTM E8. The elastic limit is defined from the stress-strain data. The first is elastic deformation, where the deformation is linear and reversible, and the stresses are less than or equal to the elastic limit. This phase considers the consolidation zone and the constriction zone, so that the strain of the specimen before and after failure is considered. The average value of the proportion between the elastic limit and the ultimate limit for all specimens is 130 MPa to 184 MPa. The specimens in the Tx and Ty group are quite similar, unlike the Tz and T45 group. Acoustic emission signals are measured during both elastic and plastic phases. A time-frequency analysis is performed, and several CNN models are built to classify the signals of the different damage stages.

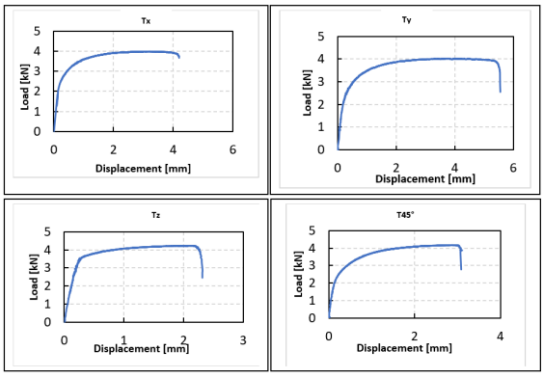

Figure 4.4: Load-displacement curves different group of AlSi10Mg specimens (Tx, Ty, Tz, and T45)

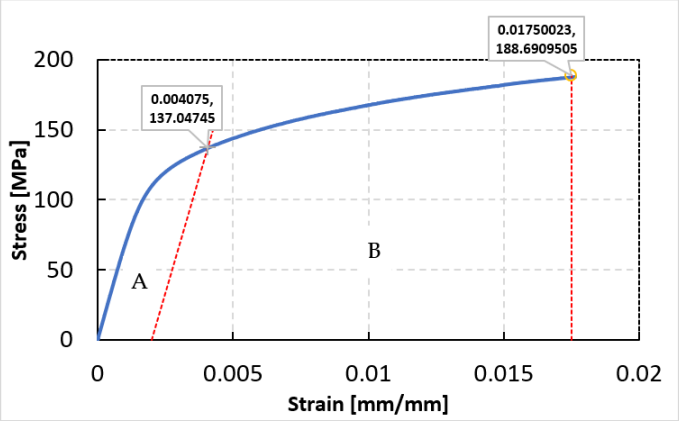

Figure 4.5: (A) Elastic stage, (B) Plastic stage considered for the AE analysis

4.4 Conclusion

In conclusion, this chapter highlights the mechanical behavior of AlSi10Mg specimens produced via SLM in different orientations (X, Y, Z, and 45 degrees). Tensile tests and AE signal analysis were used to characterize the elastic and plastic deformation stages. The Tx and Ty specimens showed similar mechanical properties and higher yield strength compared to Tz and T45, with Tz exhibiting the weakest performance. These results confirm that build orientation affects the anisotropy and mechanical properties of SLM specimens. Different methods of AE analysis will be applied in the following chapters to classify the damage stages across the specimens using Acoustic waveform and deep learning approach.

Chapter 5. Classification of Mechanical Behavior of AM-SLM AlSi10Mg Specimens for Aerospace Applications Using AE and Deep Learning

This chapter focuses on the application of deep learning techniques for analyzing Acoustic Emission (AE) signals, building on the materials, testing methods, and mechanical behavior results discussed in Chapter 4.

The chapter explores the integration of Acoustic Emission technique with deep learning (DL) framework to classify the mechanical behavior of AlSi10Mg specimens produced via Selective Laser Melting (SLM). Specimens, built in different orientations (X, Y, Z, and 45 degrees). Tensile test with AE signals was recorded to monitor damage mechanisms. Continuous Wavelet Transform (CWT) was used to distinguish between elastic and plastic deformation stages.

Three Convolutional Neural Network (CNN) models AlexNet, SqueezeNet, and a simplified new model were trained to classify AE signals. The simplified CNN model outperformed the others, offering greater accuracy and efficiency for damage classification, making it a valuable tool for SHM in aerospace.

5.1 Introduction and scope

AlSi10Mg is widely used in additive manufacturing, specifically through the Selective Laser Melting process, due to its excellent mechanical properties and suitability for producing complex aerospace components. The orientation of the build during the SLM process can significantly impact the mechanical properties and microstructural characteristics of the material. Understanding the mechanical behavior of AlSi10Mg in different orientations is crucial for optimizing its application in critical industries like aerospace.

Many authors have employed the Acoustic Emission technique to monitor the mechanical characteristics of materials. AE is a passive, non-destructive evaluation (NDE) method that detects acoustic waves generated by microscopic damage processes within materials. These waves carry information about the initiation and progression of damage and are captured using piezoelectric sensors. The analysis of the AE signal waveform, particularly in the time-frequency domain, can provide valuable insights into the onset and evolution of material damage [161]. Although limited research has focused on using AE to study AlSi10Mg produced via SLM [167], [168], AE has been successfully used for damage characterization in other AM materials.

Recently, researchers have developed approaches based on the artificial intelligence [165], [169], particularly the combination of the signal-based AE technique and artificial intelligence for damage characterization. Some authors have implemented the artificial neural network (ANN) by using statistical descriptors for intelligent damage monitoring [170]. However, Xu

et al. and D'Addona et al. stating that ANN is not suitable to capture the content of information associated with AE signals [171], [172].

Currently, researchers are focusing on developing the deep learning approach using combined AE signals. The CWT are applied to AE signals, the scalogram are extracted containing the time-frequency. These scalograms are used as an image to be transmitted to a Convolution neural network (CNN) for possible classification.

The CNN is inspired by biological processes, which can automatically learn complex features during training and are much more computationally efficient than traditional neural networks due to the convolution process [173]. They can achieve similar accuracy as human beings in image classification processes due to their self-learning capabilities to solve the multiple classification problem [174]. AlexNet is one of the most widely used neural network models to date (Figure 4). It was first developed as part of the ImageNet Large Scale Visual Recognition Challenge (ILSVRC 2012) [174]. Its structure consists of five convolutional layers (Conv1, Conv2, Conv3, Conv4, Conv5) followed by three maximum pooling layers (Pool1, Pool2, Pool3) and two normalization layers (Norm1, Norm2). Two fully connected layers (Fc) are present before the final fully connected layer (Fc) leading to the output. SqueezeNet was proposed in 2016 by researchers at DeepScale, the University of California at Berkeley and Stanford University [175]. These networks are suitable for processing both large-scale and small-scale image inputs.

The CNN and acoustic emission signals are used to characterize the damage mode of composite materials and structures. Zhang et al. worked on classification of damage-induced acoustic emission signals in UHPC using convolutional neural networks [176]. Several CNN are used: googleNet, ResNet18, efficientNet and mobileNetV2 to explore the time-frequency characteristics of different damage-induced AE signals [176]. The results of the classification of AE signals showed that ResNet18 achieved the highest overall accuracy of 93.94% [176]. Han et al. successfully monitors cracking up scaling from specimen concrete structures using acoustic emission and convolutional neural networks [176]. Sikdar et al. proposed a deep learning approach based on acoustic emission data for classification and detection of damage sources in a composite panel. They measured their AE signals through the piezoelectric sensor array. They used continuous wavelet transform (CWT) to extract time-frequency scalograms. They constructed a CNN to automatically extract the discrete damage features from the scalogram images [177]. The proposed deep learning approach has shown the potential for effective damage monitoring with high learning accuracy and proposed an image augmentation approach in their research work to generate training data [177]. Barile et al. monitored the damage of carbon fiber reinforced polymer composites using the acoustic emission technique and deep learning. They classified the AE Spectrograms from four damage modes matrix cracking, delamination, debonding and fiber breakage which were obtained in the Mel scale. The overall accuracy of their prediction is 97.9%. However, they made a special observation that the fiber breakage and delamination events could be predicted with 100% accuracy [178] And Xu et al. also used AE and CNN for damage prognostics of fiber-reinforced composite laminates [175].

In this chapter, a deep learning framework based on two types of CNN architecture (alexNet and squeezeNet) and a new model. First, tensile tests were performed, and AE signals were recorded from these tests. The CNN models were used to classify the acoustic emission signals

according to the stages of damage (elastic and plastic deformation) and the acoustic emission signals of the building configuration of the specimens (Tx, Ty Tz and T45) and the AE signals having similarities in these specimens. Certain parameters were varied to see their impact on the accuracy of the constructed CNN models, notably the size of the input data and the activation function and pooling layer. A comparison of the three different CNNs as a function of their learning time and accuracy.

5.2 CNN Methodology for Damage mechanisms Classification

The materials, testing methods, and mechanical results from the tensile tests are explained in detail in Chapter 4**.** The CNN models (AlexNet, SqueezeNet, and a simplified CNN) were used to classify the AE signals discussed in Subsection 3.2.1.1**.** These models were applied to classify AE signals according to the stages of damage (elastic and plastic deformation) and to differentiate between the build orientations of the specimens (Tx, Ty, Tz, and T45). The classification approach utilizes an 'image classification' method based on the Continuous Wavelet Transform (CWT) and Convolutional Neural Network (CNN). The CWT, which is detailed in subsection 3.1.3.1**,** is applied to AE signals to generate time-frequency scalograms. These scalograms are treated as images and fed into the CNN models for classification. Various CNN parameters, such as input data size, activation functions, and pooling layers, were adjusted to optimize the classification accuracy of the models.

5.3 Results and Analysis

5.3.1 Damage characterization using CWT of AE signals

During the tensile test, the AE signals of four groups of specimens were extracted. Figure 5.1 shows the representative waveforms of the AE signals received from the specimens constructed in four different orientations. Figure 5.2 shows the spectrograms of the AE signals for four specimen orientations obtained with the CWT. Observation of the AE signals and the spectrogram revealed that Tx and Ty can be considered equivalent. By examining the spectral content within a given class, an order of magnitude of 0.005-0.3 is observed for Tx in the frequency range 200 kHz-300 kHz see figure 5.3(a). For Ty, in the same frequency range and time interval as Tx, the magnitude varies by 0.005-0.05, see figure 5.3(b). For Tz, from 250 kHz-300kHz, the magnitude varies from 0.05-0.03 see on figure 5.3 (c). And finally, for T45, in the frequency range of 50kHz -300kHz, a magnitude of 0.01-0.1 see figure 5.3(d). A similarity is observed between the AE signals Tx and Ty, in contrast to the AE signals of Tz and T45. Figure 5.4 shows the scalogram of the different stages of elastic and plastic damage. During the elastic stage, a spectral energy is observed in the frequency range of 200kHz to 300kHz, varying in the order of 0.2-1.5 magnitude. A similar observation was made with the spectrogram of the plastic phase, where the frequency content is also found in the range of 200kHz to 300kHz, but a difference in magnitude of 0.005-0.04 is observed, which is considered small compared to the elastic stage, see Figure 5.4 (a),(b).

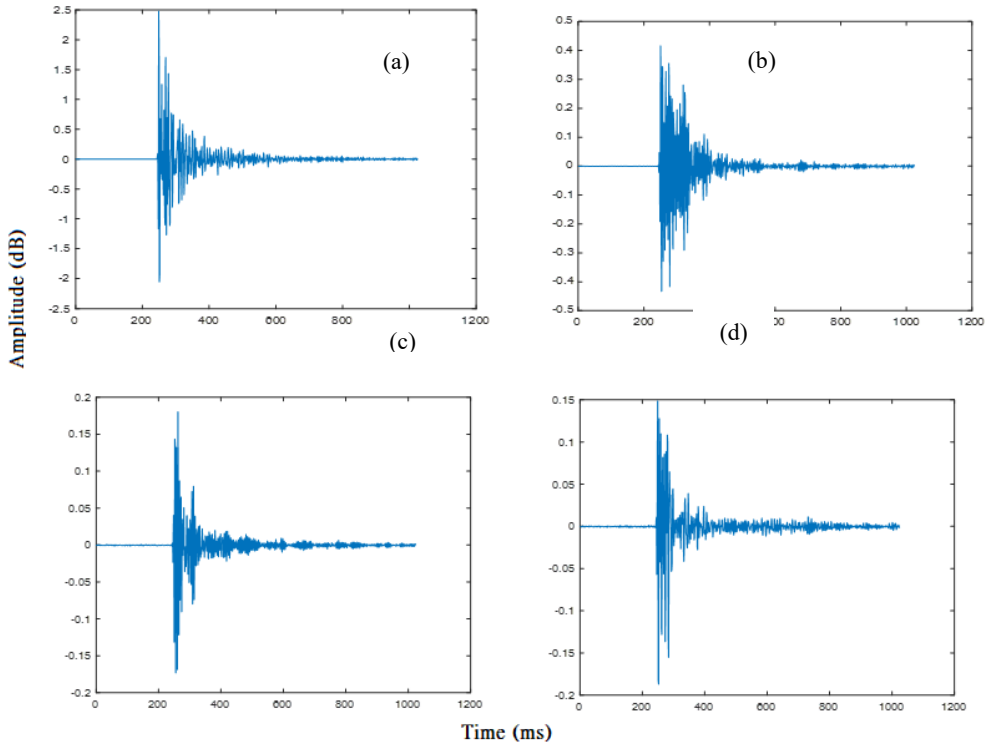

Figure 5.1: Representative Waveforms of the received AE signals for the specimens built in four different orientations (a)Tx, (b) Ty, (c) Tz, (d) T45.

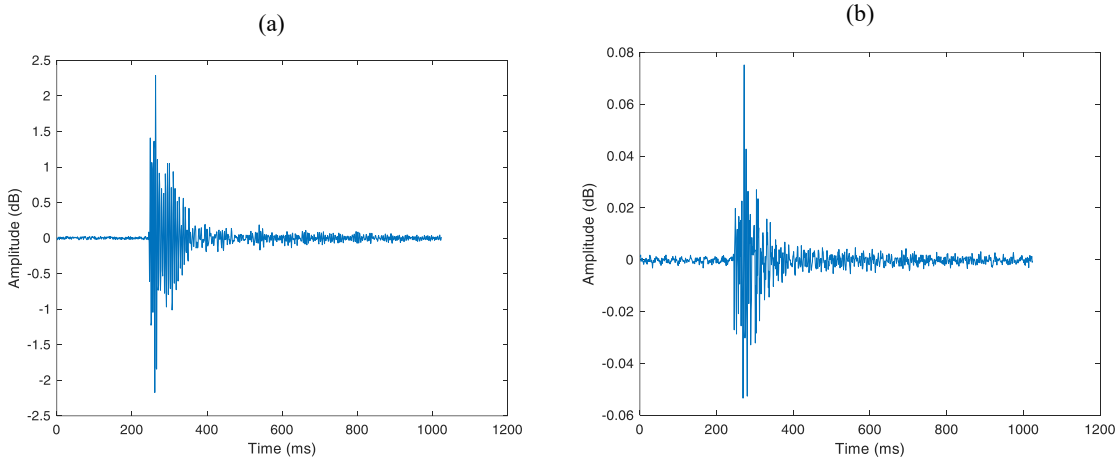

Figure 5.2: (a) Representative Waveforms of AE signal from Elastic Stage, (b) Representative Waveforms of AE signal from Plastic Stage

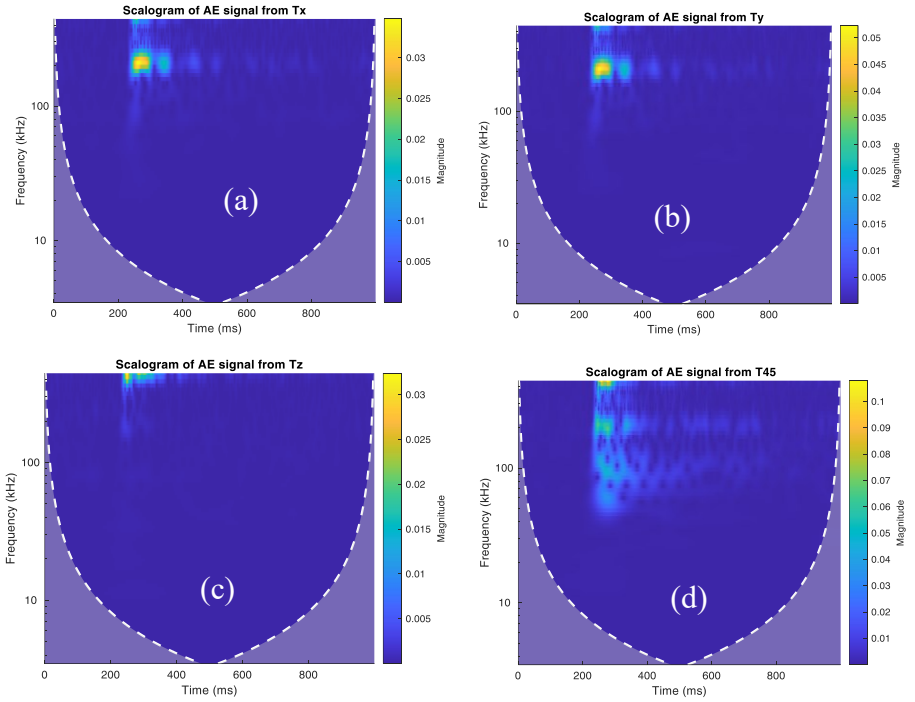

Figure 5.3: Spectrogram of AE signal from (a) Tx, (b) Ty, (c) Tz, and (d) T45.

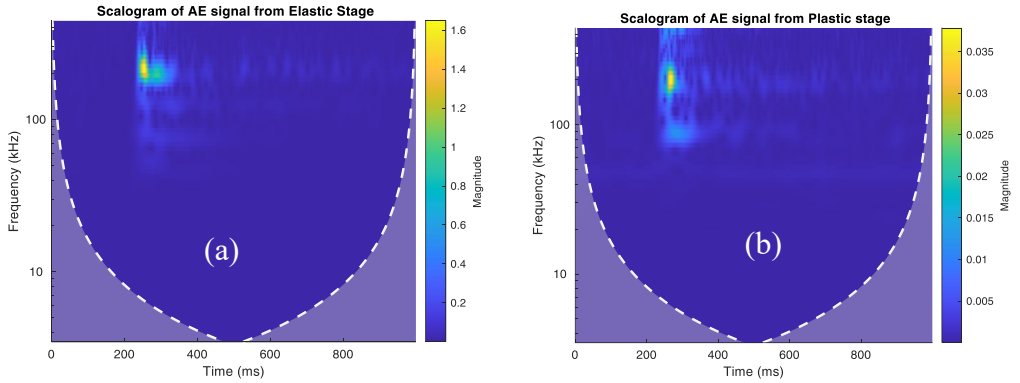

Figure 5.4: Spectrogram of AE signal from (a) Elastic Stage and (b) Plastic Stage Damage classification using Deep Learning

The analysis and processing of AE signals collected during the tensile test has been explained in the previous section. These collected AE signals are analysed by CWT in time-frequency domain and visualised with the spectrogram. The frequency-time content made it possible to categorise the AE signals based on their similarities. This categorisation is shown in Figure 5.5. The CNN is used to efficiently classify groups of AE signals based on their similarities. The first mode analysis is used to make a comparison between the CNN models considered in this work (AlexNet, SqueezeNet, the new model). The second mode of analysis represent the contribution of a new simple CNN model, but with better configurations. Finally, the minimum set to achieve a better classification of AE signals**.** The stochastic gradient descent algorithm with momentum is used to train the CNNs. The initial learning rate is set to 0.0001, the maximum number of epochs for learning is 50, the mini batch with 30 and with three validation frequency observations. In order to achieve a better comparison of the results, all the training, validation and testing of the three different CNN were performed in the same laptop with the

configuration. The processor is 11th Gen Intel(R) Core i7-1195G7 and has a speed of 2.92 GHz, with 16.0 GB RAM. The total number of images from each training mode is separated into 3 parts: 50% for training the CNN, 25% for validating its accuracy and 25% for testing to rule out the overfitting of results.

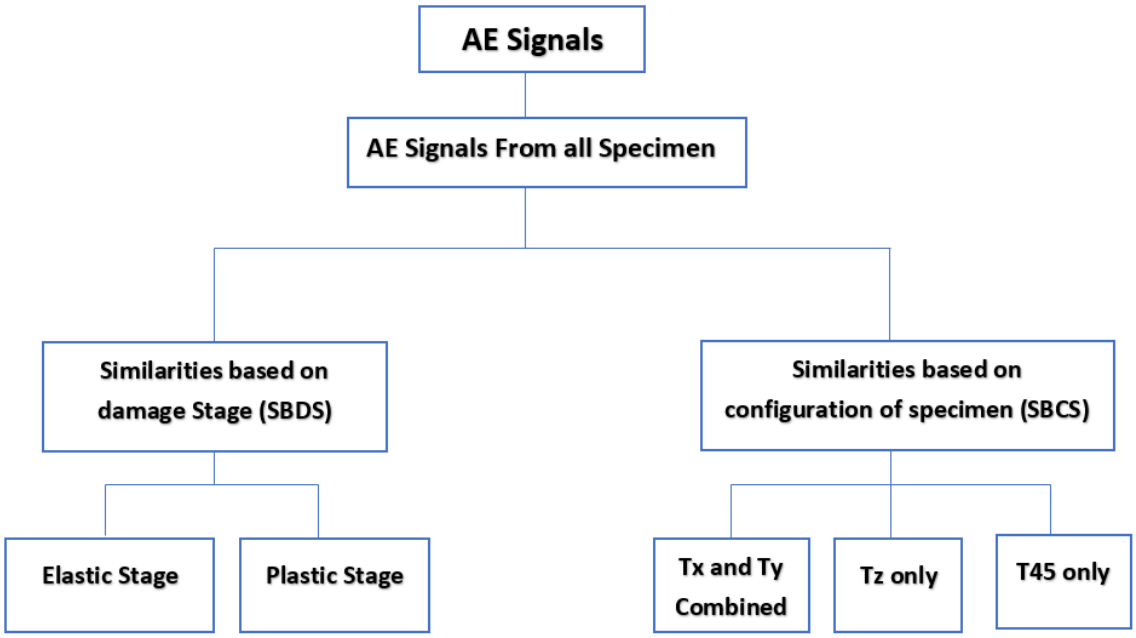

Figure 5.5: Categorization of AE signals based on similarities

5.3.2 Classification of AE signals based on damages stage

AlexNet, SqueezeNet and the proposed model were built on Matlab (2022a) using the Deep Network Designer Toolbox. Several training modes were performed to make a CNN comparison and determine the best configuration. Table 4.1 shows the result of classifying the AE signal groups based on the damage stages. Four training modes were tested for the three CNN models (alexNet, SqueezeNet and the new model). The first training mode TM 1 used 200 image inputs, the sigmoid activation function, and average pooling for pooling function. The results obtained are shown in Figure 5.6, for alexNet, SqueezeNet and the new model are at 50% accuracy. An observation was made on the training time of each CNN: alexNet 56 minutes 28 seconds, squeezeNet 46 minutes 04 seconds, the new model 26 minutes 46 seconds. For the second mode TM 2, all parameters were kept as in the first training mode, except for the activation function, which was changed from Sigmoid to ReLu. The results are shown in Table 4.1 and Figure 5.7. By changing the activation function, the accuracy of all CNN models reached the maximum value of 100%. The difference in training time was observed for each model: AlexNet 40 minutes 27 seconds, squeezeNet 25 minutes 45 seconds and the new model 19 minutes 22 seconds. In addition, the training time for each CNN model decreased by about 20 % when the ReLu activation function was used. For the third training mode TM 3, the same parameters were used as for the first mode, but with a higher image input in 1000. Thus, 500 images input were used for each class (elastic and plastic stage). The result shown in Table 4.1 shows that AlexNet achieved 50% accuracy, SqueezeNet 48.7% and the new model 50%. The

development time increased with the amount of input data, 3 hours 29 minutes for AlexNet, 2 hours 57 minutes for SqueezeNet and 1 hour 46 minutes for the new model. The fourth training mode TM 4, using 1000 images with the ReLu activation function. The results obtained are presented in Table 4.1, where 100% accuracy was achieved for all CNN models. The processing time for alexNet is 2 hours 07 minutes, for SqueezeNet 61 minutes 16 seconds and for the new model 36 minutes 32 seconds. Based on all the training modes performed to automatically classify the damage stages of AlSi10Mg specimens. Few observations were made. First, the training time of AlexNet is greater than that of squeezeNet, and the new model, especially for the high number of parameters [179]. Secondly, the ReLu activation function converges quickly and therefore takes much less time than models trained with the sigmoid function. The sigmoid activation function is a fraction between 0 and 1. As the layers multiply, the global gradient becomes exponentially small, so each step along the gradient causes only a tiny change to the weights [180]. With ReLu activation, on the other hand, the gradient is either 0 or 1, so the global gradient is neither too small nor too large [180].

Table 4.1. Classification of AE signals based on damage stage

N° Training mode [Tm]	Model	Number of inputs	Type of activation function	Pooling Avg/Max	Validation [%]	Testing [%]	Times
TM 1	AlexNet	200	Sigmoid	Avg/Max	50	50	56 min 28s
	SqueezeNet	200	Sigmoid	Avg/Max	50	50	46 min 04s
	New Model	200	Sigmoid	Avg/Max	50	50	26 min 46s
TM 2	AlexNet	200	ReLu	Avg/Max	100	100	40 min 27s
	SqueezeNet	200	ReLu	Avg/Max	100	100	25 min 45s
	New Model	200	ReLu	Avg/Max	100	100	19 min 22s
TM 3	AlexNet	1000	Sigmoid	Avg/Max	50	50	3h 29min
	SqueezeNet	1000	Sigmoid	Avg/Max	48.7	50	2h 57min
	New Model	1000	Sigmoid	Avg/Max	50	50	1h 49min
TM 4	AlexNet	1000	ReLu	Avg/Max	100	100	2h 07min
	SqueezeNet	1000	ReLu	Avg/Max	100	100	1h 16min
	New Model	1000	ReLu	Avg/Max	100	100	36min32s

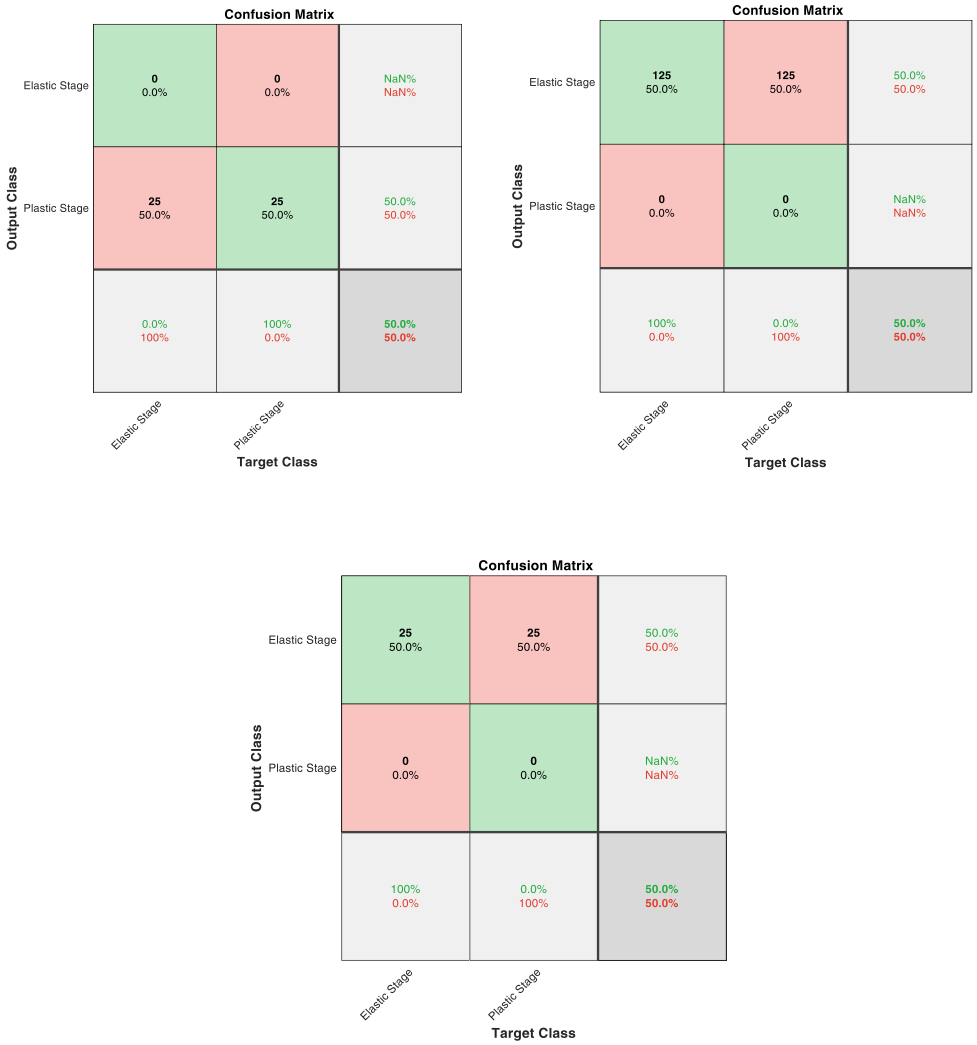

Figure 5.6: Classification based on damage stage using TM 1 (a) AlexNet, (b) SqueezeNet, and (c) Proposed model CNN.

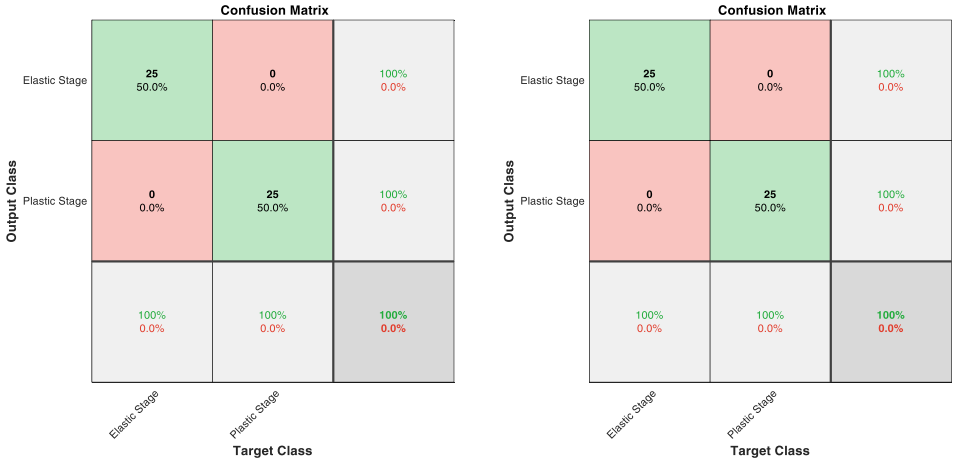

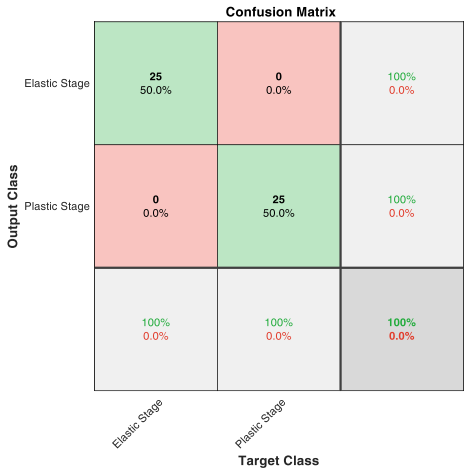

Figure 5.7: Classification based on damage stage using TM 2 (a) AlexNet, (b)SqueezeNet, and (c) Proposed model CNN.

5.3.3 Classification of AE signals based on configuration of specimen

The same observation was made for the AE signals categorized based on their configurations (Txy, Tz, T45). Looking at the results presented in Table 5.2, a simultaneity is observed with the first damage-based categorization, where the accuracy increases when the sigmoid activation function is replaced with ReLu. But again, let us observe that the accuracy is still 33. 3% lower, for AE signals from different specimen orientations. But by increasing the input data, a particular observation was made on the new model, the accuracy increases by 66.7%, compared to alexNet and SqueezeNet. Finally, by changing the sigmoid activation function to ReLu, an accuracy of 100% is achieved.

Table 5.2. Classification of AE signals based on configuration of specimen.

N° Training mode [TM]	Model	Number of inputs	Type of activation function	Pooling Avg/Max	Validation [%]	Testing [%]	Time
TM 1	AlexNet	300	Sigmoid	Avg/Max	33.3	33.3	1h 9min
	SqueezeNet	300	Sigmoid	Avg/Max	33.3	33.3	58 min 20s
	New Model	300	Sigmoid	Avg/Max	33.3	33.3	35 min 04s
TM 2	AlexNet	300	ReLu	Avg/Max	100	100	49 min 06s
	SqueezeNet	300	ReLu	Avg/Max	100	100	38 min 07s
	New Model	300	ReLu	Avg/Max	100	100	24min 00s
TM 3	AlexNet	1500	Sigmoid	Avg/Max	33.3	33.3	4h 39 min
	SqueezeNet	1500	Sigmoid	Avg/Max	33.3	33.3	3h 35 min
	New Model	1500	Sigmoid	Avg/Max	33.3	33.3	2h01 min
TM 4	AlexNet	1500	ReLu	Avg/Max	100	100	3h 10 min
	SqueezeNet	1500	ReLu	Avg/Max	100	100	2h 39 min
	New Model	1500	ReLu	Avg/Max	100	100	1h 40s

5.3.4 Classification of AE signals from individual specimen

In this section, the group of AE signals originating from a individual specimen is classified in terms of their configuration (Tx, Ty, Tz and T45). Based on the previous result (see the Table 5.3), the ReLu activation function has been shown to be effective in classifying the AE signals. Based on this optimal configuration of CNNs, this section examines the amount of data needed to train a CNN to achieve 100% accuracy.

The results are shown in Table 5.3. In the first training mode TM 1, 400 input data were used, considering 100 per class (Tx, Ty, Tz and T45) using the ReLu activation function. Figure 5.8 shows the result, for alexNet 65.0%, squeezeNet 62.0% and for the new model 68.0% accuracy. The processing time behaves the same as the previous result. Finally, when the input images are increased from 400 to 2000 at a rate of 500 per class, the improvement is seen, which is 85.5% for alexNet, 81.1% for squeezeNet and 90.1% for the new model, see Figure 5.9. Thus, for the best CNN configurations, the amount of input data affects the classification accuracy. A simplified CNN model can have better classification accuracy.

Table 5.3. Classification of AE signals from individual specimen based on configuration.

N° Training mode [TM]	Model	Number of inputs	Type of activation function	Pooling Avg/Max	Validation [%]	Testing [%]	Time
TM 1	AlexNet	400	ReLu	Avg/Max	68.3	65	1h 16 min
	SqueezeNet	400	ReLu	Avg/Max	61.7	62	55min 01s
	New Model	400	ReLu	Avg/Max	69.7	68	40 min 05s
TM 2	AlexNet	2000	ReLu	Avg/Max	97.2	85.5	4h 37min
	SqueezeNet	2000	ReLu	Avg/Max	96.4	81	4h 07min
	New Model	2000	ReLu	Avg/Max	97.8	90.1	2h 50min

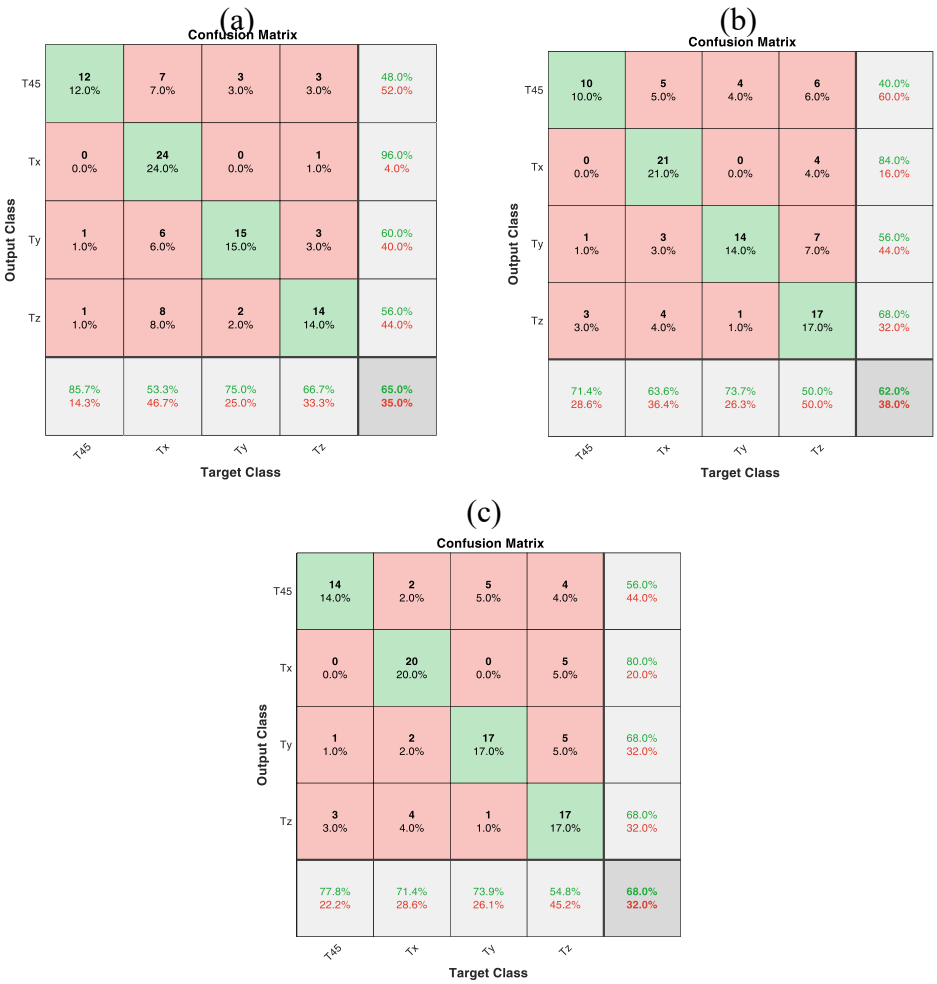

Figure 5.8: Classification based on the signals generated from individual specimens using TM 1 (a) AlexNet, (b)SqueezeNet, and (c) Proposed model CNN

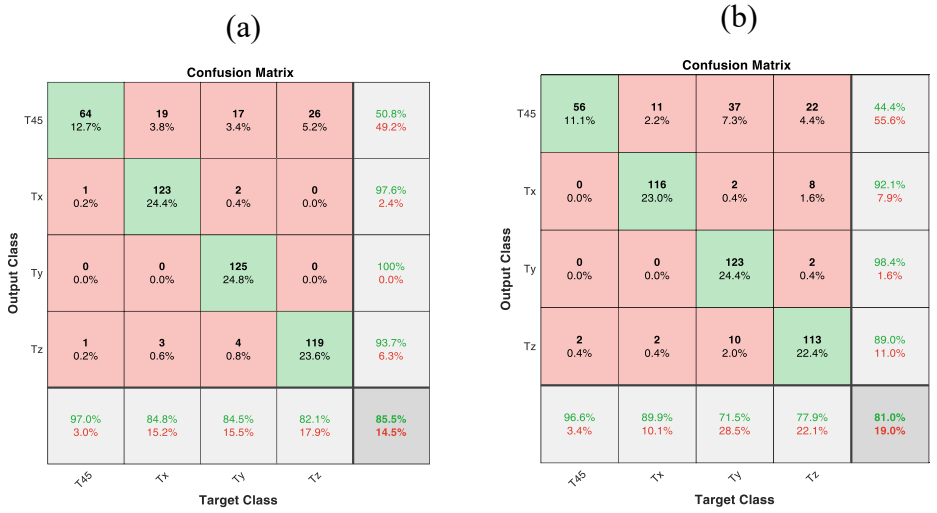

(c)

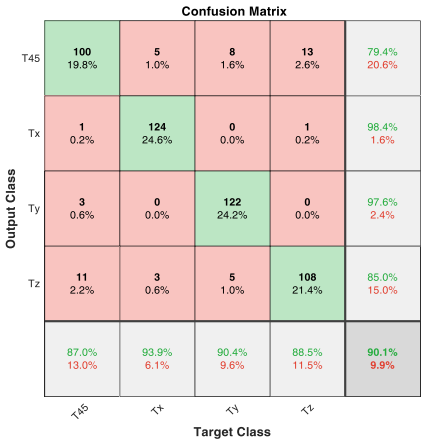

Figure 5.9: Classification based on the signals generated from individual specimens using TM 2 (a) AlexNet, (b)SqueezeNet, and (c) Proposed model CNN.

5.4 Conclusion

This chapter presents a deep-learning approach using AE data to characterize and classify different stages of deformation (elastic and plastic) and various specimen configurations (Txy, Tz, T45) in AlSi10Mg samples produced through the SLM process. The approach begins with tensile testing, during which AE signals are captured and subjected to time-frequency analysis using CWT to generate spectrograms. These spectrograms distinguish AE signals corresponding to different damage stages and specimen configurations. Three CNNs, AlexNet, SqueezeNet, and a newly developed model, were then trained on the spectrograms. A comparison of these CNN models was conducted, focusing on their classification accuracy and development time. Several training experiments were performed to determine the amount of data needed to achieve 100% accuracy. It was found that switching from Max-Pooling to Average-Pooling had no impact on results, while the sigmoid activation function yielded lower accuracy (50% for damage stage classification and 33.3% for specimen configuration). In contrast, using the ReLu activation function enabled each CNN model to achieve 100% accuracy. Although all CNNs reached the same accuracy, they differed in learning time. The newly developed, simplified CNN model classified AE signals faster than AlexNet and SqueezeNet, which contain a larger number of parameters. Additionally, the classification performance improved as the amount of input data increased. Overall, the results demonstrate that the simplified CNN model can achieve the same accuracy as AlexNet and SqueezeNet, but with significantly reduced processing time. The next chapter will present a new methodology using the same materials and test methods.

Chapter 6. Enhancing the AE Technique Using Fuzzy Artificial Bee Colony and Deep Learning for Characterizing SLM AlSi10Mg Specimens for Aerospace Applications

This chapter presents an enhanced methodology using the Fuzzy Artificial Bee Colony (FABC) algorithm combined with deep learning to improve the classification of AE signals from AlSi10Mg specimens produced via Selective Laser Melting (SLM). The materials, testing methods discussed in Chapter 4 form the foundation of this analysis.
The AE signals were analyzed using the Continuous Wavelet Transform (CWT), as explained in Subsection 3.1.3.1. A new data augmentation strategy, detailed in Subsection 3.2.1.2, applied Gaussian white noise to enhance the model's robustness. Cross-validation was used to further validate the model and prevent overfitting.
The FABC-CNN approach addresses three key challenges. It resolves the issue of suboptimal local maxima during model training, as explained in Section 3.2.2. It also introduces a new data augmentation strategy to enhance model performance. Finally, cross-validation confirmed the robustness of the model compared to the approach developed in the previous chapter.

6.1 Introduction

Selective laser melting (SLM) is an additive manufacturing technique that uses a laser to melt powder materials layer by layer to produce 3D components [181]. The SLM has several advantages over conventional mechanical manufacturing processes, including design freedom, which enables the production of components with complex shapes that would be difficult to produce using conventional methods [182]. Due to its excellent welding performance, excellent fluidity, and mechanical properties, AlSi10Mg has become one of the most widely used aluminium alloys suitable for aerospace and automotive applications [183]. In addition, it is one of the most commonly used aluminium alloys for the SLM process. Recent research has demonstrated, however, that construction orientation can have direct effects on the anisotropy and microstructural heterogeneity of SLM components, necessitating the consideration of appropriate manufacturing strategies to ensure optimal material properties [158], [184], [185]. This research aims to study the mechanical characteristics of AlSi10Mg components produced by the SLM manufacturing process, depending on different build orientations. Over the past few decades, several non-destructive testing (NDT) techniques have been developed to diagnose various damages in materials or structures without compromising their integrity[186]. Among these techniques, AE has recently gained increasing interest in evaluating the intrinsic state of materials and structures [186], [187]. This technique enables the detection of microstructure changes, cracks, and other material defects when internal or external stresses are applied[98]. When a material is subjected to stress, part of the stored energy is released as transient elastic waves. The generation and propagation of these waves can be detected by specific sensors (piezoelectric) attached to the surface of the tested object. The frequencies of these waves range from kHz to MHz and are transformed into electrical signals, called AE

signals[188]. AE signal analysis methods allow establishing a correlation between the process of damage evolution in space or time and the measured signals [189]. Although significant progress has been made in the diagnosis of structural and component defects based on AE signal analysis, it is still challenging to extract and identify effective characteristics that are sensitive to initial structural damage in materials. Conventional methods for processing AE signals are mainly focused on characteristic parameter analysis [190] and waveform analysis [191]. Based on waveform analysis using CWT, it is possible to extract information in terms of time and frequency, allowing for the detection of the most sensitive characteristics of damage. Unlike traditional methods that may lose important signal characteristics, CWT allows for a more complete characterization of the non-stationary signal captured by AE [192]. In summary, CWT is an effective time-frequency analysis method for extracting characteristic information from AE signals for the purpose of diagnosing material damage.

Damage characterization, feature selection, damage classification and failure prediction are vital aspects of material and structure health monitoring. Deep learning approaches based on convolutional neural networks (CNN) and CWT which characterize the AE signal as a two-dimensional time-frequency image are currently used in real-time material characterization and classification [192] . The combination of CNN and CWT has led to significant success in various research studies [193], [194]. While ordinary CNNs have shown significant performance, there is still room for improvement[195]. CNNs are frequently very complex, with a large number of parameters that must be optimized[196]. Due to this complexity, it is possible to get stuck in a suboptimal local minimum rather than reaching the global optimum[197]. By efficiently exploring the search space, metaheuristic algorithms can assist in avoiding this situation[198]. Various studies over the last two decades have demonstrated the vast potential of metaheuristic algorithms in solving optimization problems in a wide range of scientific and engineering fields [199], [200]. However, research on the application of metaheuristic algorithms to the optimization of CNNs, particularly on the AE signal, is extremely uncommon. Recently, other meta-heuristic algorithms, such as genetic algorithms, particle swarm optimization, and artificial bee colonization algorithms, have been combined with CNN in different fields to improve classification performance [137], [201].

In the present research, a fuzzy artificial bee colony (FABC) algorithm is used to enhance the performance of a proposed CNN model. In essence, this method minimizes classification errors by initializing the CNN classifier weights based on the FABC algorithm output solutions. The CNN-FABC is used to classify AE signals related to specimen's configuration (X, Y,45°, and Z), the stage of deformation and the damage modes of all specimens. In addition, the mechanical characteristics of AlSi10Mg components manufactured using AM-SLM in different directions have been investigated.

6.2 Fuzzy Artificial Bee Colony- CNN algorithm Methodology

This section provides an overview of the steps involved in applying the Fuzzy Artificial Bee Colony (FABC)-CNN methodology to improve the classification of Acoustic Emission (AE) signals for AlSi10Mg specimens produced via Selective Laser Melting (SLM). The materials, testing methods, and mechanical behavior results discussed in Chapter 4 form the basis for this analysis. while the detailed methodologies are covered in Section 3.2.2.

Step-by-Step Procedure:

1. Signal Acquisition: AE signals were acquired during the tensile tests performed on specimens built in different orientations (X, Y, 45°, and Z). These signals were recorded throughout the tests to capture the mechanical behavior across different deformation stages (elastic and plastic).

2. Data Augmentation: A new data augmentation strategy was applied to enhance the AE signals. This strategy, detailed in Subsection 3.2.1.2, involved the addition of Gaussian white noise to the original AE signals. The purpose was to generate a large set of synthetic signals by carefully adding noise in a specific way, which helped improve the robustness of the model.

3. Time-Frequency Analysis (CWT): The augmented signals were then processed using the Continuous Wavelet Transform, as explained in Subsection 3.1.3.1. This technique extracted time-frequency features from the AE signals, transforming them into scalograms, which represent the signals visually in the time-frequency domain.

4. FABC-CNN Model Application: The scalograms were treated as input images for the FABC-CNN model. The FABC algorithm was used to optimize the parameters of the CNN, ensuring better learning and avoiding suboptimal local maxima during the training process. The CNN model was trained to classify the AE signals based on the damage stages (elastic and plastic) and the different build orientations of the specimens (X, Y, Z, 45°). This methodology improved the classification accuracy and robustness of the model for detecting damage mechanisms in aerospace materials.

6.3 Results and Analysis

6.3.1 Tensile Test Results

In this study, the results of the tensile test for different print directions (X, Y, Z, and 45°) are presented in Table 6.1. The table shows that the yield strength, ultimate tensile strength, and Young's modulus of groups X, Y, and 45 are significantly higher than those of group Z. ANOVA analysis were performed to compare the mechanical properties of ALSI10 Mg specimens. The yield strength exhibited a highly significant difference between printing directions (p 0.001), with the highest average value observed in the Z direction (122.7 MPa), followed by X (136.6 MPa), 45° (138.2 MPa), and Y (139.3 MPa). The pairwise comparison indicated that the Z direction had a significantly lower yield strength than the other directions (see Figure 6.1a). The ultimate tensile strength also showed a significant difference between printing directions (p = 0.004), with the highest average value obtained in the Y direction (221.1 MPa), followed by 45 (215.8 MPa), X (211.7 MPa), and Z (202.8 MPa). The pairwise comparison showed that the Y direction had a significantly higher ultimate tensile strength than the Z direction (see Figure 6.1b). Young's modulus also exhibited a significant difference among printing directions (p = 0.011), with the highest average value observed in the Y direction (71.0 GPa), followed by 45 (68.2 GPa), X (63.3 GPa), and Z (59.7 GPa). The pairwise

comparison indicated that the Y direction had a significantly higher Young's modulus than the Z direction (see Figure 6.1c). The elongation at break, as well, showed a highly significant difference among printing directions (p 0.001), with the highest mean value observed in the 45 direction (4.4%), followed by X (3.4%), Y (2.9%), and Z (1.4%). The pairwise comparison showed that the 45-degree direction had a significantly higher elongation at break than all other directions (see Figure 6.1d). In addition to the mechanical properties, other factors such as the slenderness ratio and borderline porosity of the specimens may have contributed to the observed differences in mechanical behavior. Further information regarding the mechanical properties and their relationship with the printing orientations can be found in previous research papers by the authors [185], [195], [202]. However, the present study mainly focused on the analysis of acoustic emission results, and thus, post-processing was not carried out to improve the mechanical properties. The stress-strain curves (see Figure 6.2) allow to define two stages (elastic and plastic) of deformation considered in this work according to the ASTM E8 standard.

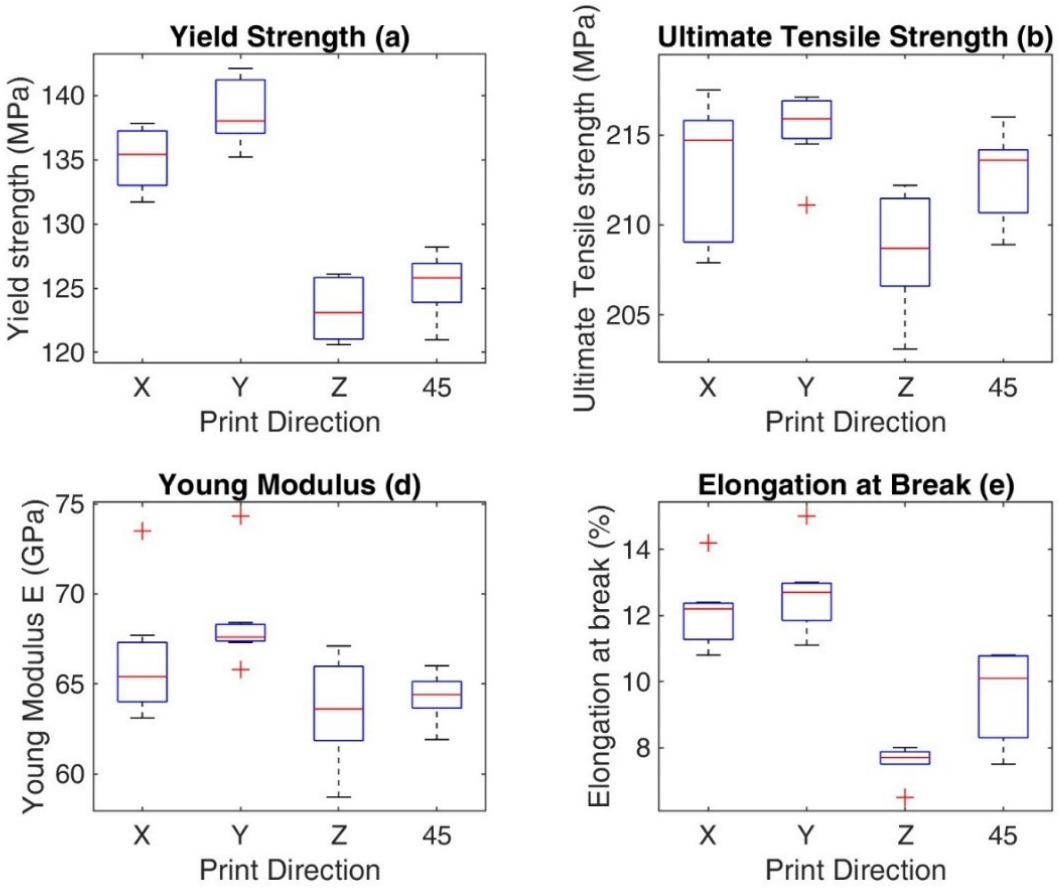

Figure 6.1: ANOVA results: (a)Yield strength, (b) Ultimate tensile strength, (c) Young's modulus, (d) Elongation at break

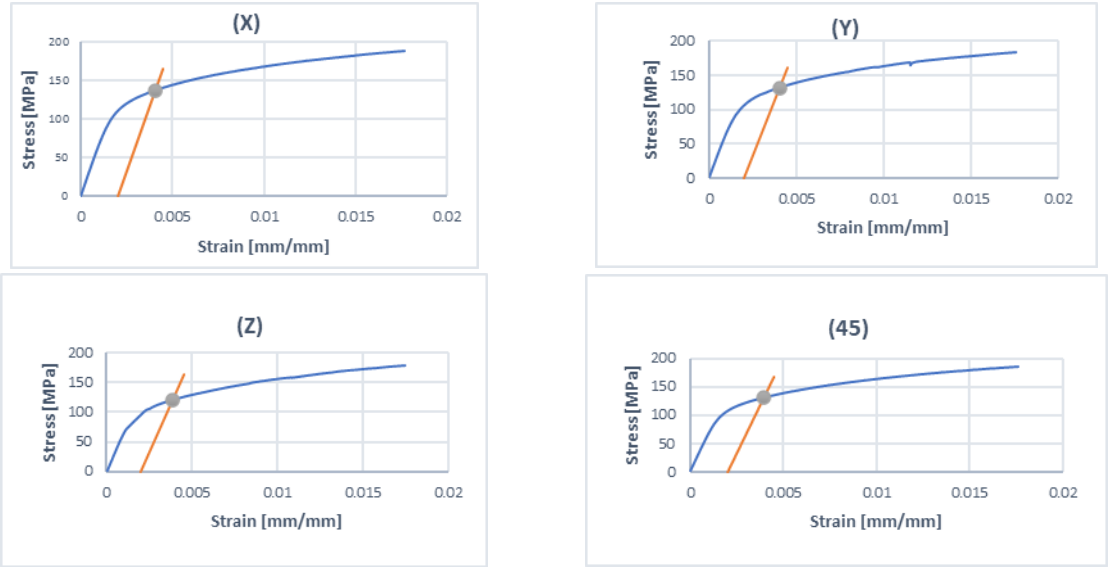

Figure 6.2: Stress–strain curves of specimen specimens tested X, Y, Z, and 45.

Table 6.1. Results of the tensile tests carried out on all specimens

Print Direction	Specimen Group	Yield strength	Ultimate tensile strength	Young's modulus	Elongation at break
		MPa	MPa	GPa	%
X	S_X1	137.4	214.9	65.4	12.3
	S_X2	135.4	217.5	67.7	12.2
	S_X3	137.8	214.7	66.1	12.1
	S_X4	136.7	216.1	73.5	14.2
	S_X5	132.5	209.0	63.1	12.4
	S_X6	131.7	207.9	64.9	10.8
	S_X7	134.5	209.2	63.7	11
Y	S_Y1	135.2	211.1	67.6	12.9
	S_Y2	138.0	217.0	67.6	15.0
	S_Y3	142.1	216.6	68,0	11.1
	S_Y4	137.5	215.7	74.3	12.7
	S_Y5	141.3	215.9	67.3	11.6
	S_Y6	136.9	214.5	65.8	12.6
	S_Y7	140.9	217.1	68.4	13.0
Z	S_Z1	120.6	203.1	58.7	6.5
	S_Z2	126.1	211.5	67.1	7.8
	S_Z3	122.1	208.7	61.7	8.0
	S_Z4	126.0	211.4	64.4	7.5
	S_Z5	120.7	206.1	66.5	7.9
	S_Z6	125.3	212.2	63.6	7.7
	S_Z7	123.1	208.1	62.3	7.5
45°	$S_{45°}1$	121.0	208.9	61.9	10.8
	$S_{45°}2$	127.2	213.6	64.9	10.8
	$S_{45°}3$	123.7	209.9	64.4	7.5

$S_{45°}4$	125.8	214.1	66.0	10.1
$S_{45°}5$	126.1	213	65.2	8.0
$S_{45°}6$	124.5	214.2	63.5	10.7
$S_{45°}7$	128.2	216	64.1	9.2

6.3.2 Damage Mode Characterization Based on Cumulative Acoustic Emission Energy

The cumulative energy is one of the acoustic emission parameters widely and effectively used to characterize damage in materials[203], [204], [205], [206]. It is defined as the total amount of energy of the acoustic event recorded over the time range from t_0 to t_i. If U_i is denoted as the transient voltage of this recorded acoustic event, the acoustic energy AE is determined by Equation (6.1):

$$E_{AE} = \int_{t_0}^{t_i} U_i^2(t)dt \tag{6.1}$$

Precise quantification of damage modes based solely on mechanical properties (stress, strain, temperature...) is quite complex [207]. Acoustic emission reflects various stages of material deterioration, including initiation, crack growth, and fracture [208], [209]. However, a joint analysis of AE descriptors and mechanical properties offers a more comprehensive perspective, enabling a better interpretation of the underlying damage mechanisms [163], [210] . In this work, the stress-strain curve of ALSI10Mg specimens built on several orientations (X, Y, 45°, and Z) are superimposed on the cumulative AE energy and are presented in figure 11.

The stress-strain curve and associated cumulative acoustic emission (AE) energy delineate four distinct phases, labelled Zones I through IV. The zone I aligns with the material's elastic region, marked by minimal AE energy, indicating scant defect activity and low stress-strain levels (Aggelis et al., 2011). Specimens X, Y, 45°, and Z exhibited stress ranges from 0 to 130.5, 0 to 131.9, 0 to 158.9, and 0 to 148.5 MPa respectively (See Table 5), with corresponding minimal strains, indicating linear elastic behavior. This phase is characterized by strains of 0 to 3.4E-3 mm/mm for Specimen X, 0 to 3.7E-3 mm/mm for Specimen Y, 0 to 7.7E-3 mm/mm for Specimen 45°, and 0 to 5.7E-3 mm/mm for Specimen Z (See Table 5), showcasing the initial elastic response of the materials. The zone II signifies the onset of plastic deformation initiation and microstructural damage, identified by a deviation from linear stress-strain behavior and evidenced by increased AE energy, stress, and strain (Rodríguez and Celestino, 2019). Here, Specimen X transitions with stress values ranging from 130.5 to 156.6 MPa, illustrating the beginning of plastic strain, a critical phase in understanding material behavior under stress. Specimens Y, 45°, and Z similarly show gradual increases in both stress and strain, with values indicating the material's transition towards plasticity, marked by strains from 14E-3 to 17.6E-3 mm/mm for Specimen X, 3.7E-3 to 10.9E-3 mm/mm for Specimen Y, 7.7E-3 to 10.8E-3 mm/mm for Specimen 45°, and 5.7E-3 to 11.6E-3 mm/mm for Specimen Z (See Table 5). The zone III is noted for a pronounced rise in AE energy parallel to stress and strain, likely signalling crack propagation and failure mechanisms such as cavitation [211]. This is further supported by the observed progression in stress and strain in all specimens, with values suggesting the continuation of plastic deformation and advancing towards material failure. The

zone IV, characterized by a sharp surge in AE energy and stress-strain, heralds imminent material failure, forecasting large-scale fracturing [212], [213]. This zone is indicative of damage strain, where Specimens X, Y, 45°, and Z all exhibit peak stress values ranging from 180.4 to 187.8 MPa, with corresponding strains indicating advanced material damage and the onset of damage strain, ranging from 14E-3 to 17.6E-3 mm/mm across specimens (see Table 6.2), highlighting the critical nature of this phase in predicting material failure. In this analysis, specific observations highlight the behavior of Specimens X, Y, 45°, and Z, particularly in terms of their AE energy distributions and mechanical properties. The specimens X and Y demonstrated remarkably similar behaviours, with their cumulative AE energy achieving nearly identical maximum levels. This parallelism implies a strong correlation between their mechanical properties, as detailed in Figure 6.3. In contrast, Specimens 45° and Z exhibited distinct behaviours regarding AE energy distribution, which aligns with their mechanical properties (refer to Figure 6.3). Notably, Specimen Z showed a significantly lower cumulative AE energy, indicative of its unique mechanical property profile. The analysis of Specimen Z's mechanical properties, encompassing yield strength, elongation at break, and ultimate tensile strength, indicated values lower than those of the other specimens. This structured narrative not only provides a theoretical basis for understanding material behavior under stress but also incorporates critical observations about the unique and shared characteristics of the specimens. By highlighting these distinctions and similarities, the narrative offers a deeper insight into the material properties and structural integrity of each specimen, enhancing the scientific understanding of their mechanical responses.

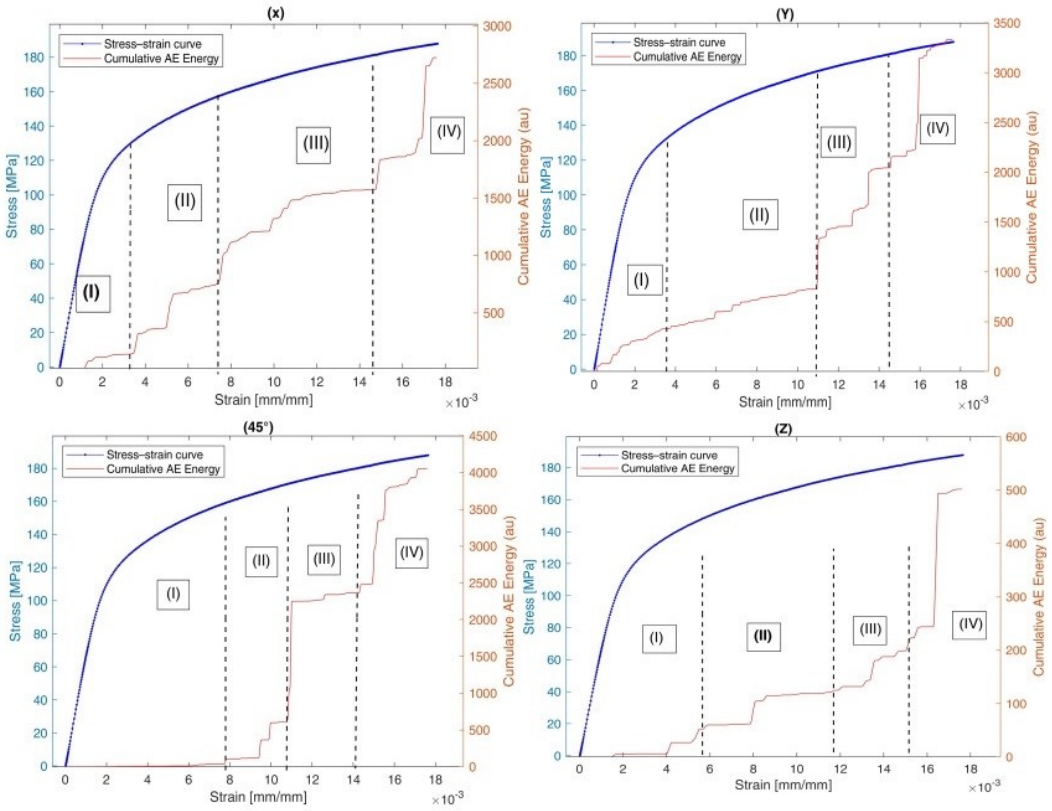

Figure 6.3: Typical stress–strain curves and cumulative AE energy of AlSi10Mg specimens based on printing direction: Specimen (X), (Y), (45°), and (Z)

Table 6.2. Synthesis of Mechanical Properties by Zone

Specimen Print Direction	Zone	Stress Range (MPa)	Strain Range (mm/mm)
X	I	0 - 130.5	0 - 3.4E-3
X	II	130.5 - 156.6	3.4E-3 - 7.3E-3
X	III	156.6 - 181.3	9.7E-3 - 14.7E-3
X	IV	181.3 - 187.8	14E-3 - 17.6E-3
Y	I	0 - 131.9	0 - 3.7E-3
Y	II	131.9 - 170.8	3.7E-3 - 10.9E-3
Y	III	170.8 - 180.4	10.9E-3 - 14.3E-3
Y	IV	180.4 - 187.8	14.3E-3 - 17.6E-3
45°	I	0 - 158.9	0 - 7.7E-3
45°	II	158.9 - 170.5	7.7E-3 - 10.8E-3
45°	III	170.5 - 180.2	10.8E-3 - 14.2E-3
45°	IV	180.2 - 187.8	14.2E-3 - 17.6E-3
Z	I	0 - 148.5	0 - 5.7E-3
Z	II	148.5 - 173.2	5.7E-3 - 11.6E-3
Z	III	173.2 - 182.2	11.6E-3 - 15.1E-3
Z	IV	182.2 - 187.8	15.1E-3 - 17.6E-3

6.3.3 CWT of AE Signals from Different Deformation Stages

In this study, CWT was used to analyze acoustic emission signals recorded at different stages of deformation (elastic and plastic). CWT is a powerful mathematical tool that allows for the simultaneous analysis of signals in both time and frequency domains, which facilitates the detection and characterization of transient events such as cracks and other damage-related phenomena. Specifically, the elastic and plastic stage AE signals of the four groups of specimens X, Y, Z, and 45° were collected and analyzed in the time-frequency domain using CWT. Interestingly, all elastic and plastic stage AE signals can be categorized based on energy contents. The continuous information obtained from this analysis can be used to describe the behavior of specimen under stress and can aid in the detection and characterization of damage-related phenomena.

Figure 6.4a shows the elastic stage scalogram, while Figure 6.4b shows the same scalogram with added noise. The spectral energy information is located in a frequency band around 200 kHz and 300 kHz, with an amplitude varying from 0.2 to 1.6. Figures 6.5a and 6.5b show the plastic stage scalogram and the same scalogram with added noise, respectively. The scalogram shows that the spectral energy is located in the same frequency band as the elastic stage but with an amplitude varying from 0.005 to 0.35. Some works have also reported the spectral energy content in the same frequency range [214], [215]. However, due to the limited literature available, a deep comparative analysis of spectral energy content is challenging. Thus, CWT

scalogram analysis is a useful tool for detecting and characterizing transient events such as cracks and other damage-related phenomena in stressed materials.

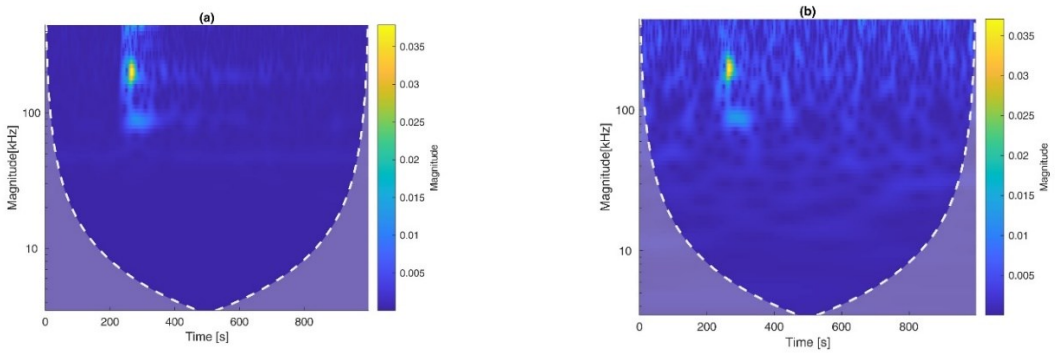

Figure 6.4: (a) Scalogram of Elastic stage, (b) Scalogram of Elastic Stage with Noise

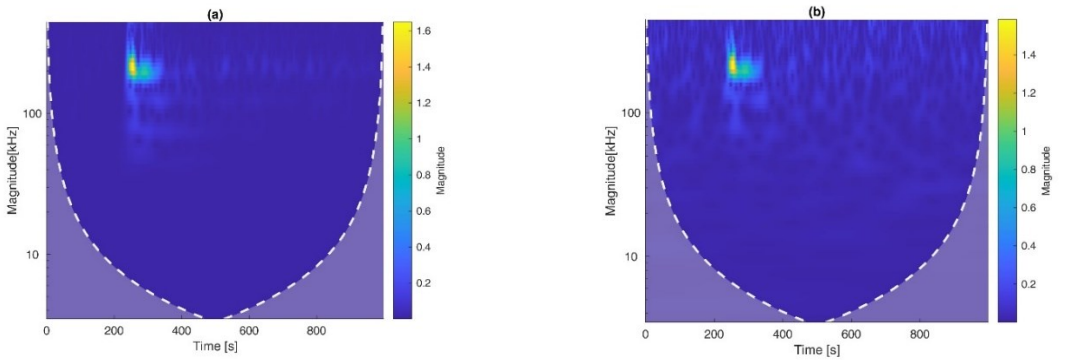

Figure 6.5: (a) Scalogram of Plastic Stage, and (b) Scalogram of Plastic Stage with Noise

6.3.4 FABC-CNN For Damage Mechanisms Characterization and Classification

The previous section discussed the analysis and processing of AE signals obtained during the tensile test using CWT to describe the elastic and plastic behaviour of AlSi10Mg specimens. The scalogram can be considered a 2D image that can be trained by CNNs, and several studies have used CWT with CNNs for damage classification [214], [215], [216]. In this work, the scalograms of the X, Y, Z, and 45° specimens, as well as those of the elastic and plastic stages, are used to train a CNN. The FABC-CNN model, based on FCM and ABC, is used. To improve accuracy and reduce overfitting, a data augmentation strategy based on AWGN (section 2.3) is used. To prepare the dataset, the AE signals of specimens X, Y, Z, and 45 were increased to 4000 at a rate of 1000 signals per class. The elastic and plastic stage AE signals were increased to 20,000 at a rate of 10,000 signals per class. Additionally, the AE signals for the damage modes of the X, Y, Z and 45° specimens were increased to a total of 4,000, with 1,000 signals per class. The FABC-CNN model is built on Matlab 2022a, and the stochastic gradient descent with momentum (SGDM) algorithm is used to train the CNNs. The initial learning rate is set to 0.0001, the maximum number of epochs is 20, and the mini-batch has 120. The cross-validation method is used by dividing the dataset into k = 5 subsets (also known as folds or partitions) and training the network for 5 iterations. In each iteration, (k - 1) subsets are used

as training data, while the remaining subset is used as test data. This process is performed on a laptop computer equipped with an 11th generation Intel (R) Core i7-1195G7 processor with a speed of 2.92 GHz and 16.0 GB of RAM. To measure the classification performance of scalograms of AE signals from AlSi10Mg specimens, the confusion matrix, precision-recall curve, and F1 score are used. First, the scalograms of specimens with respect to the printing direction are trained, and the FABC-CNN algorithm achieved an accuracy of 92.6%, with a precision-recall curve reaching 92.5% and an F1 score of 92.5% (see Figures 6.6, 6.8a and b). The training of the ABC algorithm is presented in Figure 6.7. The classification of AE signals corresponding to the elastic and plastic stages is performed. An effectiveness of 100% is achieved for all metrics using accuracy, precision-recall, and the F1 score (see Figures 6.9, 6.11a and b). The weight optimization by the ABC algorithm is presented in Figure 6.10. Finally, Ultimately, the AE signals corresponding to each zone (as outlined in Section 3.2's damage mechanisms modes) for every specimen were aggregated and classified using FABC-CNN. This algorithm demonstrated a classification accuracy of 90.6% in the confusion matrix (refer to Figure 6.11), achieving a precision-recall curve at 90.4% and an F1 score of 90.5% (refer to Figures 6.12a and 6.12b). The optimization of ABC weights is depicted in Figure 6.13. The results obtained using FABC-CNN provided better performance.

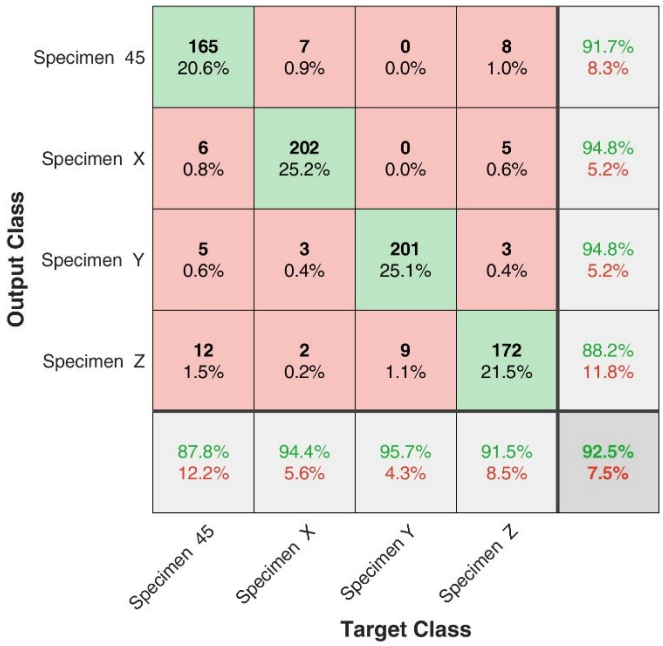

Figure 6.6: Classification based on Scalograms for Printing direction using FABC-CNN.

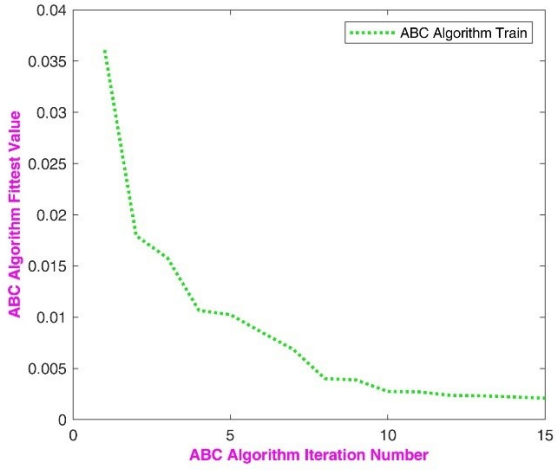

Figure 6.7: Weight optimization using the ABC for Scalograms for Printing direction

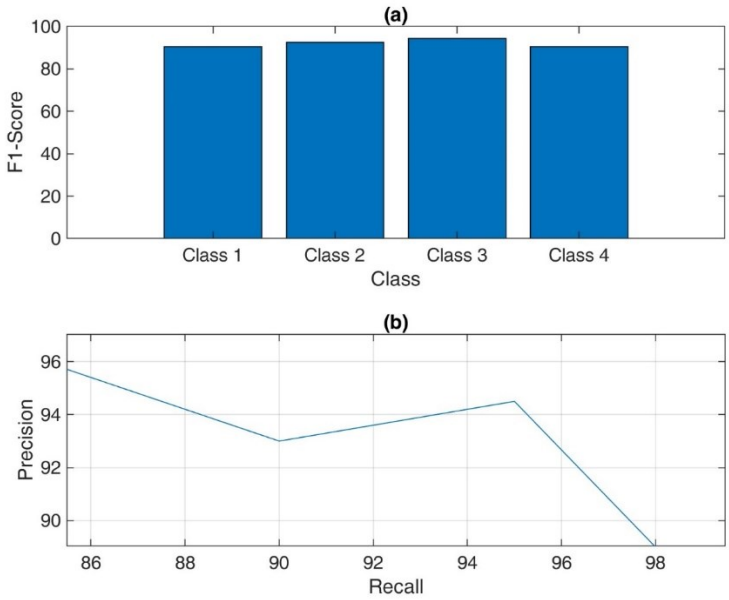

Figure 6.8: (a) F1-Score, and (b) Precision-Recall Curve Scalograms for Printing direction

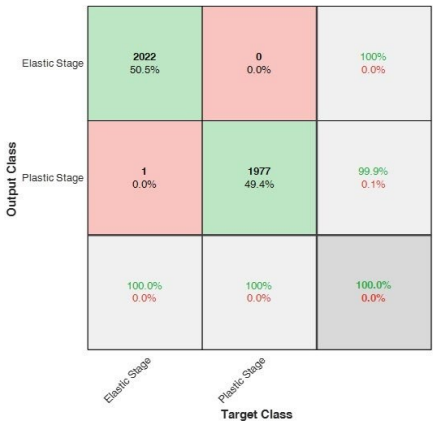

Figure 6.9: Classification based on Scalograms for Deformation Stages using FABC-CNN

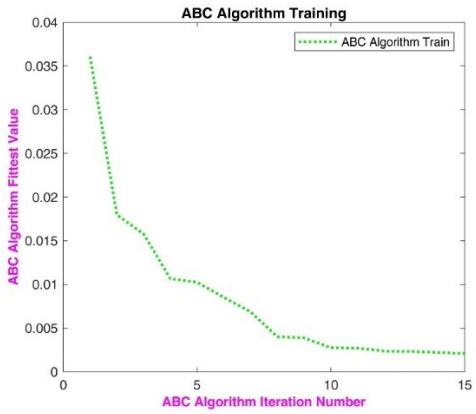

Figure 6.10. Weight optimization using the ABC for Scalograms for Deformation Stages

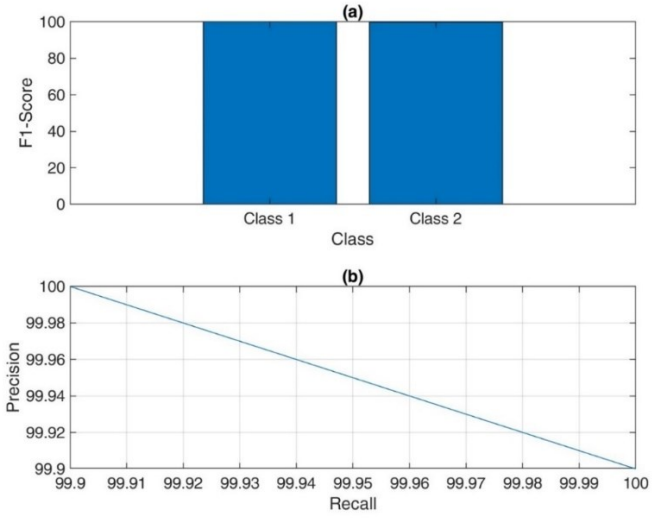

Figure 6.11: (a) F1-Score, and (b) Precision-Recall Curve Scalograms for Deformation Stages

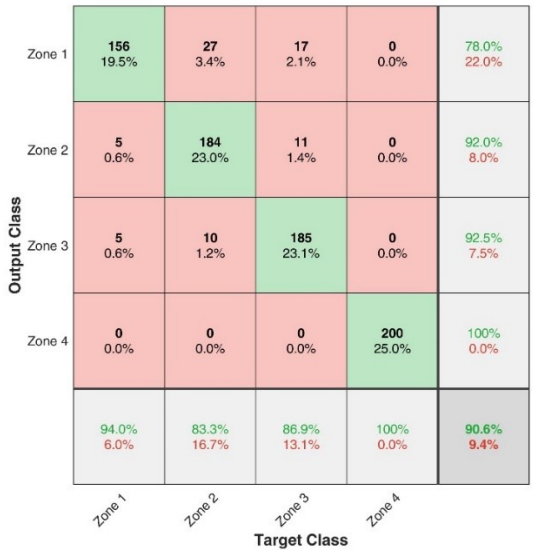

.

Figure 6.11: Classification based on Scalograms for Damage Modes of AlSi10Mg Specimens (X, Y, 45°, and Z) using FABC-CNN

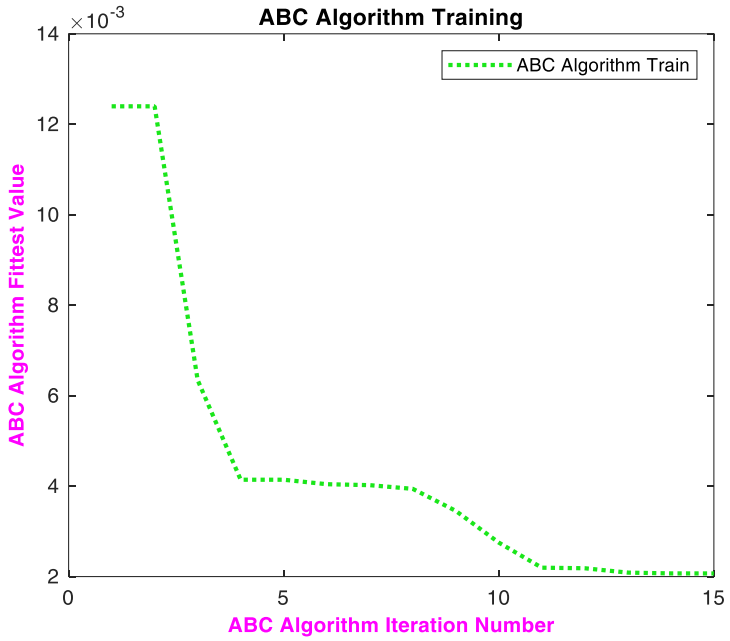

Figure 6.12: Weight optimization using the ABC for Scalograms for Damage Modes of AlSi10Mg Specimens (X, Y, 45°,and Z)

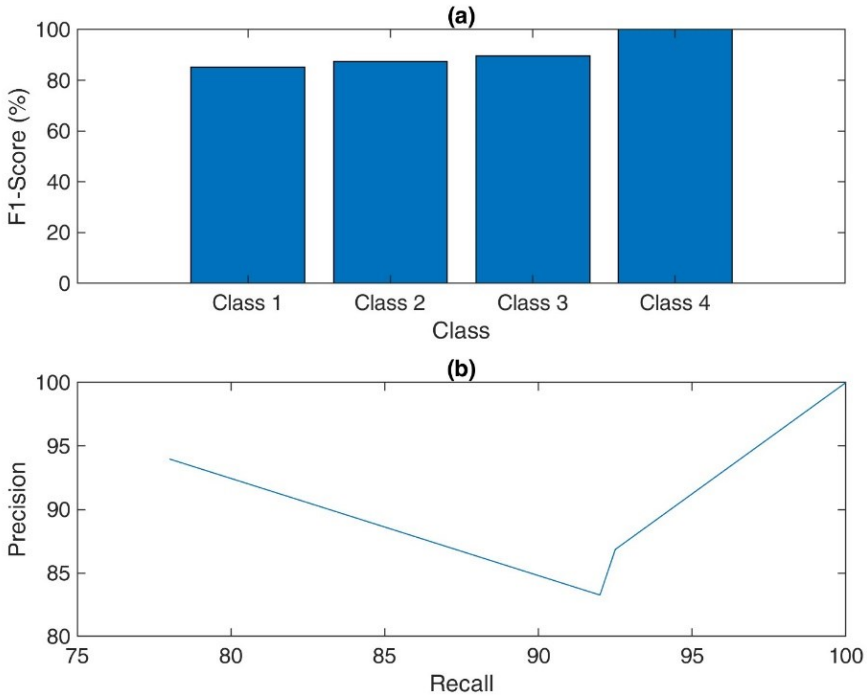

Figure 6.13: (a) F1-Score, and (b) Precision-Recall Curve for Damage Modes of AlSi10Mg specimens (X, Y, 45°,and Z)

6.4 Conclusion

In this chapiter, the mechanical properties of AlSi10Mg specimens were evaluated through a tensile test. The results demonstrate significant variations in yield strength, ultimate tensile strength, and Young's modulus based on the printing direction. This research has enabled a comprehensive assessment of the mechanical behaviour and damage mechanisms of AlSi10Mg

specimens produced by SLM using tensile tests and analysis of AE signals. The investigation began by mapping out damage modes based on the stress-strain curve and cumulative AE energy, effectively identifying four distinct phases of material behavior during deformation. These phases, labelled Zones I through IV, span from the initial elastic response with minimal AE activity, indicative of negligible defect activity, to the ultimate phase preceding material failure, characterized by a significant increase in AE energy signalling large-scale fracturing. The analysis of AE signals based on the CWT scalogram has enabled the distinction between the elastic and plastic stages. To automatically classify the AE signals obtained during the tensile test, a CNN algorithm based on a fuzzy artificial bee colony (FABC-CNN) was utilized. The scalograms of the specimens, oriented according to the printing direction, were analyzed using the FABC-CNN algorithm. This analysis achieved a classification accuracy of 92.6%, with the precision-recall curve and the F1 score both at 92.5%. For the classification of Acoustic Emission (AE) signals, distinguishing between the elastic and plastic phases, the algorithm demonstrated perfect performance, achieving 100% in accuracy, precision-recall, and F1 score. Additionally, in classifying AE signals across different damage modes, the algorithm exhibited high proficiency, with a confusion matrix accuracy of 90.6%, a precision-recall curve of 90.4%, and an F1 score of 90.5%. The outcomes obtained through the FABC-CNN approach proved to be superior. By employing cross-validation, we have demonstrated that our proposed approach, the FABC-CNN, is robust against overfitting and sub-local optimum problems, commonly associated with poor model adaptation to new data. This adaptability to new data enhances the efficiency and reliability of our approach, paving the way for broader applications in the field of material characterization and damage prediction.

Chapter 7. Deep Autoencoder Framework for Damage Characterization in Aerospace CFRP Composites Using AE Technique

This chapter focuses on the challenge of characterizing damage modes in bonded Carbon Fiber Reinforced Plastic (CFRP) composites. Mechanical loading was applied to CFRP samples, during which Acoustic Emission signals were collected to evaluate the material's integrity. A novel analysis approach using a Deep Autoencoder (DAE) was employed to automate the characterization of damage. The DAE reduced the dimensionality of the AE signals, extracting key latent waveform features through Singular Value Decomposition (SVD) to identify damage-sensitive characteristics. These features were then processed using the K-means clustering algorithm to classify distinct damage modes, although the approach faced challenges in fully understanding the physical implications of these damage modes. To overcome this, traditional AE features, such as entropy and amplitude, were also classified using the K-means clustering algorithm, categorizing damage into matrix cracking, delamination, and fiber breakage. Hilbert Spectral Analysis (HSA) was used to further validate these findings, confirming that specific clusters corresponded to distinct damage types. The study compares traditional AE methods with deep learning techniques, highlighting the complexity of identifying damage in loaded CFRP specimens and advocating for a comprehensive analysis to fully understand the behavior of composites under stress.

7.1 Introduction and scope

Carbon fiber reinforced Polymers have gained widespread acclaim due to their exceptional strength-to-weight ratio and design flexibility [217], [218]. This has led to their extensive utilization in various large component structures, including laminates and intricate thin-walled configurations, such as those found in aircraft components and high-pressure cylinder composite layers [219]. In addition to the advantages mentioned above, due to their flexibility in terms of design and manufacture and their light weight, CFRP can be used to create a variety of structures by joining them together using adhesive bonding [205], [220]. The main advantage of adhesive bonded joints is that they have a low impact on the mechanical properties of the adherents, reducing stress concentration and providing better damage tolerance than traditional fixings [221], [222].

The use of bonded joints remains a challenge due to the difficulty of guaranteeing reliability throughout the life of a component [223],[221]. Li et al, found that adhesive shears release stress energy by opening, sliding, and tearing [224]. Joint reliability is particularly delicate under critical fatigue and environmental conditions. All this can lead CFRPs to various damage modes, such as matrix cracking, fiber/matrix debonding and fiber breakage, which have a direct impact on the degradation of mechanical properties and deformation [178], [225].

To address these issues, various strategies are under consideration. These encompass enhancing adhesive mechanical properties, employing finite element analysis for predicting mechanical behavior under extreme loading and support conditions, and implementing non-destructive

testing (NDT) methods [226], [227], [228]. The main aim is to monitor assembly quality, predict damage propagation through adhesives, and identify any damage modes. Acoustic emission (AE) is a prominent non-destructive evaluation method for evaluating damage in composite structures. What sets it apart is its ability to provide an in-depth analysis of damage progression throughout the loading period. Material deformation releases energy in the form of transient elastic waves resulting from micro displacements, providing valuable insights into internal structural changes within a material[229], [230]. Most researchers have presented a variety of methods for exploiting acoustic emission descriptors to effectively characterize damage in bonded CFRP [227], [231], [232], [233], [234], [235], [236]. However, a major challenge lies in the fact that these descriptor-based methods require considerable human expertise to implement successfully.

In the present research work, an experimental study based on the damage mode characteristics of bonded CFRP specimens in a joggled lap shear configuration is carried out. Three specimens (JLS1, JLS2, and JLS3) of the same material and designed in the same configuration are mechanically tested using a tensile test, and the AE signals are measured. The mechanical properties of each specimen are discussed. An innovative approach based on a combination of a deep autoencoder, k-means data clustering and Hilbert spectrum analysis waveform processing to efficiently monitor damage modes in bonded CFRP specimens. This approach eliminates the need for manual extraction of damage-sensitive features from acoustic emission signals.

7.2 Damage Mechanisms Characterization Framework Based on Deep Autoencoder, k-means Clustering and Hilbert Spectrum Analysis

This methodology combines the Deep Autoencoder, K-means clustering, and Hilbert Spectrum Analysis (HHT) to process and characterize AE signals captured during mechanical testing of CFRP composites.

1. AE Signal Acquisition and Preprocessing: AE signals are recorded during tensile tests on CFRP composites, capturing real-time data related to various damage mechanisms such as matrix cracking, fiber breakage, and delamination. Preprocessing is conducted to remove noise and prepare clean data for analysis.
2. Deep Autoencoder for Feature Extraction: The Deep Autoencoder (DAE), as explained in Section 3.2.3, is employed to reduce the dimensionality of the high-dimensional AE data. The autoencoder compresses the data into a latent space that preserves the key damage features, allowing for efficient extraction of the most critical information.
3. K-means Clustering for Damage Classification: The latent features extracted by the autoencoder are then classified using K-means clustering, as detailed in Subsection 3.2.1.1. This clustering method groups similar AE signals into clusters that correspond to different damage modes, enabling accurate classification of damage mechanisms modes.

4. Hilbert Spectrum Analysis (HHT): To refine the classification, Hilbert Spectrum Analysis, described in Subsection 3.1.3.2, is applied to the AE signals. HHT provides a detailed time-frequency representation, which helps in identifying subtle variations between damage mechanisms by analyzing the energy distribution over time.

This integrated framework allows for accurate characterization of damage mechanisms in CFRP composites, offering a robust method for identifying and tracking damage progression. In the next section, the results and discussion of this characterization approach will be presented.

7.3 Materials and Testing Methods

To prepare the CFRP laminates, an epoxy-carbon fiber prepreg, ER450 epoxy (SAATI CIT CC206 ER450 43%) was taken. The reinforcing carbon fibers are arranged in a woven configuration, with layers of fibers overlapping one another. The adherends were cured using autoclave method. Detailed specifications, including the number of plies and adherend geometry, can be found in Table 1. The nominal ply thickness is 0.244 mm. The adherends are joined together in a Joggled Lap Shear (JLS) configuration using a strong structural adhesive. The adhesive chosen for this study is characterized by a shear strength of 25 MPa and a peel strength of 65 MPa. Details about the adhesive coated thickness and the overlapping area are also provided in Table 7.1. The adhesive was cured at a temperature of 65 °C for 1 hour, followed by testing after a 5-day interval. The JLS bonded laminates are depicted in Figure 7.1 While no standardized procedure is available to determine the ply thickness and number of plies for the specimen configuration, the testing procedures were carried out in accordance with ASTMD5068 standards. Three specimens of same category, named as JLS1, JLS2 and JLS3, were analyzed in this study. All the tests were carried out under the same test conditions.

Table 7.1. Description of Geometry and Properties for JLS Specimens

Flat Adherend				
Length (mm)	**Width (mm)**	**Thickness (mm)**	**No. of Plies**	**Stacking sequence**
101.6±0.12	26.09±0.07	2.0±0.04	8	$[+45/-45]_3/-45/+45$
Curved Adherend				
Length (mm)	**Width (mm)**	**Thickness (mm)**	**No. of Plies**	**Stacking sequence**
101.6±0.17	26.09±0.05	2.0±0.04	6	$[+45/-45]_3/-45/+45$
Overlapping Region (Adhesive)				
Length (mm)		**Width (mm)**		**Thickness (mm)**
101.6±0.17		2.0±0.04		3.67±0.05

Figure 7.1: Typical JLS specimen.

7.4 Results and discussion

7.4.1 Mechanical Test Results

The mechanical characterization of the damage modes of JLS specimens was carried out through a series of tensile tests, following the recommendations of ASTM D5868 standard. Two critical points can be identified from the mechanical results presented in Figure 4: the maximum load at initial failure, which indicates the onset of damage, and the maximum load at final failure, which represents the complete failure of the specimen. Although the three specimens share similar material characteristics, their peak load values differ significantly. This finding has been observed by several authors on the bonded specimen, such as Avila et al., Liu et al. Adin et al. and Kadioglu et al. [37 - 40]. This variation can be attributed to a series of factors such as overlap length, adhesive thickness and scarf angle.

These researchers unanimously recognized the significant impact of these factors on the performance of joined composites under static stress. Adin et al revealed that modifying joint dimensions could reduce maximum stress [39]. Meanwhile, Silva et al. observed that the use of hand-mixed adhesives in CFRP composites could introduce geometric variations in the bonded areas, affecting their load-bearing capacity. They also noted the importance of surface treatment, temperature, and exposure to hostile environments, highlighting their effect on load performance [41]. Manohar et al. highlighted that the choice of adhesive and bonding agent, overlap length and pre-treatment methods influence joint strength [42]. Kowatz et al. discussed that the reduced shear strength in composite structures is attributed to the uneven shear stress distribution and found less resilience to fatigue under repeated loading [43]. Lu et al. explored the effect of the number of CFRP layers and bonding mode on the mechanical properties of composites [44, 45]. One of their works reported an improvement in load-bearing capacity and stiffness with an increase in the number of layers [45], while the other found that the double-sided reinforcement was effective [44]. Karachalios et al. found that the adhesive thickness strongly affects joint strength, with thicker adhesives giving stronger joints [46]. Martínez et al. concluded that the shear stress in single-lap joints is mainly affected by the thickness of the adhesive [47], while the deformation, elastic modulus and absorbed energy are influenced by the overlap length [47]. In summary, these studies demonstrate that variation in the mechanical properties in bonded composites can be attributed to the following factors: interface strength, adhesive thickness, presence of defects and bonding method. In addition, they collectively highlight the complex interplay of these factors that could lead to the variations in the failure loads. The JLS 1 specimen withstood a considerably higher initial load than the JLS 2 and JLS

3 specimens. In particular, specimen JLS 2 showed low resistance to initial and final fracture (see Figures 7.2a, b and c).

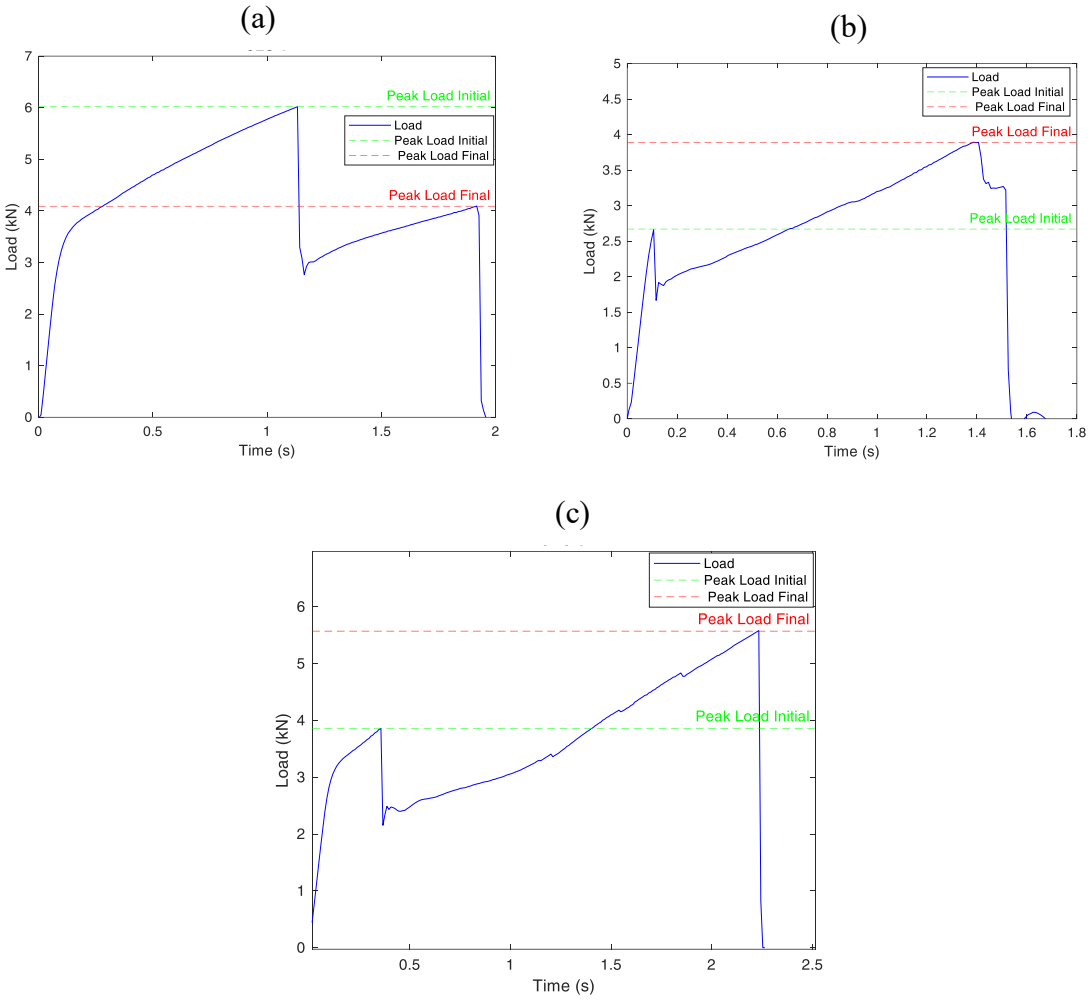

Figure 7.2: (a) Mechanical properties of JLS1 specimen, (b) Mechanical properties of JLS2 specimen, (c) Mechanical properties of JLS3 specimen

7.4.2 Results of deep autoencoder training

The AE signals acquired from the mechanical testing of the bonded composites are used to train the DAE model. During the training phase, the DAE is engaged in accurately reconstructing the AE's input signals. AE signals collected from JLS1, JLS2, and JLS3, each containing waveforms of length 5120 samples, were used to train and evaluate the model. The dataset contains 715 waveforms from JLS1, 393 waveforms from JLS2, and 827 waveforms from JLS3. During the training process, the DAE reduced the dimension of the waveform into a low-dimensional space of four latent features at the bottleneck layer through the encoder. Then it is decoded using the trained weights in the decoder layers to restore it to its original state. The k-fold cross-validation is used to improve training and validation by dividing the dataset into k=4 subsets (or "folds"). At each training iteration, k-1 datasets are used for training, while one remaining dataset is reserved for validation. This approach aims to reduce bias by using the majority of data for training in all k iterations. This process is performed on a PC with a speed of 2.92 GHz and a RAM of 16.0 GB.

The hyperparameters for this DAE training were designed to optimize the model's performance. To achieve a balance between model convergence and the prevention of overfitting, training is continued for 150 epochs. The mini-batch size of 128 improves the efficiency of the computation and the stability of the gradient. Data shuffling is included at the start of each epoch, which maintains diversity within the mini batches. Validation is repeated for every 10 mini-batches. A learning rate of 0.001 is used to ensure smooth convergence. To enhance the learning process, a piecewise learning rate schedule is implemented, which reduces the learning rate by a factor of 0.7 every 20 epochs (refer to Table 7.2). Figures 7.3 (a), (b), and (c) each illustrate an example of an original signal and its reconstructed signal from specimens JSL1, JSL2, and JSL3, respectively. The reconstruction error for each parametric study case was measured by root-mean-square error (RMSE) to assess the respective performance (see Figure 7.4). For JSL1, the average RMSE is around 0.170045. For JSL2, the average RMSE error is around 1.107225. Finally, for JSL3, the mean RMSE error is around 0.671855. The main objective was to extract latent features that represent high-dimensional input data containing information about the fracture mechanism of specimens under load and reduce them to low-dimensional features retaining the same information. To ensure efficiency, it is essential that the RMSE error is low, indicating that the model can reconstruct the data accurately, closely reflecting the original input. It should be noted that in some cases, DAE is also used to reduce noise in the data [237].

Table 7.2. Training parameters of the deep autoencoder model

Training Parameters	
Max number of training epochs	150
Mini batch	128
Validation Frequency	10
Initial Learn Rate	0.001
Learn Rate Schedule	piecewise
Drop factor	20
Drop learning	0.7
Gradient Threshold	1
L2 Regularization	0.001

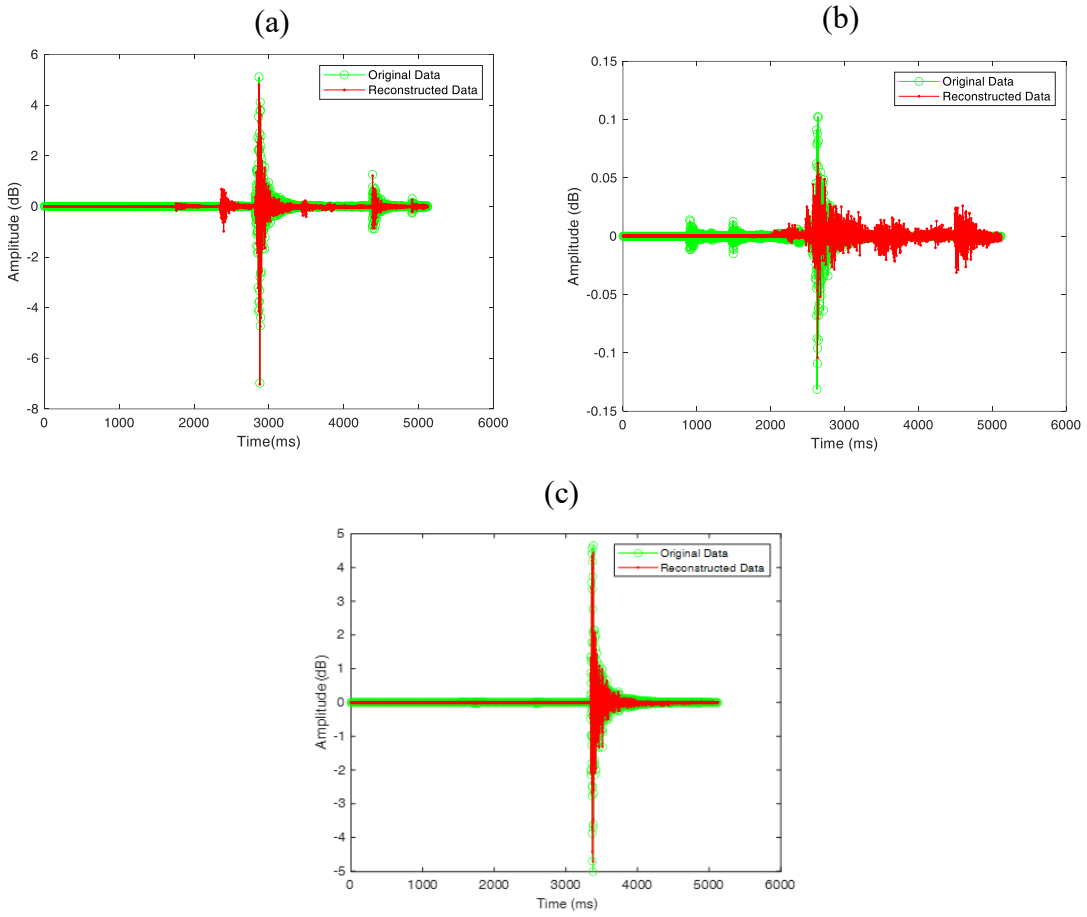

Figure 7.3: Original and reconstructed signal based on Deep Autoencoder for JLS 1; JLS 2; and JLS3

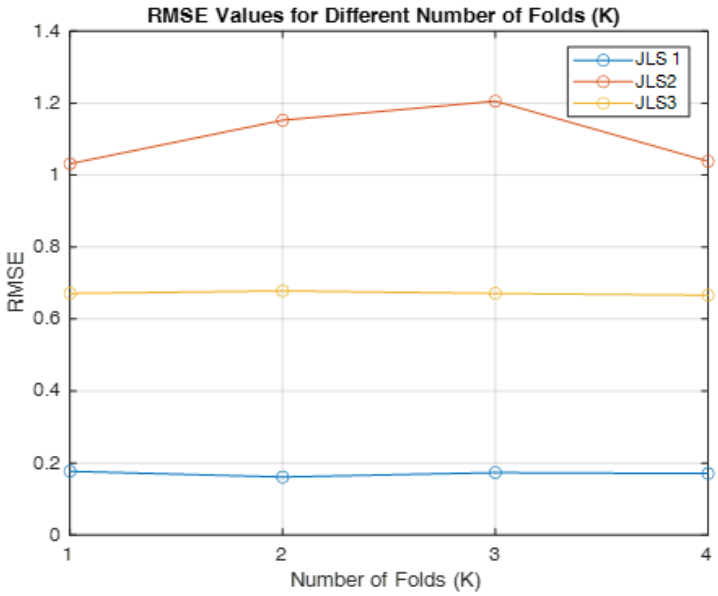

Figure 7.4: Effect of cross-validation folds (K) on RMSE values for different specimen types

7.4.2.1 Damage characterization using latent features

The latent features from the bottleneck layer are used for damage clustering. The Singular Value Decomposition (SVD) method is used to select the most significant latent features reflecting the original signal data. Figure 7.5(a) shows that the dominant singular value is two,

representing 96% of the variance explained for JLS1 specimens., 94% for JLS2 (see Figure 7.5(b)), and 92% for JLS3 (see Figure 7(c)). (See Figure 7 (c)).

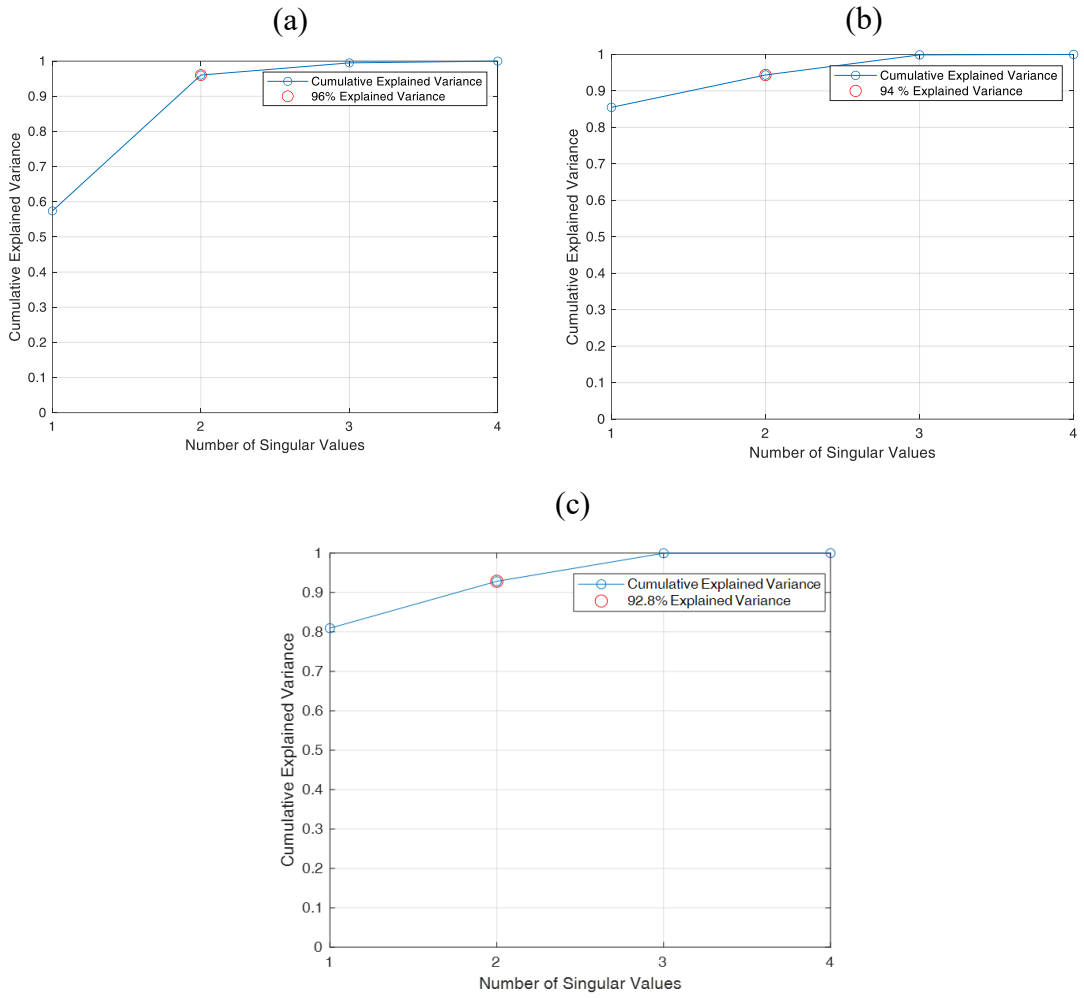

Figure 7.5: Selection of dominant features from the bottleneck layer by SVD: (a) JLS1, (b) JLS2, and (c) JLS3.

The unsupervised k-means pattern recognition algorithm was employed to examine the selected latent features. In this context, the Silhouette criterion is used to assess cluster quality by comparing the similarity of an object within its own cluster against its similarity to the objects in other clusters. A higher Silhouette score is indicative of a model characterized by well-delineated clusters. The Silhouette criterion returns k = 3 as the optimal number of clusters (see Figure 7.6 (a), (b), and (c)). This finding implies that the three-cluster model contains significant intra-cluster homogeneity and distinct inter-cluster separation and, therefore, is capable of elucidating the inherent structure of the dataset.

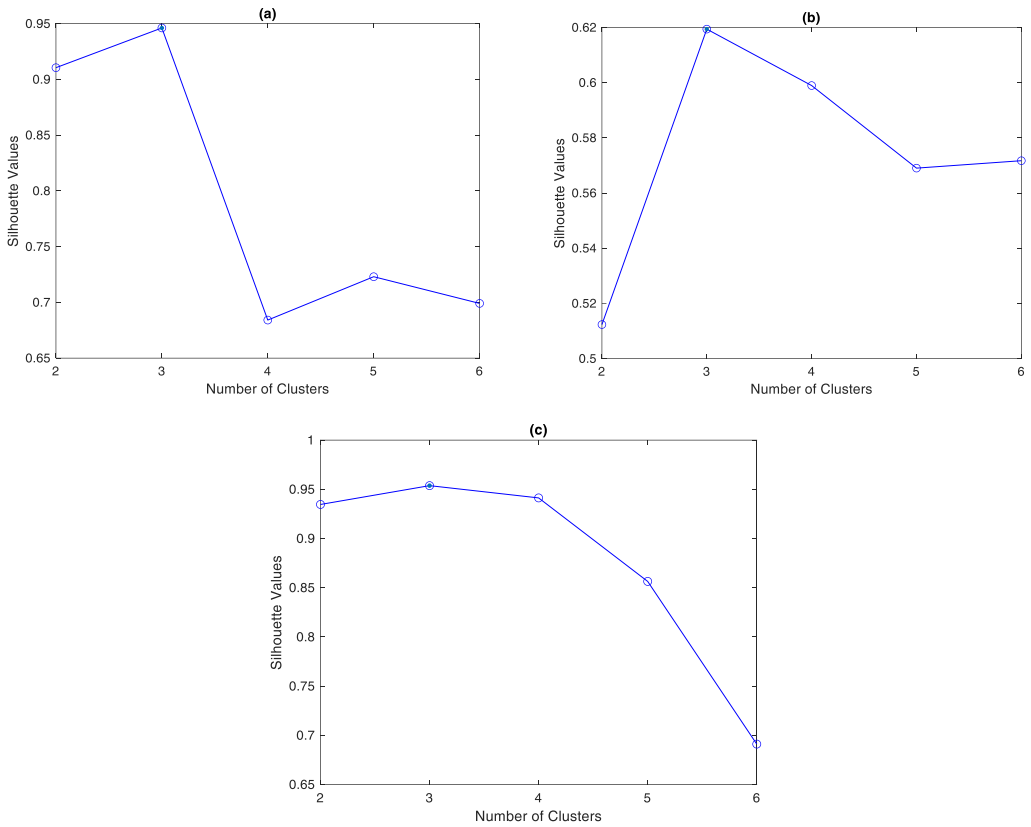

Figure 7.6: Silhouette values of clusters for latent features of: (a) JLS1, (b) JLS2, and (c) JLS3

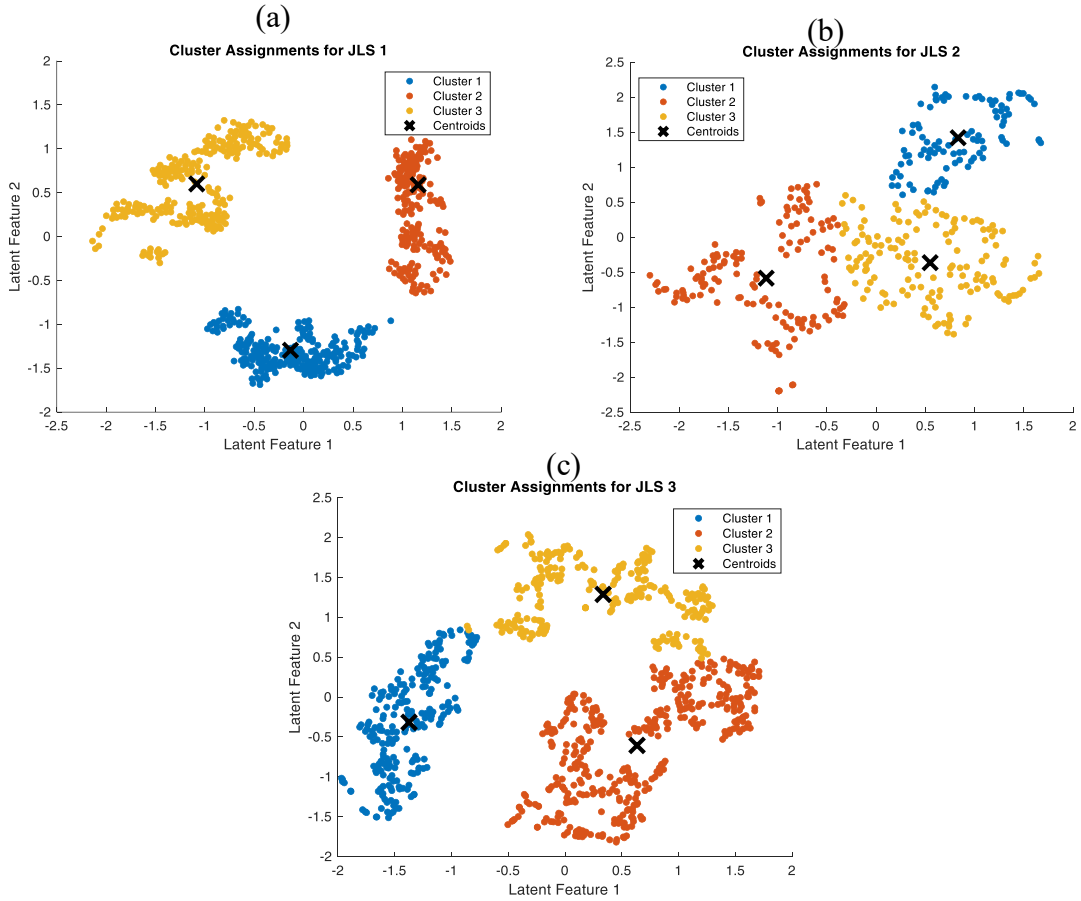

Figure 7.7: Latent feature clustered by k-means algorithm for : (a) JLS1, (b) JLS2, and (c) JLS3

Figures 7.7 (a), (b), and (c) illustrate each latent feature clustered from specimens JLS1, JLS2, and JLS3, respectively. The three distinct clusters of latent features reflect different damage modes observed during mechanical testing.

Recent studies have applied various forms of autoencoders, including deep convolutional, variational, and stacked autoencoders, for damage detection in different materials [238], [239]. The methods have demonstrated improvements in the automated detection and classification of damage mechanisms. Despite these advances, the relationship between latent features and specific damage modes remains unexplored. This represents a significant gap that limits our in-depth understanding of damage mechanisms. To address this limitation, the model proposes analyzing the AE waveforms corresponding to the clustered data points. These analyses are carried out on the corresponding signals reconstructed by the decoder. Therefore, a frequency-domain analysis based on the power spectral density of the waveforms is performed. The objective is to accurately identify the frequency characteristics responsible for damage modes in bonded composite specimens.

All waveforms analyzed were randomly selected to ensure a balanced representation of the data for analysis. The examination of the JLS 1 specimen, illustrated in Figure 7.8, reveals a distinct variety of frequencies within Cluster 1 that extend from 100 to 375 kHz. They also show frequency fluctuations, particularly from 300 to 375 kHz, where increased spectral power is observed. In Cluster 2, spectral power is distributed over the frequency range of 250–375 kHz. A distinct peak in spectral power is identified at 350 kHz. Cluster 3 shows relatively less variability, with the dominant spectral band around 300–400 kHz and a peak frequency at 350 kHz.

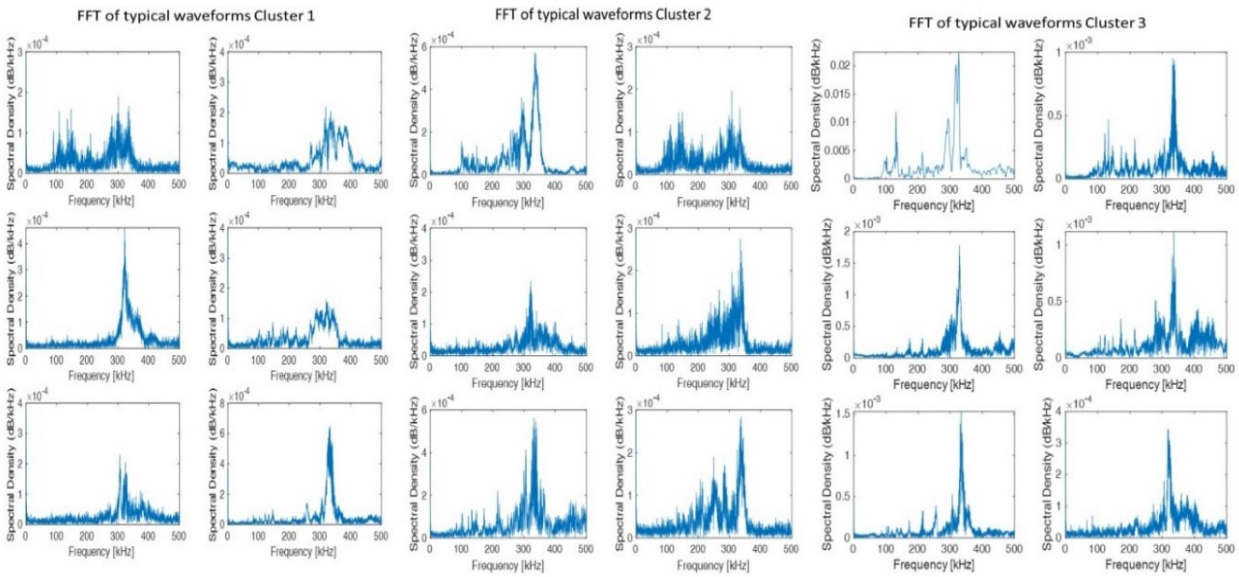

Figure 7.8: Typical AE frequency - domain waveforms from JLS 1: Cluster 1; Cluster 2; and Cluster 3 based on latent feature

The frequency analysis of the AE signals from the JLS 2 is shown in Figure 7.9. The results show increased complexity, with each cluster exhibiting a spectral power distribution in distinct frequency ranges. However, a peak around 350 kHz is observed in all clusters, highlighting a common feature despite the spectral diversity. This observation reiterates the phenomenon identified in the first specimen, where a spectral power peak was also located at this same

frequency. Three frequency spectra were identified in the cluster 1: the first spectrum is located between 100-250 kHz, the second extends from 300-375 kHz, and the third is positioned in the 400 to 500 kHz range. The cluster 2 waveforms are characterized by two distinct frequency spectra: the first spectrum from 100-250 kHz and the second from 300-375 kHz. Cluster 3 features a frequency spectrum covering 250-350 kHz.

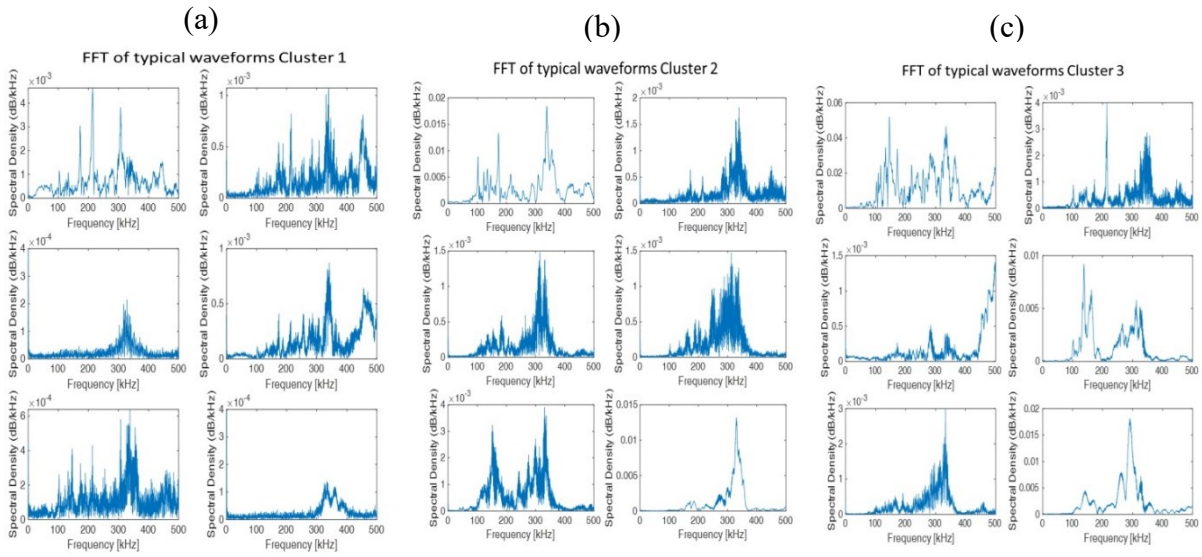

Figure 7.9: Typical AE frequency - domain waveforms from JLS 2: (a) Cluster 1; (b) Cluster 2; and (c) Cluster 3 based on latent feature

In the case of specimen JLS 3, illustrated in Figure 7.10, Cluster 1 shows dominant frequencies between 300-350 kHz, accompanied by some additional frequencies that vary with each waveform. Nevertheless, some peaks are identified in the first spectra between 100 and 200 kHz, with a main peak at 350 kHz, similar to observations made for JLS specimens 1 and 2. This recurrence of the 350 kHz peak establishes a consistent frequency pattern across the specimens studied. In cluster 2, waveforms show frequencies predominantly between 275 and 375 kHz, indicating a common dominant spectral band within this cluster. The same observation is made for cluster 3, although spectral lines are also detected as small peaks in the first spectrum between 100 and 200 kHz, adding further nuance to the spectral analysis of this cluster. However, the most dominant frequency is around 250–375 kHz.

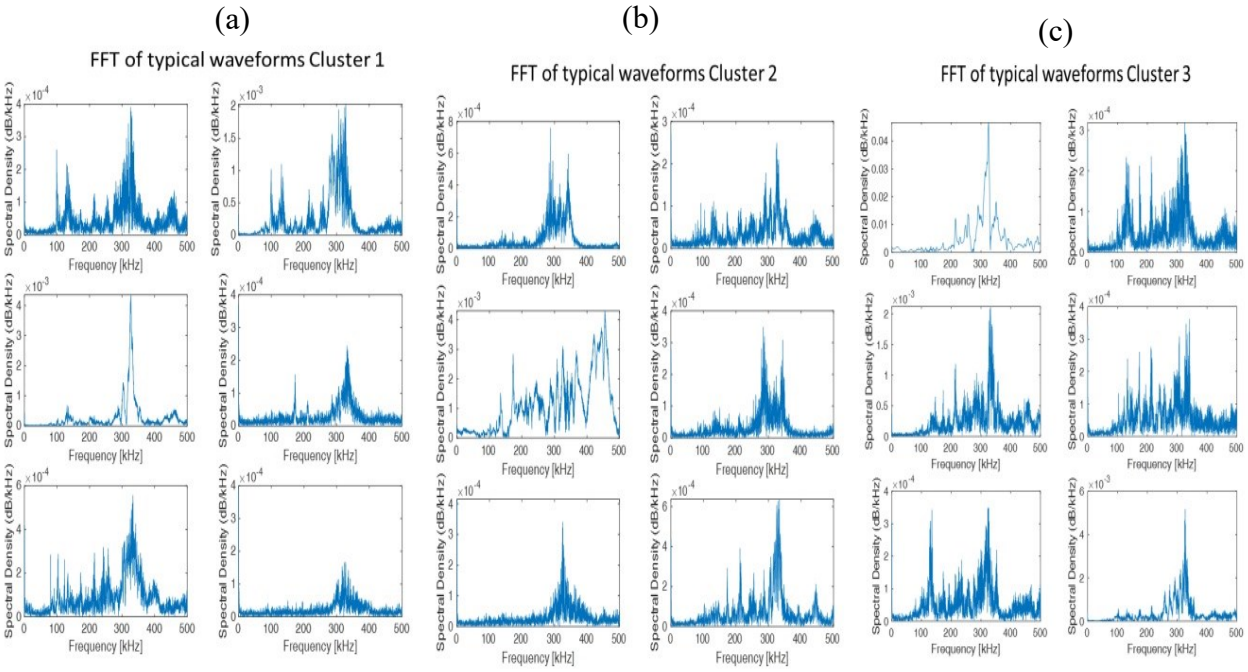

Figure 7.10: Typical AE frequency - domain waveforms form JLS 3: (a) Cluster 1; (b) Cluster 2; and (c) Cluster 3 based on latent feature

The analysis reveals variability in the overall frequency content as well as the presence of dominant frequency bands across clusters. Bearing this complexity in mind, the aim is to correlate each cluster with a specific damage mode across all tested joggled lap CFRP specimens under tensile loads. In certain clusters, AE signals with frequency bands between 100-250 kHz and 100-200 kHz were observed. De Groot et al. have similarly associated these frequency ranges with matrix cracking [240], since it produces low-frequency signals. This is confirmed by the results of this study on the JLS composites and by various other studies. In our recent study, frequency analysis of AE signals revealed two frequency bands characteristic of delamination processes: one between 150 and 250 kHz, and the other above 300 kHz [241]. Similar frequency bands were observed in the JLS composites, which could be associated with delamination. The frequency bands of 250–350 kHz and 250–375 kHz are generally considered to be indicative of matrix/ fiber debonding [53, 54]. The predominant frequency band for a large number of signals in each JLS specimen was centered around 250–375 kHz. This observation suggests that the load was transported inside the adhesive layer. The evolution of interfacial crack growth in this same zone influenced the generation of acoustic events. The 400–500 kHz frequency band is linked to fiber breakage or the development of interlaminar cracks in CFRP composites [242]. Recent studies and our previous research have confirmed this observation [108]. In this analysis based on AE waveforms, it has been observed that the main damage modes in all JLS specifications are matrix/fiber debonding and interfacial crack growth. Some research has validated the frequencies of AE signals associated with different damage modes using Digital Image Correlation (DIC) or other supplementary analysis.

Andraju and Raju identified micro/macro matrix damage (58–175 kHz), fiber-matrix debonding (175–400 kHz), delamination and fiber pullout/peel-off (400–600 kHz), and fiber failure (>600 kHz) in CFRP laminates [243]. Mahesh et al. identified matrix cracking (100–260 kHz) and interface failure (270–400 kHz) in open-hole CFRP laminates under tension-

shear loading [244]. Ali et al. identified matrix cracking (50–180 kHz), interface failure (180-400 kHz), and fiber breakage (400–670 kHz) in woven carbon fabric laminates and effectively classified the damage modes under flexural loading [245]. Zarouchas and Hemelrijck characterized thick adhesives in wind turbine blades through tensile and compression tests on dogbone specimens and bonded joints. Using DIC, they identified microcracks (80–110 kHz), matrix macrocracks (210–280 kHz), and fiber rupture (410–480 kHz). The frequency bands observed from our analysis and referenced studies establish a consistent correlation between specific frequency ranges and particular damage modes. Matrix cracking generally occurs between 50 and 260 kHz; fiber-matrix debonding and delamination between 175 and 400 kHz; and fiber breakage (>600 kHz).

7.4.3 Damage characterization using AE features

The second part of the damage characterization uses AE descriptors, the amplitude and entropy. The Amplitude and entropy of the AE signals from the JLS specimens are clustered using the k-means algorithm. These features are often used to effectively characterize materials, include CFRP composites subjected to mechanical loading [241]. In the context of our study, the choice of amplitude and entropy descriptors for AE signal analysis is dictated by their ability to provide distinct and complementary insights into the dynamics of failure events [246]. The entropy characterizes the uncertainty or disorder of the signal data, thereby enabling a qualitative analysis of failure structures. Recently, several key studies have demonstrated the effectiveness of entropy in AE analysis. For example, Burud et al. have demonstrated that wavelet entropy can effectively estimate spectral disorder in AE signals, providing valuable information on fracture processes in concrete [247]. The use of entropy and amplitude thus enriches our understanding of failure mechanisms. The integration of these two measures significantly enhances the ability to distinguish between different types of damage, facilitating the characterization and classification of failure modes in the CFRP composites. As explained in the previous subsection, the Silhouette criterion is applied to determine the optimal number of clusters. Figures 7.11 (a), (b) and (c) show that there are three optimal clusters for the features and for all specimens.

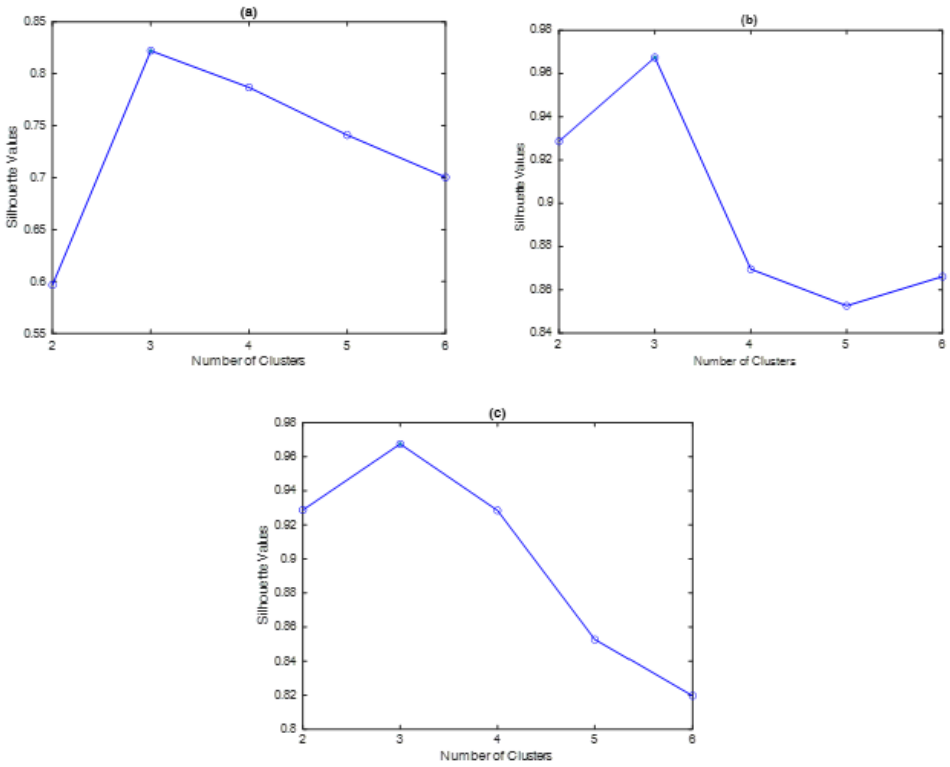

Figure 7.11: Silhouette Values of AE Features of (a) JSL1; (b) JLS 2; and (c) JLS3

In Figure 7.12 and Table 4, cluster assignments for specimens JLS1, JLS2, and JLS3 are presented. For specimen JLS1, the first cluster exhibits a low amplitude range of 40 to 48 dB and an entropy distribution from 0.01 to 1.54, indicating initial damage such as microcracks. Cluster 2, with an amplitude range of 49 to 65 dB and entropy from 0.02 to 1.01, suggests damage progression, with signs of interlaminar cracks. The third cluster, spanning 67 to 99 dB in amplitude and 0.03 to 0.8 in entropy, reveals severe damage, possibly indicating the critical failure. The specimen JLS2 exhibits damage beginning with a first cluster ranging from 40 to 58 dB in amplitude and 0.03 to 2.10 in entropy, suggesting a more varied initiation of damage, potentially due to debonding or microcracking. The second cluster, displaying an amplitude of 59 to 78 dB and an entropy of 0.02 to 1.35, indicates a progression towards moderate damage. The third cluster, from 79 to 100 dB in amplitude and 0.07 to 1.03 in entropy, denotes critical damage, with a strong indication of fiber breakages, signalling an advanced stage of structural degradation. For JLS3, the first cluster reveals an amplitude of 40 to 53 dB and an entropy distribution of 0.01 to 2.59, highlighting a wide range of initial damages, from minor debonding to various microcracks. The second cluster, with an amplitude of 54 to 75 dB and an entropy of 0.02 to 1.88, shows signs of more serious damage, likely more complex and extensive matrix cracking. Finally, the third cluster, with amplitudes of 76 to 100 dB and an entropy of 0.04 to 1.52, signals very severe damage, such as fiber ruptures, indicating the most critical phase of degradation. The initial observation is that there are three modes of damage for each specimen, each with a slightly different distribution. This variation can be attributed to the fact that the adhesive used for these specimens was applied manually. Liu et al. identified acoustic emission amplitudes for matrix cracking as 50–60 dB, delamination, 60–80 dB, interface failure, 50–70 dB, and fiber breakage, 80–90 dB in fiber reinforced composites [248]. Zhuang and Yan's study

on polyethylene composites reported similar amplitudes: matrix cracking below 60 dB, delamination 60–85 dB, interface failure 30–45 dB, and fiber breakage 80–97 dB [249]. Barre and Benzeggagh found in glass/polypropylene composites amplitudes of 40–55 dB for matrix cracking, 65–85 dB for delamination, 60–65 dB for interface failure, and 85–95 dB for fiber breakage [250]. Based on these observations, a hypothesis can be formulated. In Table 7.3, the clustered AE feature entropy versus amplitude may indicate different damage processes. Cluster 1 represents AE signals generated by matrix cracking; cluster 2 represents signals from delamination events; and cluster 3 represents signals from fiber breakage.

In this study, time-frequency analysis based on HSA is used to support this hypothesis. Previous research has identified CFRP specimen damage modes based on frequency range and the instantaneous energy of AE waveforms [251].

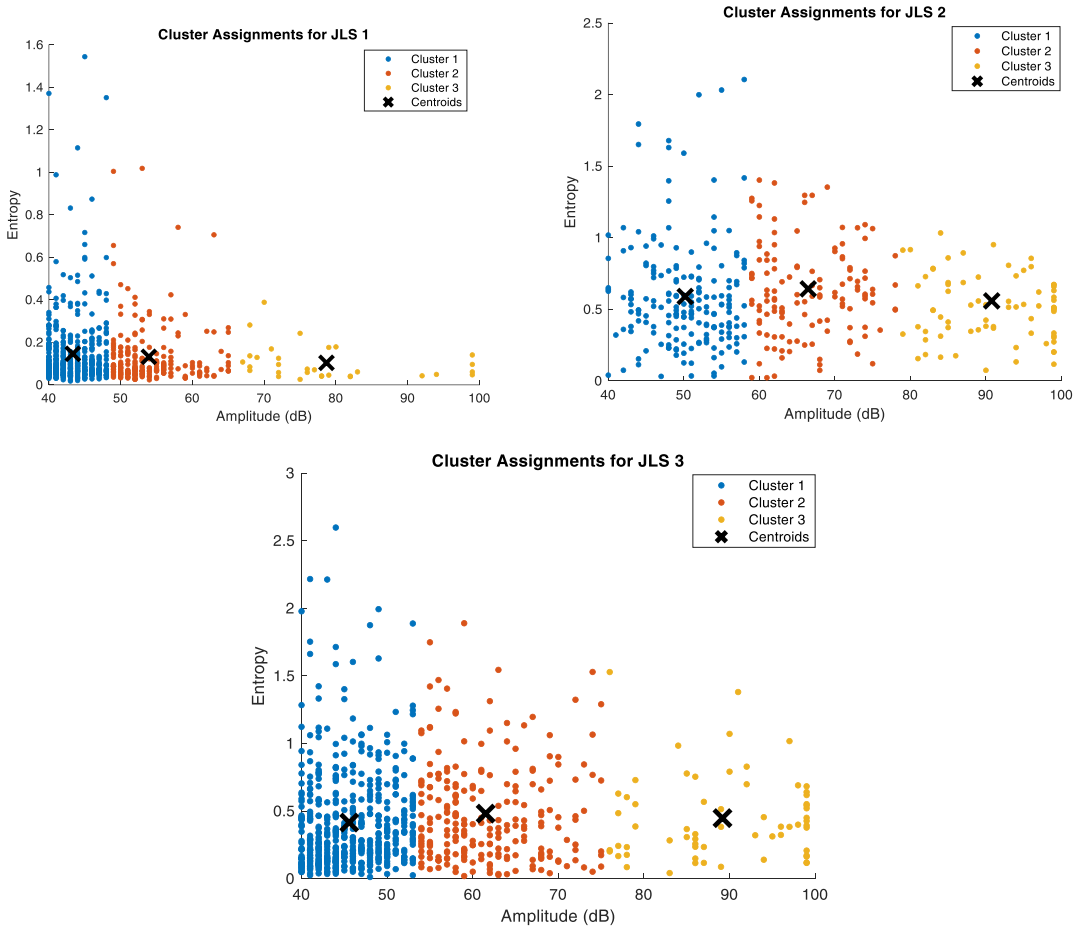

Figure 7.12: Cluster assignments between Amplitude and Entropy for Specimens: JLS1; JLS2; and JLS3

Table 7.3. Entropy and Amplitude Cluster Ranges Across all Specimens.

Specimen	Cluster entropy ranges			Cluster amplitude ranges (dB)		
	Cluster 1	Cluster 2	Cluster 3	Cluster 1	Cluster 2	Cluster 3
JLS 1	0.01 - 1.54	0.02 - 1.01	0.03 - 0.8	40 - 48	49 - 65	67 - 100
JLS 2	0.03 - 2.10	0.02 - 1.35	0.07 - 1.03	40 - 58	59 - 78	79 - 100
JLS 3	0.01 - 2.59	0.02 - 1.88	0.04 - 1.52	40 - 53	54 -75	76 - 100

In this subsection, the Fourier transform is applied in order to facilitate the visualization of the waveforms associated with each typical cluster for all the specimens examined. Complementarily, the analysis relies on Hilbert spectral analysis for further exploration. At random, AE signals are extracted for each cluster and specimen for detailed analysis.

Figures 7.13, 7.14, and 7.15 display the frequency analysis of specimens JLS1, JLS2, and JLS3, respectively. They highlight the frequency characteristics specific to each cluster. An initial observation indicates a homogeneity of frequencies within the clusters. This uniformity contrasts with analyses based on latent characteristics conducted previously. This finding highlights the limitations of the proposed DAE-based methodology.

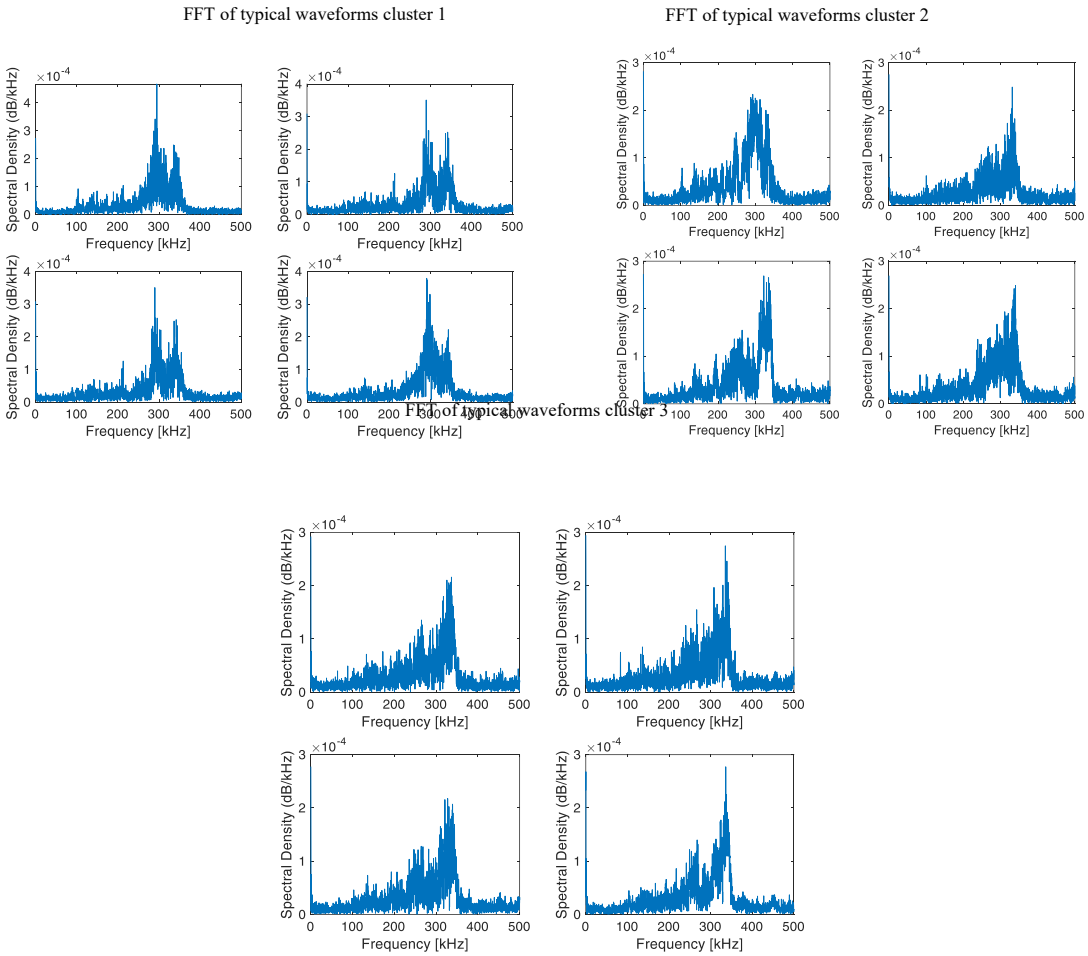

Figure 7.13: Typical AE frequency - domain waveforms from JLS 1: Cluster 1; Cluster 2; and Cluster 3 based on AE features

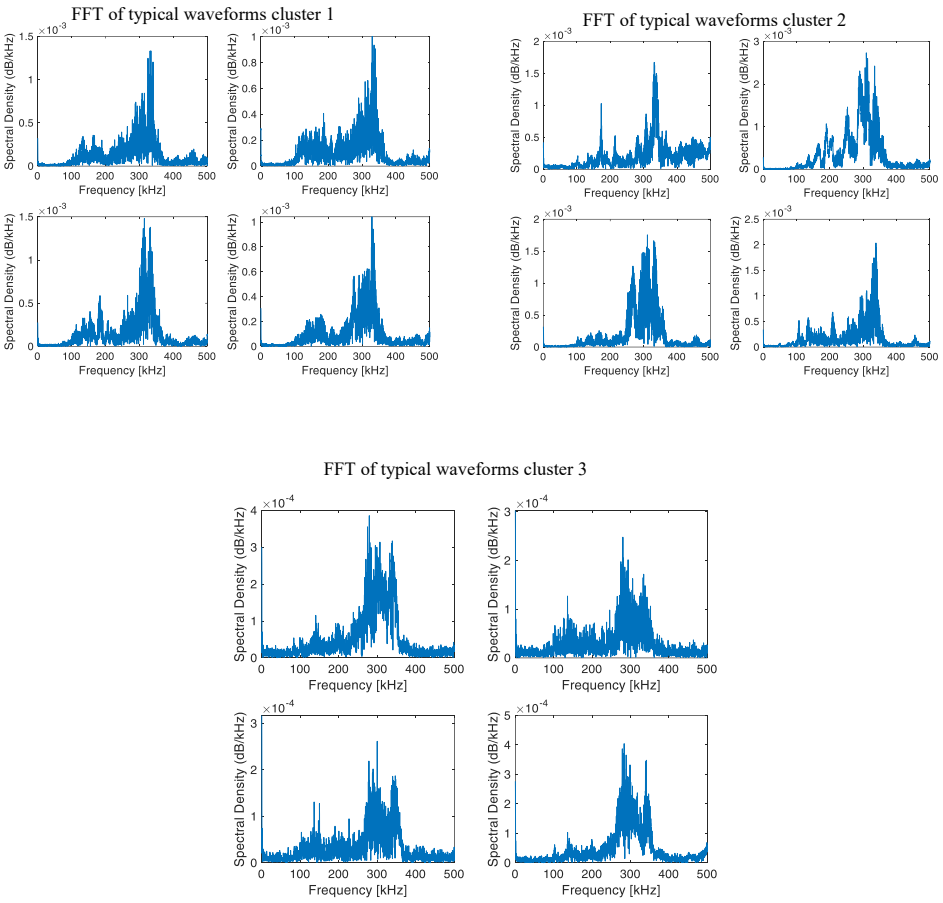

Figure 7.14: Typical AE frequency - domain waveforms from JLS 2: Cluster 1; Cluster 2; and Cluster 3 based on AE features

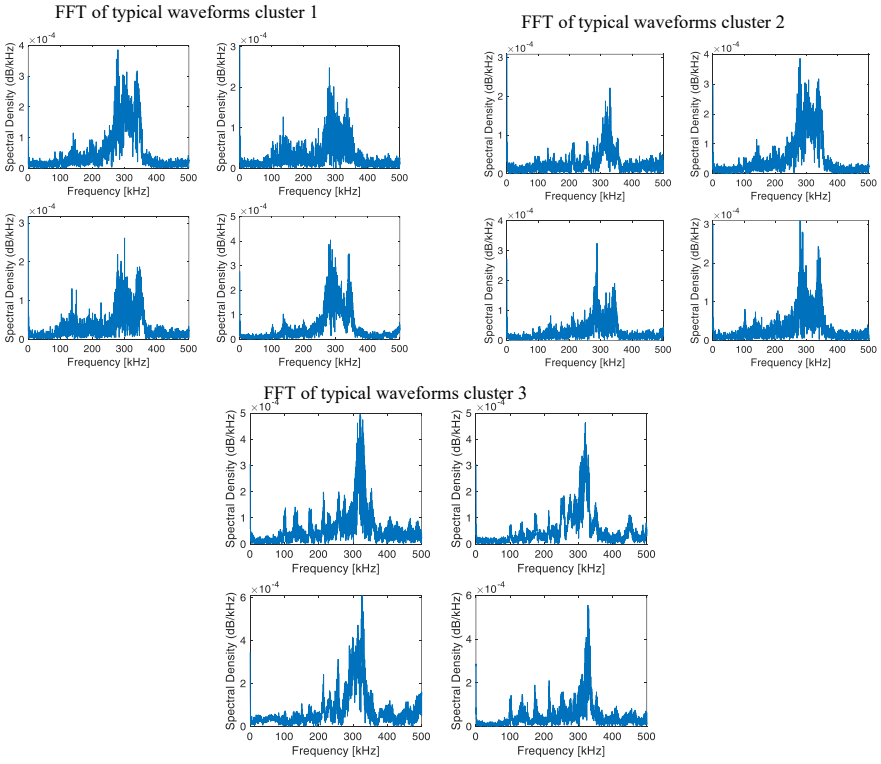

Figure 7.15: Typical AE frequency - domain waveforms from JLS 3: Cluster 1; Cluster 2; and Cluster 3 based on AE features

As mentioned earlier, HSA is used as a signal processing technique to extract relevant characteristics from AE waveforms [69]. For the first HAS of JLS 1 specimen, the instantaneous energy is concentrated between 250 and 375 kHz at 2 ms (See Figure 7.16(a)). For the second HSA, it is focused between 300 and 350 kHz at the same 2 ms mark (see Figure 7.16(b)). The third HSA exhibits higher instantaneous energy than the first two, with spectral concentration from 250 to 390 kHz at 2 ms (see Figure 7.16(c)). An increase in instantaneous energy is observed from the first to the last HSA, occurring simultaneously but across different frequency ranges.

Figure 7.17 presents the HSA of specimen JLS2. The AE waveform related to the first HSA shows a frequency concentration between 275 and 375 kHz at 2.5 ms, with spectral lines at 1.5 ms and 3.4 ms indicating low energy (see Figure 7.17 (a)). The AE waveform for the second HSA demonstrates an energy concentration in the frequency range of 300 to 350 kHz at 2.2 ms, with a spectral line around 3 ms exhibiting medium energy (see Figure 7.17 (b)). Figure 7.17 (c) shows a frequency range from 250 to 375 kHz, similar to that of the HSA in the first cluster, but with high energy and a time shift of 4.8 ms.

Figure 7.18 shows the HSA for the signals from specimen JLS3. The HSA from the first cluster is characterized by a frequency range of 275 to 375 kHz at 2 ms, as illustrated in Figure 7.18 (a). For cluster 2, the HSA narrows the focus to a frequency range of 300 to 350 kHz at 2 ms (See figure 7.18 (b)). For cluster 3, the AE waveform echoes the first cluster's behavior, presenting a frequency range of 250 to 375 kHz at 2 ms (See figure 7.18 (c)). This result indicates that the HSA for the cluster 1 across all specimens are nearly identical around 250-375 kHz with low instantaneous energy. As discussed in the previous section, the second analysis reveals that the majority of AE signals are concentrated in the 250 kHz to 375 kHz frequency band. This confirms that the main damage modes in JLS specimens are interfacial debonding and crack growth, due to load transmission through the adhesive layer. In contrast, AE features classify three modes of damage: matrix cracking, delamination and fiber breakage.

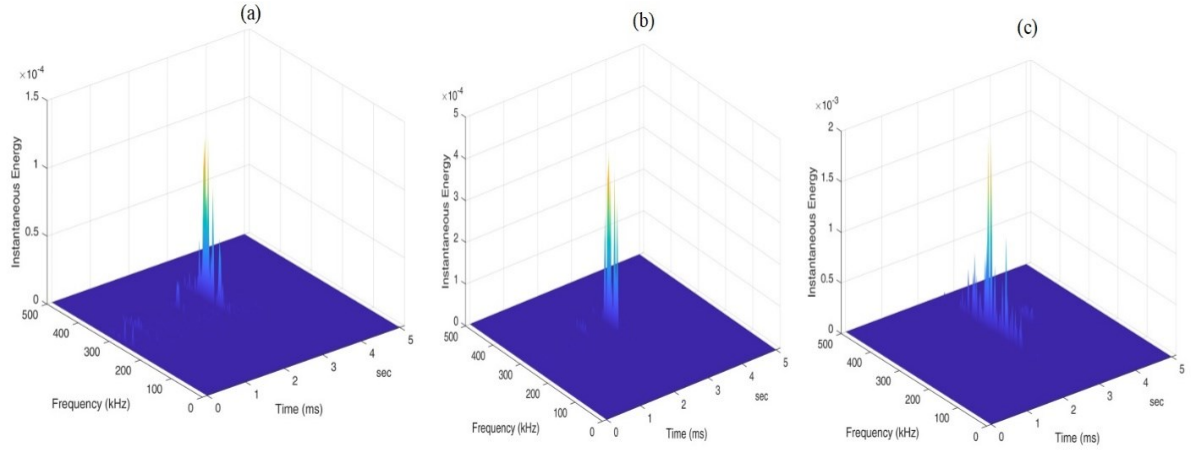

Figure 7.16: Typical AE frequency - domain waveforms from JLS 1: Cluster 1; Cluster 2; and Cluster 3

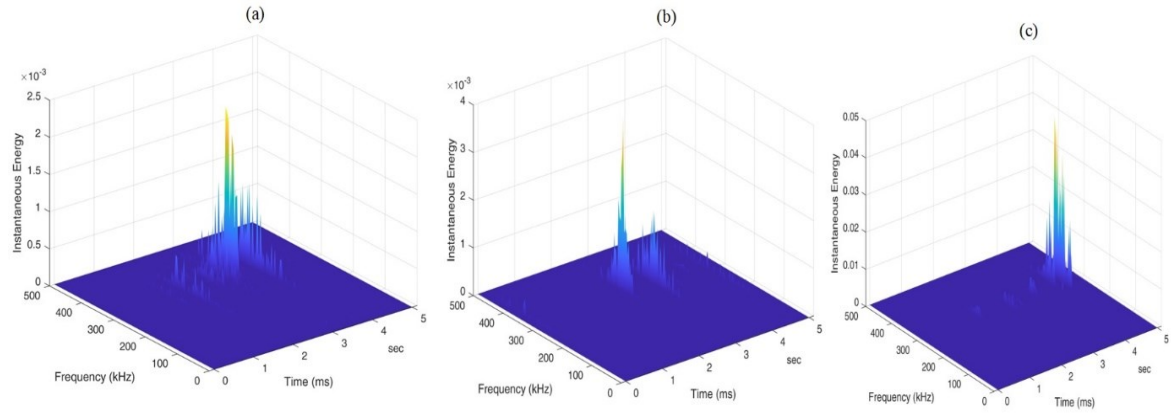

Figure 7.17: Typical AE frequency - domain waveforms from JLS 2: Cluster 1; Cluster 2; and Cluster 3

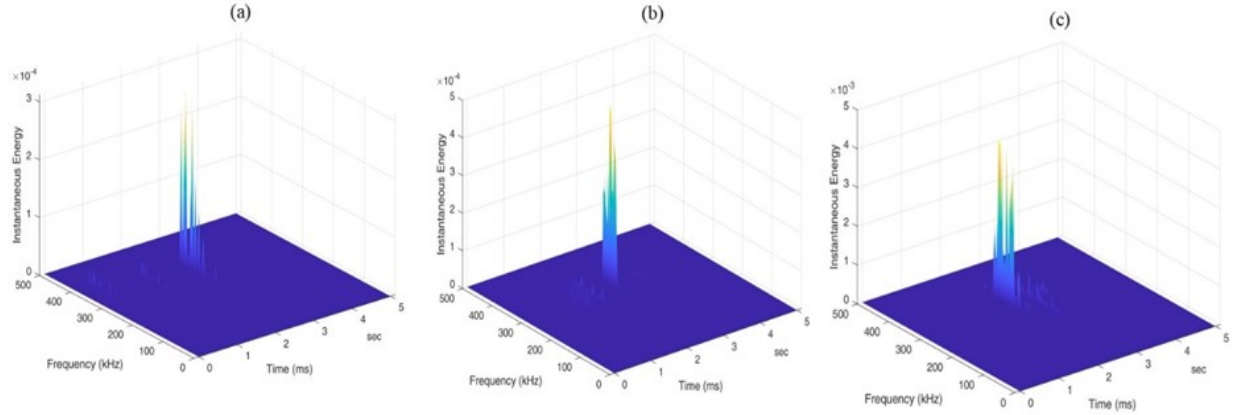

Figure 7.18: Typical AE frequency - domain waveforms from JLS 3: Cluster 1; Cluster 2; and Cluster 3

7.4.4 Validation of AE Results Using Fractographic Analysis

The damage mechanisms identified through AE signal analysis matrix cracking, fi-ber-matrix debonding (or interfacial debonding), and fiber breakage were confirmed through fractographic analysis, providing a comprehensive view of failure progression in the JLS specimens. Fractographic examination post-failure corroborated these mechanisms, revealing specific structural features associated with each damage mode.

Matrix cracking, initially detected as lower-frequency AE signals, was identified as the first stage of damage. This mechanism typically involves the formation of micro-cracks within the matrix material, marking localized stress concentrations that set the stage for further damage progression. Fractographic analysis showed that initial adhesive peel-ing occurred at the knee of the bend in the overlap region (see Figure 19a), suggesting that mechanical stress concentrates in this area, leading to early adhesive debonding under tensile load. This peeling and micro-cracking weaken the bond between the ad-hesive layer and CFRP laminates, initiating interfacial crack growth a critical damage mode highlighted by acoustic emissions in the 250–375 kHz frequency range.

As matrix cracking and adhesive peeling progress, the bond between the matrix and fibers deteriorates, resulting in fiber-matrix debonding or interfacial debonding (see Figure 19d). Fractographic evidence supported this observation, showing compromised integrity of the adhesive layer and leading to laminate debonding, as illustrated in Figure 18b. This interfacial

separation detected by AE signals in the mid-frequency range corresponds to a stage where the laminates are no longer fully bonded, creating a higher risk of delamination. The fractographic analysis confirmed this delamination, revealing that as peeling and debonding advance, individual fibers become exposed to irregular forces. These forces are not fully supported by the matrix, increasing suscep-tibility to rupture.

The final stage of damage, fiber breakage, is marked by high-frequency AE signals. Fractographic evidence in Figure 19c shows fiber breakage at the end of the lamina, where exposed fibers fail under unbalanced forces as matrix support diminishes. The combination of fiber-matrix separation and initial fiber breakage exacerbates the problem of fiber-matrix adhesion, leading to a complete breakdown in the load-bearing capability of the composite. These findings confirm that fiber breakage is the ultimate mode of failure in the JLS specimens, coinciding with the highest recorded AE frequencies and corresponding to catastrophic structural failure. The AE results, confirmed by fractographic analysis, establish interfacial debonding and interlaminar crack growth as the primary failure mechanisms in the JLS specimens. The majority of AE signals, centered in the 250–375 kHz band, indicate that load transmission is primarily occurring through the adhesive layer, with interfacial crack growth responsible for most acoustic activity. The convergence of acoustic and visual data underscores the significant role of adhesive integrity in load transmission, with interfacial cracking emerging as a key indicator of structural damage in adhesively bonded CFRP composites.

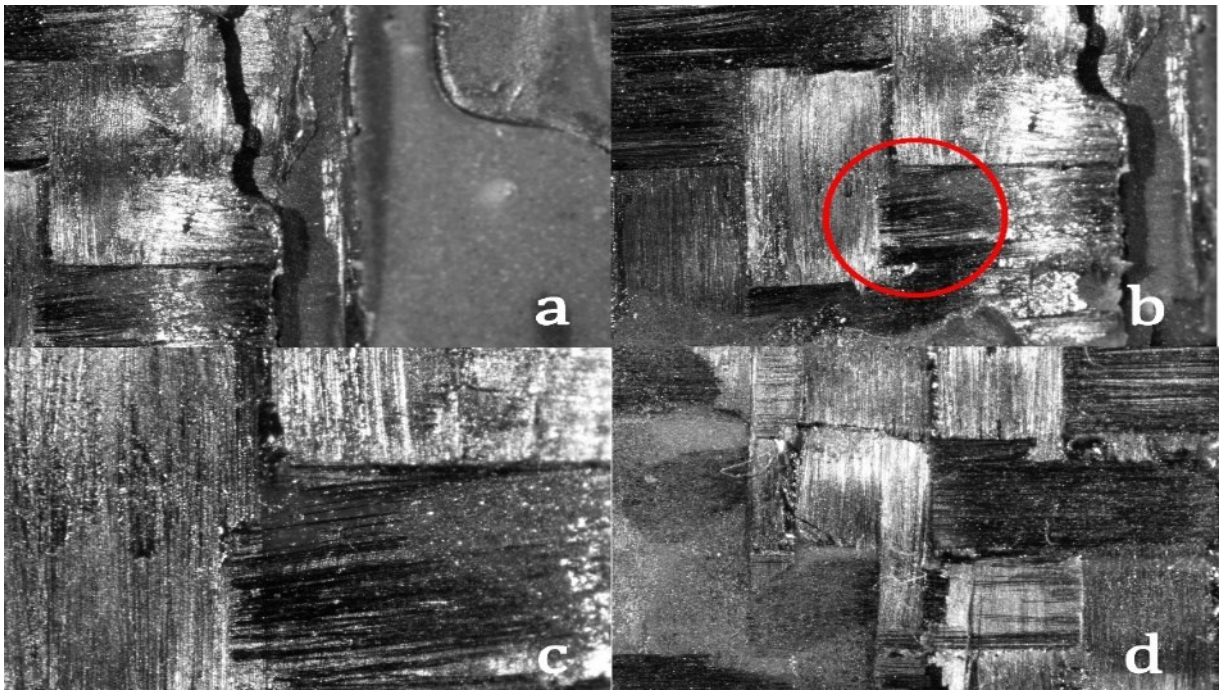

Figure 7.19: Fractographic analysis of CFRP bonded in JLS a) Peeling at the knee of adhesive; (b) Delamination along the boundary of the adhesive layer interface; (c) Fiber breakage; (d) Fiber/Matric Debonding

7.5 Conclusion

This research focused on characterizing damage modes in adhesively bonded CFRP composites under mechanical loading using AE signal analysis. A novel framework was introduced, utilizing a Deep Autoencoder (DAE) to automate the damage characterization process. The

DAE effectively reduced the dimensionality of AE signals, extracting latent waveform features through Singular Value Decomposition (SVD). These features were then analyzed using the k-means clustering algorithm to identify distinct damage modes, which were further validated through Hilbert Spectral Analysis (HSA). Three primary damage modes were identified: matrix cracking, delamination, and interfacial crack growth. The study observed a predominant frequency band between 250 kHz and 375 kHz across all specimens.

This frequency range suggests that the load applied to the CFRP bonded composite was primarily transmitted through the adhesive layer. The observed AE signals predominantly originate from the growth of interfacial cracks within the adhesive, which are essential for generating detectable acoustic events. However, the differences observed in the frequency content of the AE signal within each cluster highlight the complexity of characterizing CFRP damage. This variation underscores the limitations of current methodologies in fully capturing the various damage signatures, highlighting the need for an integrated approach. A conventional method focusing on AE features using amplitude and entropy, analyzed using k-means clustering, identified three main damage modes: matrix cracking, delamination, and fiber breakage. Validation through time-frequency analysis using Hilbert spectral analysis confirmed these categories, correlating them with specific frequency bands.

Fractographic analysis revealed that initial crack growth at the knee of the joggled overlap led to adhesive peeling, compromising the adhesive layers and causing fiber-matrix separation. The AE results corroborated these findings, with most signals centered around the identified frequency band, confirming that interfacial debonding and crack growth are the primary damage modes. Considering these observations, the necessity of integrating traditional and innovative methods becomes evident, enhancing the understanding and identification of complex damage modes in adhesively bonded CFRP composites. The frequency variability observed within clusters highlights a critical area for future research. Merging conventional acoustic emission characteristics with advanced methods will enhance the understanding and identification of complex damage patterns in adhesively bonded CFRP composites. This integrated approach promises to refine damage characterization, contribute to more robust predictive models for material behavior under stress, and advance both theoretical and practical aspects of composite materials engineering.

General conclusion

This thesis focused on developing and applying advanced methods for monitoring damage mechanisms in aerospace materials. It specifically targeted AlSi10Mg and CFRP composites, which are widely used in the aerospace industry. Significant progress was made by integrating traditional signal processing methods with deep learning models. This led to improved accuracy and efficiency in Acoustic Emission signal analysis.

Tensile tests were performed on AlSi10Mg specimens built in different orientations using Selective Laser Melting. AE signals were recorded during the mechanical tests. These signals provided real-time insights into the material's behavior during elastic and plastic deformation. The Continuous Wavelet Transform was used to extract time-frequency features. The data was then processed using deep learning models. A simplified CNN model outperformed other models such as AlexNet and SqueezeNet. It offered faster processing and higher classification accuracy.

To improve AE signal classification, a new methodology combining Fuzzy Artificial Bee Colony with CNN was introduced. This approach addressed issues like suboptimal local maxima during training. It improved performance through data augmentation using Gaussian noise. The hybrid model classified AE signals more accurately. This made it a valuable tool for Structural Health Monitoring in aerospace.

The thesis also explored damage characterization in CFRP composites. Mechanical loading was applied, and AE signals were collected to monitor damage mechanisms. These included matrix cracking, delamination, and fiber breakage. A Deep Autoencoder was developed to automate damage characterization. It reduced the dimensionality of AE signals and identified key latent features. K-means clustering was then used to classify damage modes. Hilbert Spectral Analysis validated the results.

The thesis contributed to the development of advanced AE methods. These methods integrate traditional approaches with machine learning and deep learning models. They significantly improved AE signal classification in both AlSi10Mg and CFRP composites. The FABC-CNN and Deep Autoencoder frameworks offer new tools for predictive maintenance and real-time monitoring in aerospace. This helps reduce operational costs and improves material integrity.

Looking forward, the methodologies developed in this thesis provide a solid foundation for future research. They could be expanded to other materials and stress conditions. This work shows the potential for reliable, automated damage mechanism detection. It opens new possibilities for improving the safety and longevity of aerospace components.

References

[1] R. Soni, R. Verma, R. Kumar Garg, and V. Sharma, "A critical review of recent advances in the aerospace materials," *Mater Today Proc*, Aug. 2023, doi: 10.1016/J.MATPR.2023.08.108.

[2] Z. Zhan, H. Li, and K. Y. Lam, "Development of a novel fatigue damage model with AM effects for life prediction of commonly-used alloys in aerospace," *Int J Mech Sci*, vol. 155, pp. 110–124, May 2019, doi: 10.1016/J.IJMECSCI.2019.02.032.

[3] C. Soutis, "Fibre reinforced composites in aircraft construction," *Progress in Aerospace Sciences*, vol. 41, no. 2, pp. 143–151, Feb. 2005, doi: 10.1016/J.PAEROSCI.2005.02.004.

[4] R. O. Ritchie, "Mechanisms of fatigue-crack propagation in ductile and brittle solids," *Int J Fract*, vol. 100, no. 1, pp. 55–83, 1999, doi: 10.1023/A:1018655917051/METRICS.

[5] M. G. R. Sause and E. Jasiūnienė, Eds., "Structural Health Monitoring Damage Detection Systems for Aerospace," 2021, doi: 10.1007/978-3-030-72192-3.

[6] P. Duchene, S. Chaki, A. Ayadi, and P. Krawczak, "A review of non-destructive techniques used for mechanical damage assessment in polymer composites," *Journal of Materials Science 2018 53:11*, vol. 53, no. 11, pp. 7915–7938, Jan. 2018, doi: 10.1007/S10853-018-2045-6.

[7] A. Güemes, A. Fernandez-Lopez, A. R. Pozo, and J. Sierra-Pérez, "Structural Health Monitoring for Advanced Composite Structures: A Review," *Journal of Composites Science 2020, Vol. 4, Page 13*, vol. 4, no. 1, p. 13, Jan. 2020, doi: 10.3390/JCS4010013.

[8] B. Wang, S. Zhong, T. L. Lee, K. S. Fancey, and J. Mi, "Non-destructive testing and evaluation of composite materials/structures: A state-of-the-art review," *Advances in Mechanical Engineering*, vol. 12, no. 4, Apr. 2020, doi: 10.1177/1687814020913761/ASSET/IMAGES/LARGE/10.1177_1687814020913761-FIG13.JPEG.

[9] R. Gupta *et al.*, "A Review of Sensing Technologies for Non-Destructive Evaluation of Structural Composite Materials," *Journal of Composites Science 2021, Vol. 5, Page 319*, vol. 5, no. 12, p. 319, Dec. 2021, doi: 10.3390/JCS5120319.

[10] D. Angelis, C. Grosse, O. Masayasu, and T. Shiotani, "Acoustic Emission Testing: Basics for Research-Appllication in Civil Engineering," 2018, *Springer*. Accessed: Oct. 24, 2024. [Online]. Available: https://researchportal.vub.be/en/publications/acoustic-emission-testing-basics-for-research-appllication-in-civ

[11] C. R. Ríos-Soberanis, "Acoustic Emission Technique, an Overview as a Characterization Tool in Materials Science," *Journal of Applied Research and Technology*, vol. 9, no. 03, pp. 367–379, Dec. 2011, doi: 10.22201/ICAT.16656423.2011.9.03.431.

[12] A. Carpinteri, G. Lacidogna, G. Niccolini, and S. Puzzi, "Critical defect size distributions in concrete structures detected by the acoustic emission technique," *Meccanica*, vol. 43, no. 3, pp. 349–363, Jun. 2008, doi: 10.1007/S11012-007-9101-7/METRICS.

[13] C. Radhika, R. Shanmugam, M. Ramoni, and G. Bk, "A review on additive manufacturing for aerospace application," *Mater Res Express*, vol. 11, no. 2, p. 022001, Feb. 2024, doi: 10.1088/2053-1591/AD21AD.

[14] S. K. Everton, M. Hirsch, P. I. Stavroulakis, R. K. Leach, and A. T. Clare, "Review of in-situ process monitoring and in-situ metrology for metal additive manufacturing," *Mater Des*, vol. 95, pp. 431–445, Apr. 2016, doi: 10.1016/J.MATDES.2016.01.099.

[15] R. R. Boyer, J. D. Cotton, M. Mohaghegh, and R. E. Schafrik, “Materials considerations for aerospace applications,” *MRS Bull*, vol. 40, no. 12, pp. 1055–1065, Nov. 2015, doi: 10.1557/MRS.2015.278/FIGURES/5.
[16] A. P. Mouritz, *Introduction to Aerospace Materials*. Elsevier Inc., 2012. doi: 10.2514/4.869198.
[17] R. Boyer and N. Padmapriya, “Aircraft Materials,” *Reference Module in Materials Science and Materials Engineering*, 2016, doi: 10.1016/B978-0-12-803581-8.01934-2.
[18] M. V. Orlov and W. O. Badeghaish, “Advanced Non-Metallic Coatings and Composite Materials for O & G Industry,” *J Phys Conf Ser*, vol. 1990, no. 1, p. 012001, Aug. 2021, doi: 10.1088/1742-6596/1990/1/012001.
[19] S. S. Li *et al.*, “Development and applications of aluminum alloys for aerospace industry,” *Journal of Materials Research and Technology*, vol. 27, pp. 944–983, Nov. 2023, doi: 10.1016/J.JMRT.2023.09.274.
[20] J. Bai, “Fiber-reinforced polymer types and properties,” *Advanced Fibre-Reinforced Polymer (FRP) Composites for Structural Applications*, pp. 93–99, Jan. 2022, doi: 10.1016/B978-0-12-820346-0.00014-9.
[21] J. C. Williams and E. A. Starke, “Progress in structural materials for aerospace systems,” *Acta Mater*, vol. 51, no. 19, pp. 5775–5799, Nov. 2003, doi: 10.1016/J.ACTAMAT.2003.08.023.
[22] B. Parveez, M. I. Kittur, I. A. Badruddin, S. Kamangar, M. Hussien, and M. A. Umarfarooq, “Scientific Advancements in Composite Materials for Aircraft Applications: A Review,” *Polymers 2022, Vol. 14, Page 5007*, vol. 14, no. 22, p. 5007, Nov. 2022, doi: 10.3390/POLYM14225007.
[23] G. Karadimas and K. Salonitis, “Ceramic Matrix Composites for Aero Engine Applications—A Review,” *Applied Sciences 2023, Vol. 13, Page 3017*, vol. 13, no. 5, p. 3017, Feb. 2023, doi: 10.3390/APP13053017.
[24] J. McMasters and D. Muncy, “The early development of jet propelled aircraft-a review of German contributions to aerospace technology,” *Collection of Technical Papers - 45th AIAA Aerospace Sciences Meeting*, vol. 3, pp. 1816–1846, 2007, doi: 10.2514/6.2007-151.
[25] Y. Xu, J. Zhu, Z. Wu, Y. Cao, Y. Zhao, and W. Zhang, “A review on the design of laminated composite structures: constant and variable stiffness design and topology optimization,” *Advanced Composites and Hybrid Materials 2018 1:3*, vol. 1, no. 3, pp. 460–477, Apr. 2018, doi: 10.1007/S42114-018-0032-7.
[26] A. Beukers, H. Bersee, and S. Koussios, “Future Aircraft Structures: From Metal to Composite Structures,” *Composite Materials*, pp. 1–50, 2011, doi: 10.1007/978-0-85729-166-0_1.
[27] L. Y. Ljungberg, “Materials selection and design for development of sustainable products,” *Mater Des*, vol. 28, no. 2, pp. 466–479, Jan. 2007, doi: 10.1016/J.MATDES.2005.09.006.
[28] W. E. Frazier, D. Polakovics, and W. Koegel, “Qualifying of metallic materials and structures for aerospace applications,” *JOM*, vol. 53, no. 3, pp. 16–18, 2001, doi: 10.1007/S11837-001-0171-Z/METRICS.
[29] E. A. Starke and J. T. Staley, “Application of modern aluminum alloys to aircraft,” *Progress in Aerospace Sciences*, vol. 32, no. 2–3, pp. 131–172, Jan. 1996, doi: 10.1016/0376-0421(95)00004-6.
[30] A. Bouzekova-Penkova and A. Miteva, “Some Aerospace Applications of 7075 (B95) Aluminium Alloy,” *Aerospace Research in Bulgaria*, vol. 34, pp. 165–179, 2022, doi: 10.3897/ARB.V34.E15.

[31] P. Rambabu, N. Eswara Prasad, V. V. Kutumbarao, and R. J. H. Wanhill, “Aluminium Alloys for Aerospace Applications,” pp. 29–52, 2017, doi: 10.1007/978-981-10-2134-3_2.
[32] R. R. Boyer, “Titanium for aerospace: Rationale and applications,” *Advanced Performance Materials*, vol. 2, no. 4, pp. 349–368, Oct. 1995, doi: 10.1007/BF00705316/METRICS.
[33] W. M. Garrison, “Ultrahigh-strength steels for aerospace applications,” *JOM*, vol. 42, no. 5, pp. 20–24, May 1990, doi: 10.1007/BF03220942/METRICS.
[34] D. K. Ganji and G. Rajyalakshmi, “Influence of Alloying Compositions on the Properties of Nickel-Based Superalloys: A Review,” *Lecture Notes in Mechanical Engineering*, pp. 537–555, 2020, doi: 10.1007/978-981-15-1071-7_44.
[35] J. McCrory, “Advanced Acoustic Emission (AE) monitoring techniques for aerospace structures,” 2016.
[36] N. Ramli, N. Mazlan, Y. Ando, K. Abdan, and Z. Leman, “Advanced Polymer Composite for Aerospace Engineering Applications,” *Advanced Composites in Aerospace Engineering Applications*, pp. 1–21, Jan. 2022, doi: 10.1007/978-3-030-88192-4_1.
[37] F. Ozturk, M. Cobanoglu, and R. E. Ece, “Recent advancements in thermoplastic composite materials in aerospace industry,” *https://doi.org/10.1177/08927057231222820*, Dec. 2023, doi: 10.1177/08927057231222820.
[38] J. Matsui, “Polymer matrix composites (PMC) in aerospace,” *Advanced Composite Materials*, vol. 4, no. 3, pp. 197–208, 1995, doi: 10.1163/156855195X00014.
[39] C. Soutis, “Carbon fiber reinforced plastics in aircraft construction,” *Materials Science and Engineering: A*, vol. 412, no. 1–2, pp. 171–176, Dec. 2005, doi: 10.1016/J.MSEA.2005.08.064.
[40] G. Nkurunziza, A. Debaiky, P. Cousin, and B. Benmokrane, “Durability of GFRP bars: a critical review of the literature,” *Progress in Structural Engineering and Materials*, vol. 7, no. 4, pp. 194–209, Oct. 2005, doi: 10.1002/PSE.205.
[41] Z. Zhao *et al.*, “An overview of graphene and its derivatives reinforced metal matrix composites: Preparation, properties and applications,” *Carbon N Y*, vol. 170, pp. 302–326, Dec. 2020, doi: 10.1016/J.CARBON.2020.08.040.
[42] X. Wang, X. Gao, Z. Zhang, L. Cheng, H. Ma, and W. Yang, “Advances in modifications and high-temperature applications of silicon carbide ceramic matrix composites in aerospace: A focused review,” *J Eur Ceram Soc*, vol. 41, no. 9, pp. 4671–4688, Aug. 2021, doi: 10.1016/J.JEURCERAMSOC.2021.03.051.
[43] H. Altenbach, J. Altenbach, and W. Kissing, “Classification of Composite Materials,” *Mechanics of Composite Structural Elements*, pp. 1–14, 2004, doi: 10.1007/978-3-662-08589-9_1.
[44] D. W. Martinez, M. Espino, H. M. Cascolan, J. L. Crisostomo, and J. R. Dizon, “A Comprehensive Review on the Application of 3D Printing in the Aerospace Industry,” *Key Eng Mater*, vol. 913, pp. 27–34, 2022, doi: 10.4028/P-94A9ZB.
[45] M. Khorasani, A. H. Ghasemi, B. Rolfe, and I. Gibson, “Additive manufacturing a powerful tool for the aerospace industry,” *Rapid Prototyp J*, vol. 28, no. 1, pp. 87–100, Jan. 2022, doi: 10.1108/RPJ-01-2021-0009/FULL/XML.
[46] J. C. Williams and E. A. Starke, “Progress in structural materials for aerospace systems,” *Acta Mater*, vol. 51, no. 19, pp. 5775–5799, Nov. 2003, doi: 10.1016/J.ACTAMAT.2003.08.023.

[47] J. C. Najmon, S. Raeisi, and A. Tovar, “Review of additive manufacturing technologies and applications in the aerospace industry,” *Additive Manufacturing for the Aerospace Industry*, pp. 7–31, Jan. 2019, doi: 10.1016/B978-0-12-814062-8.00002-9.

[48] J. Bonnín Roca, P. Vaishnav, R. E. Laureijs, J. Mendonça, and E. R. H. Fuchs, “Technology cost drivers for a potential transition to decentralized manufacturing,” *Addit Manuf*, vol. 28, pp. 136–151, Aug. 2019, doi: 10.1016/J.ADDMA.2019.04.010.

[49] J. K. Watson and K. M. B. Taminger, “A decision-support model for selecting additive manufacturing versus subtractive manufacturing based on energy consumption,” *J Clean Prod*, vol. 176, pp. 1316–1322, Mar. 2018, doi: 10.1016/J.JCLEPRO.2015.12.009.

[50] L. Zhu, N. Li, and P. R. N. Childs, “Light-weighting in aerospace component and system design,” *Propulsion and Power Research*, vol. 7, no. 2, pp. 103–119, Jun. 2018, doi: 10.1016/J.JPPR.2018.04.001.

[51] A. H. Alami *et al.*, “Additive manufacturing in the aerospace and automotive industries: Recent trends and role in achieving sustainable development goals,” *Ain Shams Engineering Journal*, vol. 14, no. 11, p. 102516, Nov. 2023, doi: 10.1016/J.ASEJ.2023.102516.

[52] S. Singh, S. Ramakrishna, and R. Singh, “Material issues in additive manufacturing: A review,” *J Manuf Process*, vol. 25, pp. 185–200, Jan. 2017, doi: 10.1016/J.JMAPRO.2016.11.006.

[53] B. Blakey-Milner *et al.*, “Metal additive manufacturing in aerospace: A review,” *Mater Des*, vol. 209, p. 110008, Nov. 2021, doi: 10.1016/J.MATDES.2021.110008.

[54] R. Wagmare, R. Harshe, J. Pednekar, and T. U. Patro, “Additive manufacturing of continuous fiber-reinforced polymer composites: current trend and future directions,” *Progress in Additive Manufacturing 2024*, pp. 1–28, Sep. 2024, doi: 10.1007/S40964-024-00777-9.

[55] H. A. Hegab, “Design for additive manufacturing of composite materials and potential alloys: a review,” *Manuf Rev (Les Ulis)*, vol. 3, p. 11, 2016, doi: 10.1051/MFREVIEW/2016010.

[56] J. H. Tan, W. L. E. Wong, and K. W. Dalgarno, “An overview of powder granulometry on feedstock and part performance in the selective laser melting process,” *Addit Manuf*, vol. 18, pp. 228–255, Dec. 2017, doi: 10.1016/J.ADDMA.2017.10.011.

[57] K. Osipovich *et al.*, “Wire-Feed Electron Beam Additive Manufacturing: A Review,” *Metals 2023, Vol. 13, Page 279*, vol. 13, no. 2, p. 279, Jan. 2023, doi: 10.3390/MET13020279.

[58] M. Lalegani Dezaki, M. K. A. Mohd Ariffin, and S. Hatami, “An overview of fused deposition modelling (FDM): research, development and process optimisation,” *Rapid Prototyp J*, vol. 27, no. 3, pp. 562–582, Apr. 2021, doi: 10.1108/RPJ-08-2019-0230/FULL/XML.

[59] N. E. Uzan, R. Shneck, O. Yeheskel, and N. Frage, “High-temperature mechanical properties of AlSi10Mg specimens fabricated by additive manufacturing using selective laser melting technologies (AM-SLM),” *Addit Manuf*, vol. 24, pp. 257–263, Dec. 2018, doi: 10.1016/J.ADDMA.2018.09.033.

[60] N. Limbasiya, A. Jain, H. Soni, V. Wankhede, G. Krolczyk, and P. Sahlot, “A comprehensive review on the effect of process parameters and post-process treatments on microstructure and mechanical properties of selective laser melting of AlSi10Mg,” *Journal of Materials Research and Technology*, vol. 21, pp. 1141–1176, Nov. 2022, doi: 10.1016/J.JMRT.2022.09.092.

[61] V. Madhavadas *et al.*, “A review on metal additive manufacturing for intricately shaped aerospace components,” *CIRP J Manuf Sci Technol*, vol. 39, pp. 18–36, Nov. 2022, doi: 10.1016/J.CIRPJ.2022.07.005.
[62] H. Assler, J. T.-9th E. C. on NDT, and undefined 2006, “Design of aircraft structures under special consideration of NDT,” *ndt.net*, Accessed: Oct. 24, 2024. [Online]. Available: https://www.ndt.net/article/ecndt2006/doc/_keynote.pdf
[63] G. A. Kardomateas and P. H. Geubelle, “Fatigue and Fracture Mechanics in Aerospace Structures,” *Encyclopedia of Aerospace Engineering*, Dec. 2010, doi: 10.1002/9780470686652.EAE142.
[64] J. C. Williams and E. A. Starke, “Progress in structural materials for aerospace systems,” *Acta Mater*, vol. 51, no. 19, pp. 5775–5799, Nov. 2003, doi: 10.1016/J.ACTAMAT.2003.08.023.
[65] S. Lynch, “Failures of metallic components involving environmental degradation and material- selection issues,” *Corrosion Reviews*, vol. 35, no. 4–5, pp. 191–204, Oct. 2017, doi: 10.1515/CORRREV-2017-0023/MACHINEREADABLECITATION/RIS.
[66] A. Dasgupta and M. Pecht, “Material Failure Mechanisms and Damage Models,” *IEEE Trans Reliab*, vol. 40, no. 5, pp. 531–536, 1991, doi: 10.1109/24.106769.
[67] A. Dalmau, C. Richard, and A. Igual – Muñoz, “Degradation mechanisms in martensitic stainless steels: Wear, corrosion and tribocorrosion appraisal,” *Tribol Int*, vol. 121, pp. 167–179, May 2018, doi: 10.1016/J.TRIBOINT.2018.01.036.
[68] B. T. Lu, Z. K. Chen, J. L. Luo, B. M. Patchett, and Z. H. Xu, “Pitting and stress corrosion cracking behavior in welded austenitic stainless steel,” *Electrochim Acta*, vol. 50, no. 6, pp. 1391–1403, Jan. 2005, doi: 10.1016/J.ELECTACTA.2004.08.036.
[69] S. M. O. Tavares and P. M. S. T. de Castro, “An overview of fatigue in aircraft structures,” *Fatigue Fract Eng Mater Struct*, vol. 40, no. 10, pp. 1510–1529, Oct. 2017, doi: 10.1111/FFE.12631.
[70] E. Salvati, “Evaluating fatigue onset in metallic materials: Problem, current focus and future perspectives,” *Int J Fatigue*, vol. 188, p. 108487, Nov. 2024, doi: 10.1016/J.IJFATIGUE.2024.108487.
[71] S. J. Findlay and N. D. Harrison, “Why aircraft fail,” *Materials Today*, vol. 5, no. 11, pp. 18–25, Nov. 2002, doi: 10.1016/S1369-7021(02)01138-0.
[72] A. Khalifeh, “Fatigue Failure in Aircraft Materials,” pp. 63–79, 2025, doi: 10.1007/978-3-031-65850-1_4.
[73] C. Laird and G. C. Smith, “Crack propagation in high stress fatigue,” *Philosophical Magazine*, vol. 7, no. 77, pp. 847–857, 1962, doi: 10.1080/14786436208212674.
[74] K. Kida, T. Yamazaki, M. Shibata, N. Oguma, and H. Harada, “Crack initiation from micro surface holes in bearings under rolling contact fatigue,” *Fatigue Fract Eng Mater Struct*, vol. 27, no. 6, pp. 481–493, Jun. 2004, doi: 10.1111/J.1460-2695.2004.00771.X.
[75] U. Zerbst, M. Vormwald, R. Pippan, H. P. Gänser, C. Sarrazin-Baudoux, and M. Madia, “About the fatigue crack propagation threshold of metals as a design criterion – A review,” *Eng Fract Mech*, vol. 153, pp. 190–243, Mar. 2016, doi: 10.1016/J.ENGFRACMECH.2015.12.002.
[76] B. Raj, T. Jayakumar, and B. P. C. Rao, “Non-destructive testing and evaluation for structural integrity,” *Sadhana*, vol. 20, no. 1, pp. 5–38, Feb. 1995, doi: 10.1007/BF02747282/METRICS.
[77] N. Pugno, M. Ciavarella, P. Cornetti, and A. Carpinteri, “A generalized Paris’ law for fatigue crack growth,” *J Mech Phys Solids*, vol. 54, no. 7, pp. 1333–1349, Jul. 2006, doi: 10.1016/J.JMPS.2006.01.007.

[78] B. F. Dyson, “Creep and fracture of metals : mechanisms and mechanics,” *Revue de Physique Appliquée*, vol. 23, no. 4, pp. 605–613, Apr. 1988, doi: 10.1051/RPHYSAP:01988002304060500.
[79] W. Abd-Elaziem, J. Liu, N. Ghoniem, and X. Li, “Effect of nanoparticles on creep behaviour of metals: A review,” *Journal of Materials Research and Technology*, vol. 26, pp. 3025–3053, Sep. 2023, doi: 10.1016/J.JMRT.2023.08.068.
[80] M. J. Jackson and V. Ruxton, “Creep-Feed Grinding Wheel Development for Safely Grinding Aerospace Alloys,” *J Mater Eng Perform*, vol. 30, no. 3, pp. 2220–2228, Mar. 2021, doi: 10.1007/S11665-021-05489-7/FIGURES/7.
[81] M. F. Ashby and C. A. Abel, “Materials selection to resist creep,” *Philosophical Transactions of the Royal Society of London. Series A: Physical and Engineering Sciences*, vol. 351, no. 1697, pp. 451–468, Jun. 1995, doi: 10.1098/RSTA.1995.0046.
[82] M. Perrut, P. Caron, M. Thomas, and A. Couret, “High temperature materials for aerospace applications: Ni-based superalloys and γ-TiAl alloys,” *C R Phys*, vol. 19, no. 8, pp. 657–671, Dec. 2018, doi: 10.1016/J.CRHY.2018.10.002.
[83] F. N, V. Venkataraman, and M. Nagaral, “Mechanical characterization and wear behavior of aerospace alloy AA2124 and micro B4C reinforced metal composites,” *Journal of Metals, Materials and Minerals*, vol. 30, no. 4, Dec. 2020, Accessed: Oct. 31, 2024. [Online]. Available: https://digital.car.chula.ac.th/jmmm/vol30/iss4/12
[84] J. Qadir, A. Savio Lewise, G. Jims John Wessley, and G. Diju Samuel, “Influence of nanoparticles in reinforced aluminium metal matrix composites in aerospace applications – A review,” *Mater Today Proc*, Jul. 2023, doi: 10.1016/J.MATPR.2023.06.414.
[85] J. A. Williams, “Wear and wear particles—some fundamentals,” *Tribol Int*, vol. 38, no. 10, pp. 863–870, Oct. 2005, doi: 10.1016/J.TRIBOINT.2005.03.007.
[86] P. W. R. Beaumont, “The Structural Integrity of Composite Materials and Long-Life Implementation of Composite Structures,” *Applied Composite Materials*, vol. 27, no. 5, pp. 449–478, Oct. 2020, doi: 10.1007/S10443-020-09822-6/FIGURES/13.
[87] T. Huang and M. Bobyr, “A Review of Delamination Damage of Composite Materials,” *Journal of Composites Science 2023, Vol. 7, Page 468*, vol. 7, no. 11, p. 468, Nov. 2023, doi: 10.3390/JCS7110468.
[88] D. Kreculj and B. Rasuo, “Impact damage modeling in laminated composite aircraft structures,” *Sustainable Composites for Aerospace Applications*, pp. 125–153, Jan. 2018, doi: 10.1016/B978-0-08-102131-6.00007-4.
[89] J. G. Williams, “The fracture mechanics of delamination tests,” *J Strain Anal Eng Des*, vol. 24, no. 4, pp. 207–214, Oct. 1989, doi: 10.1243/03093247V244207/ASSET/03093247V244207.FP.PNG_V03.
[90] S. Abrate, “Matrix cracking in laminated composites: A review,” *Composites Engineering*, vol. 1, no. 6, pp. 337–353, Jan. 1991, doi: 10.1016/0961-9526(91)90039-U.
[91] R. Talreja, “Stiffness properties of composite laminates with matrix cracking and interior delamination,” *Eng Fract Mech*, vol. 25, no. 5–6, pp. 751–762, Jan. 1986, doi: 10.1016/0013-7944(86)90038-X.
[92] S. Abrate, “Impact on Laminated Composites: Recent Advances,” *Appl Mech Rev*, vol. 47, no. 11, pp. 517–544, Nov. 1994, doi: 10.1115/1.3111065.
[93] T. W. Clyne and D. Hull, “An Introduction to Composite Materials,” *An Introduction to Composite Materials*, Jul. 2019, doi: 10.1017/9781139050586.
[94] Y. Geng and C. K. Y. Leung, “A microstructural study of fibre/mortar interfaces during fibre debonding and pull-out,” *J Mater Sci*, vol. 31, no. 5, pp. 1285–1294, Mar. 1996, doi: 10.1007/BF00353108/METRICS.

[95] H. M. Flower, “An Introduction to Composite Materials — Second edition D. Hull and T.W. Clyne Cambridge University Press, The Pitt Building, Trumpington Street, Cambridge CB2 IRP. 1996. 326pp. Illustrated. £19.95.,” *The Aeronautical Journal*, vol. 101, no. 1005, pp. 228–228, May 1997, doi: 10.1017/S0001924000066410.
[96] J. Halpin and S. Tsai, “Effects of environmental factors on composite materials,” 1969, Accessed: Nov. 03, 2024. [Online]. Available: https://citeseerx.ist.psu.edu/document?repid=rep1&type=pdf&doi=06f0a156110c13c202eb13d3e46c1378da1886f3
[97] S. Sethi and B. C. Ray, “Environmental effects on fibre reinforced polymeric composites: Evolving reasons and remarks on interfacial strength and stability,” *Adv Colloid Interface Sci*, vol. 217, pp. 43–67, Mar. 2015, doi: 10.1016/J.CIS.2014.12.005.
[98] C. B. Scruby, “An introduction to acoustic emission,” *J Phys E*, vol. 20, no. 8, p. 946, Aug. 1987, doi: 10.1088/0022-3735/20/8/001.
[99] R. Gupta *et al.*, “A Review of Sensing Technologies for Non-Destructive Evaluation of Structural Composite Materials,” *Journal of Composites Science 2021, Vol. 5, Page 319*, vol. 5, no. 12, p. 319, Dec. 2021, doi: 10.3390/JCS5120319.
[100] C. B. Scruby, “An introduction to acoustic emission,” *J Phys E*, vol. 20, no. 8, p. 946, Aug. 1987, doi: 10.1088/0022-3735/20/8/001.
[101] V. I. Levitas and M. Javanbakht, “Interaction between phase transformations and dislocations at the nanoscale. Part 1. General phase field approach,” *J Mech Phys Solids*, vol. 82, pp. 287–319, Sep. 2015, doi: 10.1016/J.JMPS.2015.05.005.
[102] D. G. Aggelis *et al.*, “Acoustic Emission,” *Springer Aerospace Technology*, pp. 175–217, 2021, doi: 10.1007/978-3-030-72192-3_7/FIGURES/19.
[103] C. Barile, C. Casavola, G. Pappalettera, and V. Paramsamy Kannan, “Sound Waves and Acoustic Emission,” 2023, doi: 10.1007/978-3-031-23789-8.
[104] S. Ashraf, S. Khan, and V. K. Oad, “Microcracking monitoring and damage detection of graphene nanoplatelets-cement composites based on acoustic emission technology,” *Case Studies in Construction Materials*, vol. 18, p. e01844, Jul. 2023, doi: 10.1016/J.CSCM.2023.E01844.
[105] T. He, Y. Ji, Y. Qi, L. Q. Chen, and M. Feng, “Stress-dependence of dislocation dissociation, nucleation and annihilation in elastically anisotropic Cu,” *Int J Plast*, vol. 138, p. 102927, Mar. 2021, doi: 10.1016/J.IJPLAS.2021.102927.
[106] V. I. Levitas, “Phase transformations, fracture, and other structural changes in inelastic materials,” *Int J Plast*, vol. 140, p. 102914, May 2021, doi: 10.1016/J.IJPLAS.2020.102914.
[107] M. Saeedifar and D. Zarouchas, “Damage characterization of laminated composites using acoustic emission: A review,” *Compos B Eng*, vol. 195, p. 108039, Aug. 2020, doi: 10.1016/J.COMPOSITESB.2020.108039.
[108] C. Barile, C. Casavola, G. Pappalettera, and V. Paramsamy Kannan, “Laplacian score and K-means data clustering for damage characterization of adhesively bonded CFRP composites by means of acoustic emission technique,” *Applied Acoustics*, vol. 185, p. 108425, Jan. 2022, doi: 10.1016/J.APACOUST.2021.108425.
[109] V. A. D. De Almeida, F. G. Baptista, and P. R. De Aguiar, “Piezoelectric transducers assessed by the pencil lead break for impedance-based structural health monitoring,” *IEEE Sens J*, vol. 15, no. 2, pp. 693–702, Feb. 2015, doi: 10.1109/JSEN.2014.2352171.
[110] J. Melchiorre, A. Manuello Bertetto, M. M. Rosso, and G. C. Marano, “Acoustic Emission and Artificial Intelligence Procedure for Crack Source Localization,” *Sensors 2023, Vol. 23, Page 693*, vol. 23, no. 2, p. 693, Jan. 2023, doi: 10.3390/S23020693.
[111] G. C. McLaskey, “Stress Wave Source Characterization: Impact, Fracture, and Sliding Friction,” 2011.

[112] Y. H. Pao, “THEORY OF ACOUSTIC EMISSION,” *American Society of Mechanical Engineers, Applied Mechanics Division, AMD*, pp. 464–497, Jan. 1981, doi: 10.1016/B978-0-08-026724-1.50058-3.
[113] T. Jayakumar, “NDT Techniques: Acoustic Emission,” *Encyclopedia of Materials: Science and Technology*, pp. 6001–6003, Jan. 2001, doi: 10.1016/B0-08-043152-6/01053-6.
[114] M. Saeedifar and D. Zarouchas, “Damage characterization of laminated composites using acoustic emission: A review,” *Compos B Eng*, vol. 195, p. 108039, Aug. 2020, doi: 10.1016/J.COMPOSITESB.2020.108039.
[115] K. Ono, “Acoustic Emission,” *Springer Handbook of Acoustics*, pp. 1209–1229, 2014, doi: 10.1007/978-1-4939-0755-7_30.
[116] I. M. De Rosa, C. Santulli, and F. Sarasini, “Acoustic emission for monitoring the mechanical behaviour of natural fibre composites: A literature review,” *Compos Part A Appl Sci Manuf*, vol. 40, no. 9, pp. 1456–1469, Sep. 2009, doi: 10.1016/J.COMPOSITESA.2009.04.030.
[117] D. G. Aggelis, “Classification of cracking mode in concrete by acoustic emission parameters,” *Mech Res Commun*, vol. 38, no. 3, pp. 153–157, Apr. 2011, doi: 10.1016/J.MECHRESCOM.2011.03.007.
[118] P. Antonaci, P. Bocca, and D. Masera, “Fatigue crack propagation monitoring by Acoustic Emission signal analysis,” *Eng Fract Mech*, vol. 81, pp. 26–32, Feb. 2012, doi: 10.1016/J.ENGFRACMECH.2011.09.017.
[119] M. F. Haider and V. Giurgiutiu, “A Helmholtz Potential Approach to the Analysis of Guided Wave Generation During Acoustic Emission Events,” *J Nondestruct Eval Diagn Progn Eng Syst*, vol. 1, no. 2, pp. 021002-021002–11, May 2018, doi: 10.1115/1.4038116.
[120] S. Pant, “Lamb Wave Propagation and Material Characterization of Metallic and Composite Aerospace Structures for Improved Structural Health Monitoring (SHM),” 2014, doi: 10.22215/ETD/2014-10409.
[121] X. Yu, “Dynamic acoustic emission for the characterization of the nonlinear behavior of complex materials,” Sep. 2020, Accessed: Oct. 31, 2024. [Online]. Available: https://theses.hal.science/tel-03117827
[122] H. P. Rossmanith, “Elastic Wave Propagation,” *Rock Fracture Mechanics*, pp. 229–251, 1983, doi: 10.1007/978-3-7091-2750-6_6.
[123] M. Muller, A. Sutin, R. Guyer, M. Talmant, P. Laugier, and P. A. Johnson, “Nonlinear resonant ultrasound spectroscopy (NRUS) applied to damage assessment in bone,” *Journal of the Acoustical Society of America*, vol. 118, no. 6, pp. 3946–3952, Dec. 2005, doi: 10.1121/1.2126917.
[124] B. Gurevich and J. M. Carcione, “Attenuation and Dispersion of Elastic Waves in Porous Rocks: Mechanisms and models,” *Attenuation and Dispersion of Elastic Waves in Porous Rocks: Mechanisms and models*, Dec. 2022, doi: 10.1190/1.9781560803911.
[125] M. G. R. Sause, “Acoustic emission,” *Springer Series in Materials Science*, vol. 242, pp. 131–359, 2016, doi: 10.1007/978-3-319-30954-5_4.
[126] J. H. Oh, Y. J. Kim, and Y. Y. Kim, “Wave attenuation and dissipation mechanisms in viscoelastic phononic crystals,” *J Appl Phys*, vol. 113, no. 10, Mar. 2013, doi: 10.1063/1.4795285/964771.
[127] Z. El and H. Hamam, “Simulation numérique et analyse de l’émission acoustique due à la rupture de fibre et à la décohésion à l’interface fibre/matrice dans un microcomposite,” Dec. 2020, Accessed: Nov. 04, 2024. [Online]. Available: https://theses.hal.science/tel-03208857

[128] M. Shateri, M. Ghaib, D. Svecova, and D. Thomson, “On acoustic emission for damage detection and failure prediction in fiber reinforced polymer rods using pattern recognition analysis,” *Smart Mater Struct*, vol. 26, no. 6, p. 065023, May 2017, doi: 10.1088/1361-665X/AA6E43.
[129] C. Barile, C. Casavola, G. Pappalettera, and P. K. Vimalathithan, “Damage characterization in composite materials using acoustic emission signal-based and parameter-based data,” *Compos B Eng*, vol. 178, p. 107469, Dec. 2019, doi: 10.1016/J.COMPOSITESB.2019.107469.
[130] A. ; Jierula *et al.*, “A Review of Acoustic Emission Source Localization Techniques in Different Dimensions,” *Applied Sciences 2024, Vol. 14, Page 8684*, vol. 14, no. 19, p. 8684, Sep. 2024, doi: 10.3390/APP14198684.
[131] Y. Li and F. Xu, “All-phase fast Fourier transform and multiple cross-correlation analysis based on Geiger iteration for acoustic emission sources localization in complex metallic structures,” *https://doi.org/10.1177/14759217211027481*, vol. 21, no. 3, pp. 1235–1250, Jun. 2021, doi: 10.1177/14759217211027481.
[132] G. L. Trigg, “Mathematical Tools for Physicists,” *Mathematical Tools for Physicists*, pp. 1–676, May 2006, doi: 10.1002/3527607773.
[133] C. Van Loan, “Computational Frameworks for the Fast Fourier Transform,” *Computational Frameworks for the Fast Fourier Transform*, Jan. 1992, doi: 10.1137/1.9781611970999.
[134] R. X. Gao and R. Yan, “Continuous Wavelet Transform,” *Wavelets*, pp. 33–48, 2011, doi: 10.1007/978-1-4419-1545-0_3.
[135] Y. Li and F. Xu, “Structural damage monitoring for metallic panels based on acoustic emission and adaptive improvement variational mode decomposition–wavelet packet transform,” *https://doi.org/10.1177/14759217211008969*, vol. 21, no. 2, pp. 710–730, Apr. 2021, doi: 10.1177/14759217211008969.
[136] D. Baccar and D. Söffker, “Wear detection by means of wavelet-based acoustic emission analysis,” *Mech Syst Signal Process*, vol. 60–61, pp. 198–207, Aug. 2015, doi: 10.1016/J.YMSSP.2015.02.012.
[137] Y. Zhu, G. Li, S. Tang, R. Wang, H. Su, and C. Wang, “Acoustic signal-based fault detection of hydraulic piston pump using a particle swarm optimization enhancement CNN,” *Applied Acoustics*, vol. 192, p. 108718, Apr. 2022, doi: 10.1016/J.APACOUST.2022.108718.
[138] H. Chen, R. C. K. Wong, S. Park, and R. Hugo, “An AI-based monitoring system for external disturbance detection and classification near a buried pipeline,” *Mech Syst Signal Process*, vol. 196, p. 110346, Aug. 2023, doi: 10.1016/J.YMSSP.2023.110346.
[139] H. WenQin, L. Ying, G. AiJun, and F. G. Yuan, “Damage Modes Recognition and Hilbert-Huang Transform Analyses of CFRP Laminates Utilizing Acoustic Emission Technique,” *Applied Composite Materials*, vol. 23, no. 2, pp. 155–178, Apr. 2016, doi: 10.1007/S10443-015-9454-3/FIGURES/30.
[140] G. Siracusano *et al.*, “A framework for the damage evaluation of acoustic emission signals through Hilbert–Huang transform,” *Mech Syst Signal Process*, vol. 75, pp. 109–122, Jun. 2016, doi: 10.1016/J.YMSSP.2015.12.004.
[141] S. E. Hamdi, A. Le Duff, L. Simon, G. Plantier, A. Sourice, and M. Feuilloy, “Acoustic emission pattern recognition approach based on Hilbert–Huang transform for structural health monitoring in polymer-composite materials,” *Applied Acoustics*, vol. 74, no. 5, pp. 746–757, May 2013, doi: 10.1016/J.APACOUST.2012.11.018.
[142] A. K. Jain, “Data clustering: 50 years beyond K-means,” *Pattern Recognit Lett*, vol. 31, no. 8, pp. 651–666, Jun. 2010, doi: 10.1016/J.PATREC.2009.09.011.

[143] A. Likas, N. Vlassis, and J. J. Verbeek, “The global k-means clustering algorithm,” *Pattern Recognit*, vol. 36, no. 2, pp. 451–461, Feb. 2003, doi: 10.1016/S0031-3203(02)00060-2.
[144] H. L. Dawson, O. Dubrule, and C. M. John, “Impact of dataset size and convolutional neural network architecture on transfer learning for carbonate rock classification,” *Comput Geosci*, vol. 171, p. 105284, Feb. 2023, doi: 10.1016/J.CAGEO.2022.105284.
[145] J. L. Bautista, Y. K. Lee, and H. S. Shin, “Speech Emotion Recognition Based on Parallel CNN-Attention Networks with Multi-Fold Data Augmentation,” *Electronics 2022, Vol. 11, Page 3935*, vol. 11, no. 23, p. 3935, Nov. 2022, doi: 10.3390/ELECTRONICS11233935.
[146] Z. Lyu *et al.*, “Robust automatic modulation classification based on convolutional and recurrent fusion network,” *Physical Communication*, vol. 43, p. 101213, Dec. 2020, doi: 10.1016/J.PHYCOM.2020.101213.
[147] M. Barbosh, K. Dunphy, and A. Sadhu, “Time-Frequency Assisted Deep Learning for Crack Localization Using Acoustic Emission Data,” *Lecture Notes in Civil Engineering*, vol. 244, pp. 185–196, 2022, doi: 10.1007/978-981-19-0656-5_16/COVER.
[148] “(PDF) Using Fuzzy C-means to Discover Concept-drift Patterns for Membership Functions.” Accessed: May 02, 2023. [Online]. Available: https://www.researchgate.net/publication/361544353_Using_Fuzzy_C-means_to_Discover_Concept-drift_Patterns_for_Membership_Functions
[149] M. Kaveh, · Mohammad, S. Mesgari, and B. Mohammad, “Application of Meta-Heuristic Algorithms for Training Neural Networks and Deep Learning Architectures: A Comprehensive Review,” *Neural Processing Letters 2022*, pp. 1–104, Oct. 2022, doi: 10.1007/S11063-022-11055-6.
[150] A. Banharnsakun, “Towards improving the convolutional neural networks for deep learning using the distributed artificial bee colony method,” *International Journal of Machine Learning and Cybernetics*, vol. 10, no. 6, pp. 1301–1311, Jun. 2019, doi: 10.1007/S13042-018-0811-Z/FIGURES/10.
[151] L. Zhao, J. G. Santos Macías, L. Ding, H. Idrissi, and A. Simar, “Damage mechanisms in selective laser melted AlSi10Mg under as built and different post-treatment conditions,” *Materials Science and Engineering: A*, vol. 764, p. 138210, Sep. 2019, doi: 10.1016/J.MSEA.2019.138210.
[152] E. Uhlmann, R. Kersting, T. B. Klein, M. F. Cruz, and A. V. Borille, “Additive Manufacturing of Titanium Alloy for Aircraft Components,” *Procedia CIRP*, vol. 35, pp. 55–60, Jan. 2015, doi: 10.1016/J.PROCIR.2015.08.061.
[153] K. N. Amato *et al.*, “Microstructures and mechanical behavior of Inconel 718 fabricated by selective laser melting,” *Acta Mater*, vol. 60, no. 5, pp. 2229–2239, Mar. 2012, doi: 10.1016/J.ACTAMAT.2011.12.032.
[154] F. Geiger, K. Kunze, and T. Etter, “Tailoring the texture of IN738LC processed by selective laser melting (SLM) by specific scanning strategies,” *Materials Science and Engineering: A*, vol. 661, pp. 240–246, Apr. 2016, doi: 10.1016/J.MSEA.2016.03.036.
[155] M. Ma, Z. Wang, and X. Zeng, “A comparison on metallurgical behaviors of 316L stainless steel by selective laser melting and laser cladding deposition,” *Materials Science and Engineering: A*, vol. 685, pp. 265–273, Feb. 2017, doi: 10.1016/J.MSEA.2016.12.112.
[156] H. Rao, S. Giet, K. Yang, X. Wu, and C. H. J. Davies, “The influence of processing parameters on aluminium alloy A357 manufactured by Selective Laser Melting,” *Mater Des*, vol. 109, pp. 334–346, Nov. 2016, doi: 10.1016/J.MATDES.2016.07.009.

[157] F. J. Tavitas-Medrano, • A M A Mohamed, J. E. Gruzleski, F. H. Samuel, and • H W Doty, “Precipitation-hardening in cast AL-Si-Cu-Mg alloys”, doi: 10.1007/s10853-009-3978-6.
[158] K. Kempen, L. Thijs, J. Van Humbeeck, and J. P. Kruth, “Mechanical Properties of AlSi10Mg Produced by Selective Laser Melting,” *Phys Procedia*, vol. 39, pp. 439–446, Jan. 2012, doi: 10.1016/J.PHPRO.2012.10.059.
[159] U. Patakham, A. Palasay, P. Wila, and R. Tongsri, “MPB characteristics and Si morphologies on mechanical properties and fracture behavior of SLM AlSi10Mg,” *Materials Science and Engineering A*, vol. 821, Jul. 2021, doi: 10.1016/J.MSEA.2021.141602.
[160] S. Beretta, M. Gargourimotlagh, S. Foletti, A. du Plessis, and M. Riccio, “Fatigue strength assessment of ‘as built’ AlSi10Mg manufactured by SLM with different build orientations,” *Int J Fatigue*, vol. 139, p. 105737, Oct. 2020, doi: 10.1016/J.IJFATIGUE.2020.105737.
[161] A. Tetelman and R. Chow, “ACOUSTIC EMISSION TESTING AND MICROFRACTURE PROCESSES,” *undefined*, pp. 30-30–11, Mar. 1971, doi: 10.1520/STP35380S.
[162] C. Barile, C. Casavola, G. Pappalettera, and P. K. Vimalathithan, “Acoustic emission descriptors for the mechanical behavior of selective laser melted samples: An innovative approach,” *Mechanics of Materials*, vol. 148, p. 103448, Sep. 2020, doi: 10.1016/J.MECHMAT.2020.103448.
[163] A. Ould Amer, A. L. Gloanec, S. Courtin, and C. Touze, “Characterization of Fatigue Damage in 304L Steel by an Acoustic Emission Method,” *Procedia Eng*, vol. 66, pp. 651–660, Jan. 2013, doi: 10.1016/J.PROENG.2013.12.117.
[164] C. Barile, C. Casavola, and A. Cazzato, “materials Acoustic Emissions in 3D Printed Parts under Mode I Delamination Test,” 2018, doi: 10.3390/ma11091760.
[165] C. Barile, C. Casavola, G. Pappalettera, and C. Pappalettere, “Fatigue Damage Monitoring by Means of Acoustic Emission and Thermography in Ti Grade 5 Specimens,” *Procedia Eng*, vol. 114, pp. 487–492, Jan. 2015, doi: 10.1016/J.PROENG.2015.08.096.
[166] Y. Yao *et al.*, “Microstructural heterogeneity and mechanical anisotropy of 18Ni-330 maraging steel fabricated by selective laser melting: The effect of build orientation and height,” *J Mater Res*, vol. 35, no. 15, pp. 2065–2076, Aug. 2020, doi: 10.1557/JMR.2020.126.
[167] C. Barile, C. Casavola, G. Pappalettera, V. P. Kannan, and D. K. Mpoyi, “Acoustic Emission and Deep Learning for the Classification of the Mechanical Behavior of AlSi10Mg AM-SLM Specimens,” *Applied Sciences 2023, Vol. 13, Page 189*, vol. 13, no. 1, p. 189, Dec. 2022, doi: 10.3390/APP13010189.
[168] C. Barile, C. Casavola, G. Pappalettera, V. P. Kannan, and G. Renna, “Acoustic emission signal processing for the assessment of corrosion behaviour in additively manufactured AlSi10Mg,” *Mechanics of Materials*, vol. 170, p. 104347, Jul. 2022, doi: 10.1016/J.MECHMAT.2022.104347.
[169] P. Ramasamy and S. Sampathkumar, “Prediction of impact damage tolerance of drop impacted WGFRP composite by artificial neural network using acoustic emission parameters,” *Compos B Eng*, vol. 60, pp. 457–462, Apr. 2014, doi: 10.1016/J.COMPOSITESB.2013.12.028.
[170] C. Suresh Kumar, V. Arumugam, R. Sengottuvelusamy, S. Srinivasan, and H. N. Dhakal, “Failure strength prediction of glass/epoxy composite laminates from acoustic emission parameters using artificial neural network,” *Applied Acoustics*, vol. 115, pp. 32–41, Jan. 2017, doi: 10.1016/J.APACOUST.2016.08.013.

[171] D. D'Addona, R. Teti, and G. Caprino, "Residual strength prediction of artificially damaged composite laminates based on neural networks," *Journal of Intelligent & Fuzzy Systems*, vol. 23, no. 5, pp. 217–223, Jan. 2012, doi: 10.3233/IFS-2012-0511.
[172] D. Xu, P. F. Liu, and Z. P. Chen, "A deep learning method for damage prognostics of fiber-reinforced composite laminates using acoustic emission," *Eng Fract Mech*, vol. 259, p. 108139, Jan. 2022, doi: 10.1016/J.ENGFRACMECH.2021.108139.
[173] F. Ucar and D. Korkmaz, "COVIDiagnosis-Net: Deep Bayes-SqueezeNet based diagnosis of the coronavirus disease 2019 (COVID-19) from X-ray images," *Med Hypotheses*, vol. 140, p. 109761, Jul. 2020, doi: 10.1016/J.MEHY.2020.109761.
[174] P. Dhar, S. Dutta, and V. Mukherjee, "Cross-wavelet assisted convolution neural network (AlexNet) approach for phonocardiogram signals classification," *Biomed Signal Process Control*, vol. 63, p. 102142, Jan. 2021, doi: 10.1016/J.BSPC.2020.102142.
[175] Y. Xu, Z. Li, S. Wang, W. Li, T. Sarkodie-Gyan, and S. Feng, "A hybrid deep-learning model for fault diagnosis of rolling bearings," *Measurement*, vol. 169, p. 108502, Feb. 2021, doi: 10.1016/J.MEASUREMENT.2020.108502.
[176] G. Han *et al.*, "Auto-detection of acoustic emission signals from cracking of concrete structures using convolutional neural networks: Upscaling from specimen," *Expert Syst Appl*, vol. 186, p. 115863, Dec. 2021, doi: 10.1016/J.ESWA.2021.115863.
[177] S. Sikdar, D. Liu, and A. Kundu, "Acoustic emission data based deep learning approach for classification and detection of damage-sources in a composite panel," *Compos B Eng*, vol. 228, p. 109450, Jan. 2022, doi: 10.1016/J.COMPOSITESB.2021.109450.
[178] C. Barile, C. Casavola, G. Pappalettera, and V. Paramsamy Kannan, "Damage monitoring of carbon fibre reinforced polymer composites using acoustic emission technique and deep learning," *Compos Struct*, vol. 292, p. 115629, Jul. 2022, doi: 10.1016/J.COMPSTRUCT.2022.115629.
[179] E. Oostwal, M. Straat, and M. Biehl, "Hidden unit specialization in layered neural networks: ReLU vs. sigmoidal activation," *Physica A: Statistical Mechanics and its Applications*, vol. 564, Feb. 2021, doi: 10.1016/J.PHYSA.2020.125517.
[180] M. A. Islam, H. Wimmer, and C. M. Rebman, "Examining Sigmoid vs ReLu Activation Functions in Deep Learning," *Interdisciplinary Research in Technology and Management*, pp. 432–437, Sep. 2021, doi: 10.1201/9781003202240-68.
[181] L. C. Zhang and H. Attar, "Selective Laser Melting of Titanium Alloys and Titanium Matrix Composites for Biomedical Applications: A Review," *Adv Eng Mater*, vol. 18, no. 4, pp. 463–475, Apr. 2016, doi: 10.1002/ADEM.201500419.
[182] Y. Zou *et al.*, "The Effect of Annealing on Microstructure and Mechanical Properties of Selective Laser Melting AlSi10Mg," *IOP Conf Ser Mater Sci Eng*, vol. 538, no. 1, p. 012023, May 2019, doi: 10.1088/1757-899X/538/1/012023.
[183] E. Louvis, P. Fox, and C. J. Sutcliffe, "Selective laser melting of aluminium components," *J Mater Process Technol*, vol. 211, no. 2, pp. 275–284, Feb. 2011, doi: 10.1016/J.JMATPROTEC.2010.09.019.
[184] Y. Kok *et al.*, "Anisotropy and heterogeneity of microstructure and mechanical properties in metal additive manufacturing: A critical review," *Mater Des*, vol. 139, pp. 565–586, Feb. 2018, doi: 10.1016/J.MATDES.2017.11.021.
[185] T. Maconachie *et al.*, "Effect of build orientation on the quasi-static and dynamic response of SLM AlSi10Mg," *Materials Science and Engineering: A*, vol. 788, p. 139445, Jun. 2020, doi: 10.1016/J.MSEA.2020.139445.
[186] B. Wang, S. Zhong, T.-L. Lee, K. S. Fancey, and J. Mi, "Non-destructive Testing and Evaluation of Composite Materials and Structures-Review Non-destructive testing and

evaluation of composite materials/structures: A state-of-the-art review," *Advances in Mechanical Engineering*, vol. 2020, no. 4, pp. 1–28, doi: 10.1177/1687814020913761.
[187] J. Xu, X. Luo, X. Qiu, and G. Hu, "Wavelet and fractal analysis of acoustic emission characteristic of fatigue damage of asphalt mixtures," *Constr Build Mater*, vol. 349, p. 128643, Sep. 2022, doi: 10.1016/J.CONBUILDMAT.2022.128643.
[188] A. Carpinteri, G. Lacidogna, and G. Niccolini, "Fractal analysis of damage detected in concrete structural elements under loading," *Chaos Solitons Fractals*, vol. 42, no. 4, pp. 2047–2056, Nov. 2009, doi: 10.1016/J.CHAOS.2009.03.165.
[189] B. Wisner, K. Mazur, and A. Kontsos, "The use of nondestructive evaluation methods in fatigue: A review," *Fatigue Fract Eng Mater Struct*, vol. 43, no. 5, pp. 859–878, May 2020, doi: 10.1111/FFE.13208.
[190] Z. H. Zhang and J. H. Deng, "A new method for determining the crack classification criterion in acoustic emission parameter analysis," *International Journal of Rock Mechanics and Mining Sciences*, vol. 130, p. 104323, Jun. 2020, doi: 10.1016/J.IJRMMS.2020.104323.
[191] C. Barile, C. Casavola, and G. Pappalettera, "Acoustic emission waveform analysis in CFRP under Mode I test," *Eng Fract Mech*, vol. 210, pp. 408–413, Apr. 2019, doi: 10.1016/J.ENGFRACMECH.2018.01.023.
[192] D. Adeniji, K. Oligee, and J. Schoop, "A Novel Approach for Real-Time Quality Monitoring in Machining of Aerospace Alloy through Acoustic Emission Signal Transformation for DNN," *Journal of Manufacturing and Materials Processing 2022, Vol. 6, Page 18*, vol. 6, no. 1, p. 18, Jan. 2022, doi: 10.3390/JMMP6010018.
[193] J. Gu, Y. Peng, H. Lu, X. Chang, and G. Chen, "A novel fault diagnosis method of rotating machinery via VMD, CWT and improved CNN," *Measurement*, vol. 200, p. 111635, Aug. 2022, doi: 10.1016/J.MEASUREMENT.2022.111635.
[194] S. Vetova, "Comparative analysis on CNN and wavelet features based technology for medical image classification," *AIP Conf Proc*, vol. 2333, no. 1, p. 30003, Mar. 2021, doi: 10.1063/5.0043624/1027780.
[195] L. Alzubaidi *et al.*, "Review of deep learning: concepts, CNN architectures, challenges, applications, future directions," *Journal of Big Data 2021 8:1*, vol. 8, no. 1, pp. 1–74, Mar. 2021, doi: 10.1186/S40537-021-00444-8.
[196] R. Sun, "Optimization for deep learning: theory and algorithms," 2019.
[197] K. Kawaguchi Leslie Pack Kaelbling, "Elimination of All Bad Local Minima in Deep Learning," 2020.
[198] M. Abd Elaziz *et al.*, "Advanced metaheuristic optimization techniques in applications of deep neural networks: a review," *Neural Computing and Applications 2021 33:21*, vol. 33, no. 21, pp. 14079–14099, Apr. 2021, doi: 10.1007/S00521-021-05960-5.
[199] B. Akay, D. Karaboga, and R. Akay, "A comprehensive survey on optimizing deep learning models by metaheuristics," *Artif Intell Rev*, vol. 55, no. 2, pp. 829–894, Feb. 2022, doi: 10.1007/S10462-021-09992-0/FIGURES/17.
[200] Z. H. Zhan, J. Y. Li, and J. Zhang, "Evolutionary deep learning: A survey," *Neurocomputing*, vol. 483, pp. 42–58, Apr. 2022, doi: 10.1016/J.NEUCOM.2022.01.099.
[201] A. Sarkar, S. K. S. Hossain, and R. Sarkar, "Human activity recognition from sensor data using spatial attention-aided CNN with genetic algorithm," *Neural Comput Appl*, vol. 35, no. 7, pp. 5165–5191, Mar. 2023, doi: 10.1007/S00521-022-07911-0/FIGURES/14.
[202] C. R. Reddy, K. H. Reddy, B. S. Goud, and B. Pakkiraiah, "A Deep learning approach for Islanding Detection of Integrated DG with CWT and CNN," *2021 International*

Conference on Sustainable Energy and Future Electric Transportation, SeFet 2021, Jan. 2021, doi: 10.1109/SEFET48154.2021.9375798.

[203] M. Azadi, M. Alizadeh, S. M. Jafari, and A. Farrokhabadi, "Cumulative acoustic emission energy for damage detection in composites reinforced by carbon fibers within low-cycle fatigue regime at various displacement amplitudes and rates," *Polymers and Polymer Composites*, vol. 29, no. 9_suppl, pp. S36–S48, Nov. 2021, doi: 10.1177/0967391120985709/ASSET/IMAGES/LARGE/10.1177_0967391120985709-FIG10.JPEG.

[204] Y. Tian, R. Yu, Y. Zhang, and X. Zhao, "Research on damage evolution of deep formation rock based on acoustic emission test," *International Journal of Damage Mechanics*, vol. 30, no. 1, pp. 145–159, Jan. 2021, doi: 10.1177/1056789520957381/ASSET/IMAGES/LARGE/10.1177_1056789520957381-FIG8.JPEG.

[205] Q. Q. Yu, R. X. Gao, X. L. Gu, X. L. Zhao, and T. Chen, "Bond behavior of CFRP-steel double-lap joints exposed to marine atmosphere and fatigue loading," *Eng Struct*, vol. 175, pp. 76–85, Nov. 2018, doi: 10.1016/J.ENGSTRUCT.2018.08.012.

[206] X. Qiu, J. Xu, S. Xiao, and Q. Yang, "Acoustic emission parameters and waveforms characteristics of fracture failure process of asphalt mixtures," *Constr Build Mater*, vol. 215, pp. 135–147, Aug. 2019, doi: 10.1016/J.CONBUILDMAT.2019.04.150.

[207] M. Mohammad, S. Abdullah, N. Jamaludin, and O. Innayatullah, "Quantitative relationship between strain and acoustic emission response in monitoring fatigue damage," *Jurnal Teknologi (Sciences and Engineering)*, vol. 66, no. 1, pp. 43–47, 2013, doi: 10.11113/JT.V66.1349.

[208] E. Eberhardt, D. Stead, B. Stimpson, and R. S. Read, "Changes in acoustic event properties with progressive fracture damage," *International Journal of Rock Mechanics and Mining Sciences*, vol. 34, no. 3–4, pp. 71.e1-71.e12, Apr. 1997, doi: 10.1016/S1365-1609(97)00062-2.

[209] B. Goszczyńska, "Analysis of the process of crack initiation and evolution in concrete with acoustic emission testing," *Archives of Civil and Mechanical Engineering*, vol. 14, no. 1, pp. 134–143, Jan. 2014, doi: 10.1016/J.ACME.2013.06.002.

[210] M. Habibi, G. Lebrun, and L. Laperrière, "Experimental characterization of short flax fiber mat composites: tensile and flexural properties and damage analysis using acoustic emission," *J Mater Sci*, vol. 52, no. 11, pp. 6567–6580, Jun. 2017, doi: 10.1007/S10853-017-0892-1/FIGURES/7.

[211] E. N. Landis and L. Baillon, "Experiments to Relate Acoustic Emission Energy to Fracture Energy of Concrete," *J Eng Mech*, vol. 128, no. 6, pp. 698–702, Jun. 2002, doi: 10.1061/(ASCE)0733-9399(2002)128:6(698).

[212] W. W. Gerberich, R. H. Jones, M. A. Friesel, and A. Nozue, "Acoustic emission monitoring of stress corrosion cracking," *Materials Science and Engineering: A*, vol. 103, no. 1, pp. 185–191, Aug. 1988, doi: 10.1016/0025-5416(88)90565-4.

[213] K. Otsuka and H. Date, "Fracture process zone in concrete tension specimen," *Eng Fract Mech*, vol. 65, no. 2–3, pp. 111–131, Jan. 2000, doi: 10.1016/S0013-7944(99)00111-3.

[214] C. Barile, C. Casavola, G. Pappalettera, V. P. Kannan, and D. K. Mpoyi, "Acoustic Emission and Deep Learning for the Classification of the Mechanical Behavior of AlSi10Mg AM-SLM Specimens," *Applied Sciences 2023, Vol. 13, Page 189*, vol. 13, no. 1, p. 189, Dec. 2022, doi: 10.3390/APP13010189.

[215] Z. Chen, Y. Wang, J. Wu, C. Deng, and K. Hu, "Sensor data-driven structural damage detection based on deep convolutional neural networks and continuous wavelet transform," *Applied Intelligence*, vol. 51, no. 8, pp. 5598–5609, Aug. 2021, doi: 10.1007/S10489-020-02092-6/FIGURES/11.

[216] M. N. Islam, N. Sulaiman, B. S. Bari, M. Rashid, and M. Mustafa, “A hybrid scheme for AEP based hearing deficiency diagnosis: CWT and convoluted k-nearest neighbour (CKNN) pipeline,” *Neuroscience Informatics*, vol. 2, no. 1, p. 100037, Mar. 2022, doi: 10.1016/J.NEURI.2021.100037.

[217] X. Liu, S. Tian, F. Tao, and W. Yu, “A review of artificial neural networks in the constitutive modeling of composite materials,” *Compos B Eng*, vol. 224, p. 109152, Nov. 2021, doi: 10.1016/J.COMPOSITESB.2021.109152.

[218] F. Ciampa and M. Meo, “A new algorithm for acoustic emission localization and flexural group velocity determination in anisotropic structures,” *Compos Part A Appl Sci Manuf*, vol. 41, no. 12, pp. 1777–1786, Dec. 2010, doi: 10.1016/J.COMPOSITESA.2010.08.013.

[219] Y. Sugita, C. Winkelmann, and V. La Saponara, “Environmental and chemical degradation of carbon/epoxy lap joints for aerospace applications, and effects on their mechanical performance,” *Compos Sci Technol*, vol. 70, no. 5, pp. 829–839, May 2010, doi: 10.1016/J.COMPSCITECH.2010.01.021.

[220] R. D. S. G. Campilho, M. F. S. F. de Moura, and J. J. M. S. Domingues, “Using a cohesive damage model to predict the tensile behaviour of CFRP single-strap repairs,” *Int J Solids Struct*, vol. 45, no. 5, pp. 1497–1512, Mar. 2008, doi: 10.1016/J.IJSOLSTR.2007.10.003.

[221] R. De Araujo, A. Lima, A. Bernasconi, and M. Carboni, “Acoustic emission applied to mode I fatigue damage monitoring of adhesively bonded joints,” *THE E-JOURNAL OF NONDESTRUCTIVE TESTING*, vol. 28, no. 1, pp. 1–9, Jan. 2023, doi: 10.58286/27601.

[222] M. D. Banea, L. F. M. Da Silva, R. D. S. G. Campilho, and C. Sato, “Smart Adhesive Joints: An Overview of Recent Developments,” *https://doi.org/10.1080/00218464.2013.785916*, vol. 90, no. 1, pp. 16–40, 2013, doi: 10.1080/00218464.2013.785916.

[223] G. Li, S. S. Pang, E. Woldesenbet, M. A. Stubblefield, P. F. Mensah, and S. I. Ibekwe, “Investigation of prepreg bonded composite single lap joint,” *Compos B Eng*, vol. 32, no. 8, pp. 651–658, Dec. 2001, doi: 10.1016/S1359-8368(01)00045-2.

[224] G. Li, S. S. Pang, E. Woldesenbet, M. A. Stubblefield, P. F. Mensah, and S. I. Ibekwe, “Investigation of prepreg bonded composite single lap joint,” *Compos B Eng*, vol. 32, no. 8, pp. 651–658, Dec. 2001, doi: 10.1016/S1359-8368(01)00045-2.

[225] W. Zhao, N. Pei, and C. Xu, “Experimental study of carbon/glass fiber-reinforced hybrid laminate composites with torsional loads by using acoustic emission and Micro-CT,” *Compos Struct*, vol. 290, p. 115541, Jun. 2022, doi: 10.1016/J.COMPSTRUCT.2022.115541.

[226] A. A. Taib, R. Boukhili, S. Achiou, and H. Boukehili, “Bonded joints with composite adherends. Part II. Finite element analysis of joggle lap joints,” *Int J Adhes Adhes*, vol. 26, no. 4, pp. 237–248, Jul. 2006, doi: 10.1016/J.IJADHADH.2005.03.014.

[227] C. Barile, C. Casavola, V. Moramarco, C. Pappalettere, and P. K. Vimalathithan, “Bonding Characteristics of Single- and Joggled-Lap CFRP Specimens: Mechanical and Acoustic Investigations,” *Applied Sciences 2020, Vol. 10, Page 1782*, vol. 10, no. 5, p. 1782, Mar. 2020, doi: 10.3390/APP10051782.

[228] C. Barile, C. Casavola, G. Pappalettera, and P. K. Vimalathithan, “Characterization of adhesive bonded CFRP laminates using full-field digital image stereo-correlation and finite element analysis,” *Compos Sci Technol*, vol. 169, pp. 16–25, Jan. 2019, doi: 10.1016/J.COMPSCITECH.2018.10.032.

[229] G. L. Balázs, C. U. Grosse, R. Koch, and H. W. Reinhardt, “Damage accumulation on deformed steel bar to concrete interaction detected by acoustic emission technique,”

https://doi.org/10.1680/macr.1996.48.177.311, vol. 48, no. 4, pp. 311–320, May 2015, doi: 10.1680/MACR.1996.48.177.311.

[230] C. U. Grosse and L. M. Linzer, "Signal-based AE analysis," *Acoustic Emission Testing: Basics for Research-Applications in Civil Engineering*, pp. 53–99, 2008, doi: 10.1007/978-3-540-69972-9_5/COVER.

[231] L. B. Andraju and G. Raju, "Damage characterization of CFRP laminates using acoustic emission and digital image correlation: Clustering, damage identification and classification," *Eng Fract Mech*, vol. 277, p. 108993, Jan. 2023, doi: 10.1016/J.ENGFRACMECH.2022.108993.

[232] V. Arumugam, C. Suresh Kumar, C. Santulli, F. Sarasini, and A. J. Stanley, "Identification of Failure Modes in Composites from Clustered Acoustic Emission Data Using Pattern Recognition and Wavelet Transformation," *Arab J Sci Eng*, vol. 38, no. 5, pp. 1087–1102, May 2013, doi: 10.1007/S13369-012-0351-X/METRICS.

[233] C. Barile, C. Casavola, G. Pappalettera, and P. K. Vimalathithan, "Damage Propagation Analysis in the Single Lap Shear and Single Lap Shear-Riveted CFRP Joints by Acoustic Emission and Pattern Recognition Approach," *Materials 2020, Vol. 13, Page 3963*, vol. 13, no. 18, p. 3963, Sep. 2020, doi: 10.3390/MA13183963.

[234] C. Barile, C. Casavola, G. Pappalettera, C. Pappalettere, and P. K. Vimalathithan, "Evaluating Bonding Characteristics of Joggled Lap CFRP Using Acoustic Emission Techniques," *Structural Integrity*, vol. 16, pp. 26–31, 2020, doi: 10.1007/978-3-030-47883-4_5/COVER.

[235] P. J. de Groot, P. A. M. Wijnen, and R. B. F. Janssen, "Real-time frequency determination of acoustic emission for different fracture mechanisms in carbon/epoxy composites," *Compos Sci Technol*, vol. 55, no. 4, pp. 405–412, Jan. 1995, doi: 10.1016/0266-3538(95)00121-2.

[236] P. F. Liu, J. K. Chu, Y. L. Liu, and J. Y. Zheng, "A study on the failure mechanisms of carbon fiber/epoxy composite laminates using acoustic emission," *Mater Des*, vol. 37, pp. 228–235, May 2012, doi: 10.1016/J.MATDES.2011.12.015.

[237] D. Bhowick, D. K. Gupta, S. Maiti, and U. Shankar, "Stacked autoencoders based machine learning for noise reduction and signal reconstruction in geophysical data," *arXiv: Computational Engineering, Finance, and Science*, 2019.

[238] C. S. N. Pathirage, J. Li, L. Li, H. Hao, and W. Liu, "Application of deep autoencoder model for structural condition monitoring," *Journal of Systems Engineering and Electronics*, vol. 29, no. 4, pp. 873–880, Aug. 2018, doi: 10.21629/JSEE.2018.04.22.

[239] K. Lee, S. Jeong, S. H. Sim, and D. H. Shin, "Field experiment on a PSC-I bridge for convolutional autoencoder-based damage detection," *https://doi.org/10.1177/1475921720926267*, vol. 20, no. 4, pp. 1627–1643, Jun. 2020, doi: 10.1177/1475921720926267.

[240] P. J. de Groot, P. A. M. Wijnen, and R. B. F. Janssen, "Real-time frequency determination of acoustic emission for different fracture mechanisms in carbon/epoxy composites," *Compos Sci Technol*, vol. 55, no. 4, pp. 405–412, Jan. 1995, doi: 10.1016/0266-3538(95)00121-2.

[241] C. Barile, C. Casavola, G. Pappalettera, and P. K. Vimalathithan, "Damage characterization in composite materials using acoustic emission signal-based and parameter-based data," *Compos B Eng*, vol. 178, p. 107469, Dec. 2019, doi: 10.1016/J.COMPOSITESB.2019.107469.

[242] C. Barile, C. Casavola, G. Pappalettera, and V. P. Kannan, "Application of different acoustic emission descriptors in damage assessment of fiber reinforced plastics: A comprehensive review," *Eng Fract Mech*, vol. 235, p. 107083, Aug. 2020, doi: 10.1016/J.ENGFRACMECH.2020.107083.

[243] L. B. Andraju and G. Raju, “Damage characterization of CFRP laminates using acoustic emission and digital image correlation: Clustering, damage identification and classification,” *Eng Fract Mech*, vol. 277, p. 108993, Jan. 2023, doi: 10.1016/J.ENGFRACMECH.2022.108993.
[244] P. Mahesh, V. Chinthapenta, G. Raju, and M. Ramji, “Experimental investigation on open-hole CFRP laminate under combined loading using acoustic emission and digital image correlation,” *Theoretical and Applied Fracture Mechanics*, vol. 130, p. 104300, Apr. 2024, doi: 10.1016/J.TAFMEC.2024.104300.
[245] H. Q. Ali, I. Emami Tabrizi, R. M. A. Khan, A. Tufani, and M. Yildiz, “Microscopic analysis of failure in woven carbon fabric laminates coupled with digital image correlation and acoustic emission,” *Compos Struct*, vol. 230, p. 111515, Dec. 2019, doi: 10.1016/J.COMPSTRUCT.2019.111515.
[246] S. F. Karimian and M. Modarres, “Acoustic emission signal clustering in CFRP laminates using a new feature set based on waveform analysis and information entropy analysis,” *Compos Struct*, vol. 268, p. 113987, Jul. 2021, doi: 10.1016/J.COMPSTRUCT.2021.113987.
[247] P. F. Liu, J. K. Chu, Y. L. Liu, and J. Y. Zheng, “A study on the failure mechanisms of carbon fiber/epoxy composite laminates using acoustic emission,” *Mater Des*, vol. 37, pp. 228–235, May 2012, doi: 10.1016/J.MATDES.2011.12.015.
[248] X. Zhuang and X. Yan, “Investigation of damage mechanisms in self-reinforced polyethylene composites by acoustic emission,” *Compos Sci Technol*, vol. 66, no. 3–4, pp. 444–449, Mar. 2006, doi: 10.1016/J.COMPSCITECH.2005.07.013.
[249] S. Barré and M. L. Benzeggagh, “On the use of acoustic emission to investigate damage mechanisms in glass-fibre-reinforced polypropylene,” *Compos Sci Technol*, vol. 52, no. 3, pp. 369–376, Jan. 1994, doi: 10.1016/0266-3538(94)90171-6.
[250] H. WenQin, L. Ying, G. AiJun, and F. G. Yuan, “Damage Modes Recognition and Hilbert-Huang Transform Analyses of CFRP Laminates Utilizing Acoustic Emission Technique,” *Applied Composite Materials*, vol. 23, no. 2, pp. 155–178, Apr. 2016, doi: 10.1007/S10443-015-9454-3/FIGURES/30.
[251] W. Q. Han, A. J. Gu, and J. Zhou, “A Damage Modes Extraction Method from AE Signal in Composite Laminates Based on DEEMD,” *J Nondestr Eval*, vol. 38, no. 3, pp. 1–10, Sep. 2019, doi: 10.1007/S10921-019-0609-2/FIGURES/15.